Precision Spectroscopy of Kaonic Helium-4 $3d \to 2p$ X-rays

K中間子ヘリウム4原子X線 $3d \to 2p$ 遷移の精密分光

Master's Thesis

Hideyuki TATSUNO

竜野秀行

Department of Physics, School of Science
University of Tokyo

February 5, 2007

Abstract

For the strong-interaction effects of kaonic-helium atom, there has been a known discrepancy between previous experimental results and predictions of the conventional optical-potential model. The average of the past measurements is more than five standard deviations away from the theoretical calculation. In order to explain the significant disagreement called "kaonic helium atom puzzle," a possibility of kaon-nucleus bound state was indicated more than 30 years ago.

At present, deeply-bound kaon-nucleus states were predicted by Akaishi and Yamazaki by treating $\Lambda(1405)$ as a $\bar{K}$-N bound state, and unconventionally attractive K^--nucleus potentials were indicated. From the point of view of the 'deep' potentials, the strong-interaction effects of kaonic-helium $2p$ state were re-calculated, then anomalously large shift and width were predicted. However, even with this new calculation, the previous experimental values were still far away.

To provide a conclusive answer for the puzzle, we have performed a precise measurement of kaonic helium-4 X-rays using silicon drift detectors which have good energy resolution and small detector thickness. We used the method of the vertex reconstruction of the kaon-reaction point to suppress the background. In addition, we realized the in-beam energy calibration using titanium and nickel characteristic X-rays.

We obtained for the strong-interaction shift and width of kaonic-helium $2p$ state with the best statistical accuracy to date,

$$\begin{aligned} \Delta E_{2p} &= -3.3 \pm 2.2(\text{stat.}) \text{ eV (repulsive)} \\ \Gamma_{2p} &= 33 \pm 6(\text{stat.}) \text{ eV} \end{aligned}$$

Since the analysis has not been finished, the systematic error is not definite and its estimation is work in progress. Even if a conservative error is considered, these results are consistent with the conventional optical-potential model and the Akaishi-Yamazaki prediction of deeply-bound kaon-nucleus states.

Contents

List of Figures

List of Tables

Chapter 1

Introduction

1.1 Kaonic Helium Atom Puzzle

There is a long standing puzzle about the kaonic helium atom, which is related directly to the strong interaction between kaons and helium nuclei and to a possibility of kaon-nucleus bound states.

The puzzle is based on the discrepancy between the measured and theoretical values of the strong-interaction shift of kaonic-helium $2p$ states. There are two types of theories compared to the experimental results,

- the conventional optical-potential model [1],
- Akaishi-Yamazaki model of deeply-bound kaon-nucleus states [2],

Here, the "kaonic helium puzzle" is explained with a historical survey of kaonic-helium atom and kaon-nucleus bound states.

1.1.1 Previous Measurements and Theoretical Predictions

Before bringing this introduction forward, it is necessary to first clarify the definition of the energy shift (ΔE) used in the present work. The shift is defined by the difference between the measured transition energy and the calculated pure-electromagnetic X-ray energy ($\Delta E = E_{\rm X}^{\rm exp} - E_{\rm X}^{\rm EM}$), where $E_{\rm X}^{\rm exp}$ and $E_{\rm X}^{\rm EM}$ are the measured energy and the calculated one only with the Coulomb interaction, respectively. If the strong-interaction effect is *repulsive*, the atomic-level shifts upward, and the transition energy to the shifted level decreases from the pure-electromagnetic one, then the shift (ΔE) has negative sign.

The shift and width of the kaonic-helium $2p$ state have been measured three times in the 1970's and 1980's [3–5]. All experiments observed large repulsive shifts and broad widths. The world average was

$$\Delta E_{2p} = -43 \pm 8 \text{ eV}, \quad \Gamma_{2p} = 55 \pm 34 \text{ eV},$$

On the other hand, the optical-potential model predicts [6] on the order of

$$\Delta E_{2p} = -0.2 \text{ eV}, \quad \Gamma_{2p} = 2 \text{ eV},$$

meaning that the shift and width will not be accurately measurable.

In order to explain these discrepancies, Batty implied a possibility of a bound state of the kaon in the helium nucleus [6]. A kaon-nucleus bound state can give rise to large energy shifts and widths in the atomic states. Assuming that the effective scattering length is represented by

$$V_{\text{opt}} = -\frac{2\pi}{\mu}\left(1 + \frac{\mu}{m}\right)\bar{a}\rho(r) \tag{1.1}$$

where μ is the reduced mass of K^--^{4}He system, m is the mass of nucleon, $\rho(r)$ is the nucleon density distribution and $\bar{a}$ is a complex "effective scattering length," the relation of shift and width with the effective scattering length is calculated as shown in Figure 1.1. The oscillations in the shift and width correspond to cases where a_R is sufficiently large to produce binding of a further kaon-nucleus bound state. However, the previous experimental results could not be reproduced even with this calculation.

1.1.2 Predictions of Deeply Bound $\bar{K}$ States

The concept of a kaon-nucleus bound state was invoked more than 30 years ago by Seki [7] and by Koch *et al.* [8] within the optical-potential model. Later, the bound state was predicted as a 'deeply-bound' kaonic-atom state by the global fit to a comprehensive data set of the kaonic-atom X-rays [9].

In the late 1990's, the low-energy $\bar{K}N$ interaction was established by the KpX experiment [10]. This made it possible to calculate $\bar{K}$-nucleus bound states quantitatively, especially for the $\Lambda(1405)$, and to predict narrow deeply-bound kaon-nucleus states. Akaishi and Yamazaki predicted the objects using the g matrix method [2]. They calculated the potentials and bound levels for the K^--p, K^--^{3}He and K^--^{4}He systems which correspond to $\Lambda(1405)$, $^3_{\bar{K}}$H and $^4_{\bar{K}}$H, respectively. Figure 1.2 shows the predicted nuclear bound states.

Just after these predictions, several experimental indications have been reported, for example, KEK-PS E471 (2004) [11,12], DAΦNE FINUDA (2005) [13] and BNL-AGS E930 (2005) [14]. Even though hot discussions have occurred in several conferences, interpretations are not yet conclusive.

1.1.3 Akaishi's Calculations for ΔE_{2p} and Γ_{2p}

To coincide with the above discussions, the kaonic-helium puzzle was reconsidered by Akaishi. He calculated the strong-interaction effects of K^--^{4}He and K^--^{3}He atoms from the view point of the formation of deeply-bound kaon-nucleus states using a coupled-channel model. As a result, anomalous shift $|\Delta E_{2p}| \leq 11$ eV and

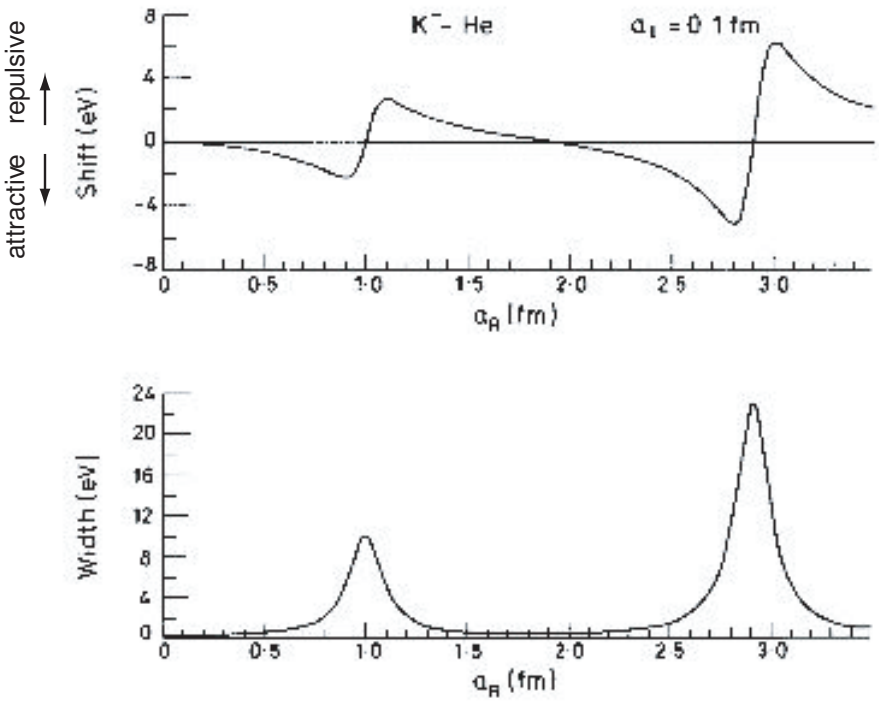

Figure 1.1: Calculated strong-interaction shift and width for the $2p$ state in the kaonic-helium atom as a function of a_R, the real part of $\bar{a}$, with $a_I = 0.1$ fm [6]. A large a_R corresponds to a deep real-part potential. Note that the definition of the *repulsive* sign is inverse.

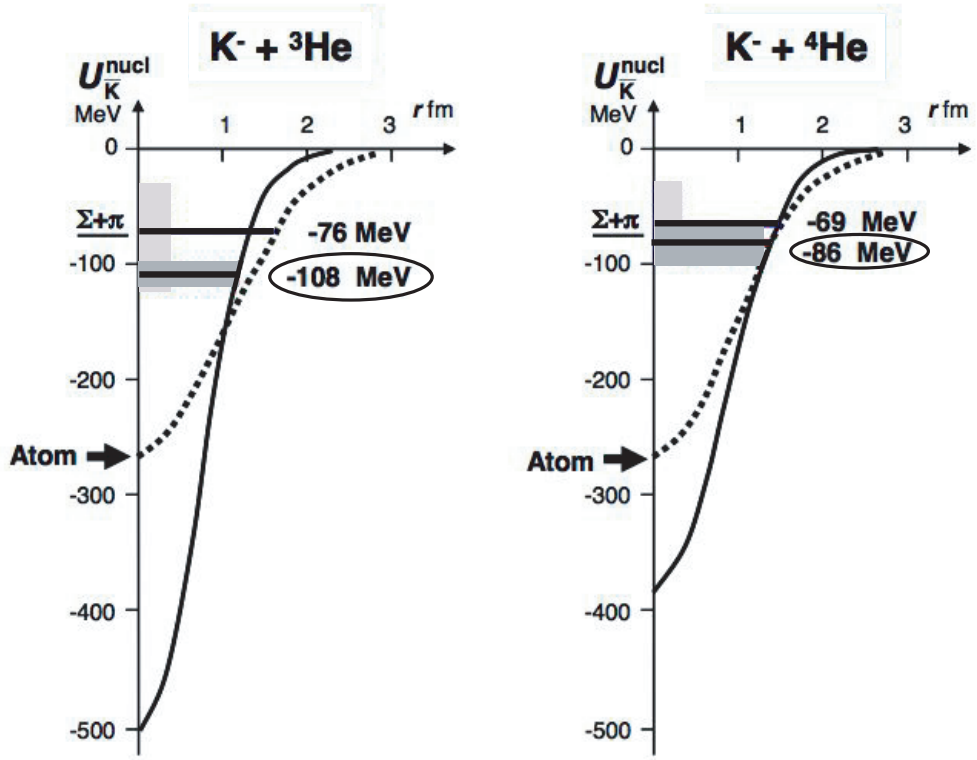

Figure 1.2: Real part of the potential of the K^--^{3}He and K^--^{4}He strong interaction. The dashed line is the case of *unchanged* nuclear cores, which relates directly to atomic-state shifts, and the solid line is the case of *shrunk* nuclear cores with consideration of changing the core-density distribution due to the strong attraction of the K^-. Nuclear s-wave bound states are shown. The states with circles are the predicted deeply-bound states in [2].

width $\Gamma_{2p} \leq 40$ eV were obtained for the K^--^{4}He atom [17]. The result is shown in Figure 1.3. However, the previous experimental results could not be reproduced even with this new calculation. Comparisons between this calculation and the past experimental results are shown in Figure 1.4 and Figure 1.5.

After Akaishi's new prediction, KEK-PS E570 experiment was proposed to provide a conclusive answer for the question "*Is really the strong-interaction shift of the kaonic helium-4 atom so large that a kaon-nucleus bound state exists?* "

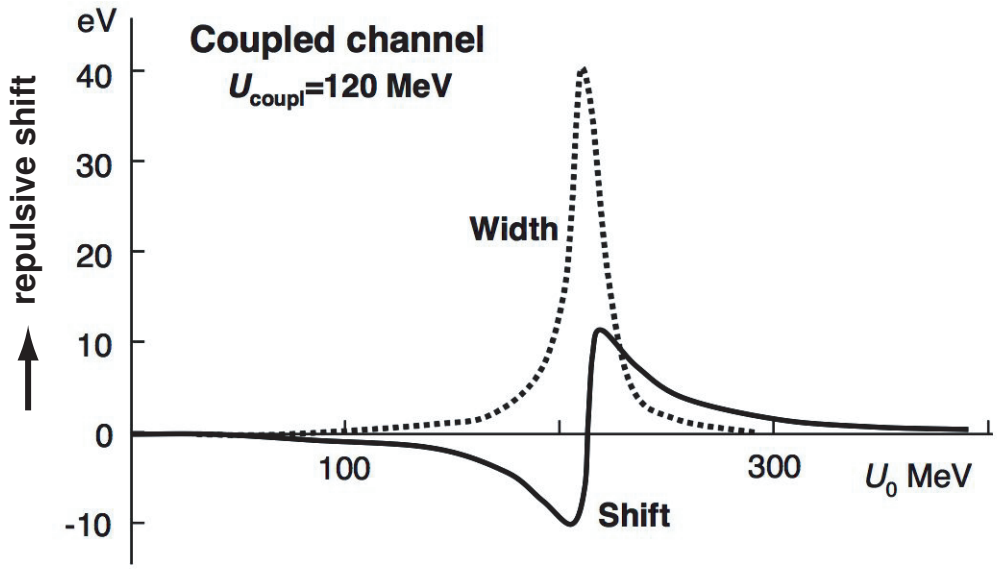

Figure 1.3: Akaishi's calculations for the shift ΔE_{2p} and the width Γ_{2p} of the K^--^{4}He atom as a function of the potential strength U_0 with the coupling potential $U_{\rm coupl} = 120$ MeV [17]. An anomalous shift $|\Delta E_{2p}| \leq 11$ eV and width $\Gamma_{2p} \leq 40$ eV were obtained. Note that the definition of the *repulsive* sign is inverse.

1.2 Present Experiment KEK-PS E570

In this section, the principles and approach of the present experiment, which is the last experiment at KEK-PS, are described.

1.2.1 Principles

When a negative kaon is stopped in a helium target, it is captured into an atomic orbit around a helium nucleus with a principal quantum number of $n = \sqrt{M^*/m_e} \sim$

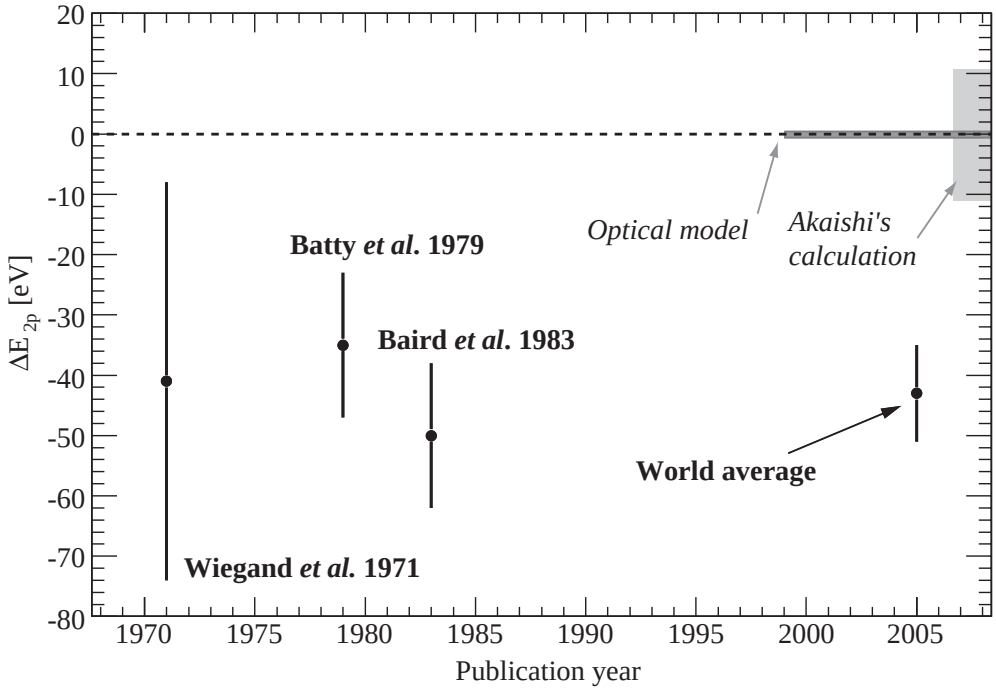

Figure 1.4: Comparison between theoretical predictions and previous experimental results for ΔE_{2p}. The negative sign corresponds to a repulsive shift. The world average is far away from theoretical predictions.

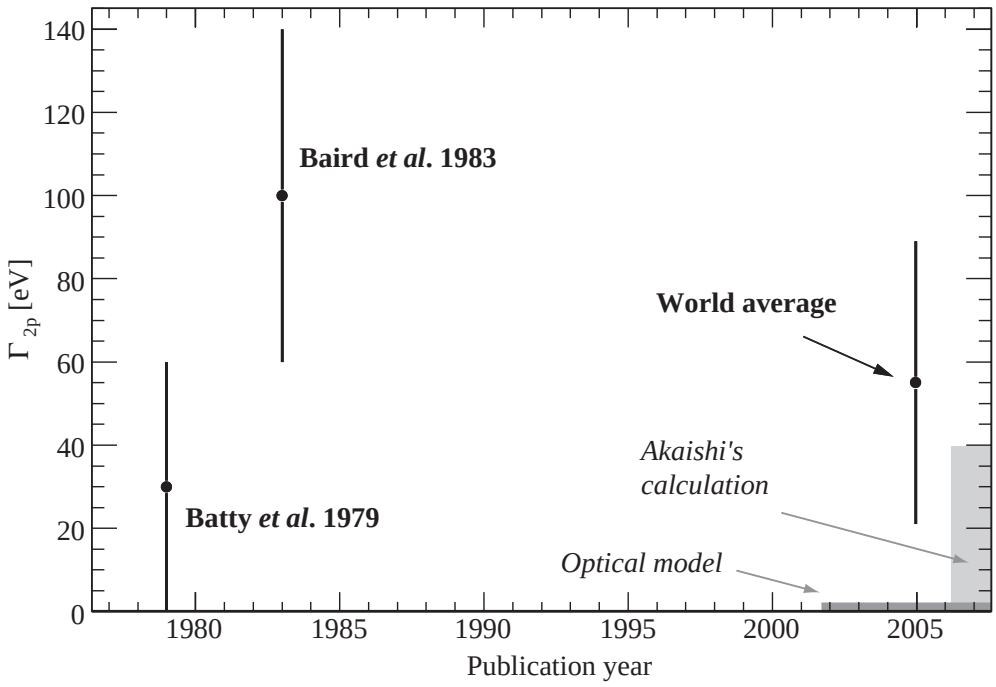

Figure 1.5: Comparison between theoretical predictions and previous experimental results for Γ_{2p}. Akaishi's calculation shows a finite width due to a deepliy-bound kaon-nucleus state.

30 by replacing an electron, where M^* and m_e are the reduced mass of negative kaon and electron, respectively. The possibility of kaonic-helium-atom formation becomes maximum when a kaon is captured at the same radius as an electron. The highly excited kaon then cascades down to lower atomic levels and is finally absorbed by the nucleus through the strong interaction. Some of the trapped kaons lose their energy by emitting X-rays and are absorbed.

The atomic levels of a kanoic-helium are shifted and broadened by the strong interaction. The states with smaller n and l (orbital angular momentum) are affected significantly due to the larger overlap between the kaon and the helium nucleus wavefunction. Since the absorption is too strong to observe the radiative transition to $1s$ state of the kaonic-helium atom, its practical last-observable state is the $2p$ state. Therefore the $3d \rightarrow 2p$ transition is the most suitable to observe the strong-interaction effects.

By comparing the pure-electromagnetic X-ray energy with the measured one which has a finite absorption width, the strong-interaction effects are evaluated as a *shift* and *width*. Our objective is to observe these strong-interaction effects on the $2p$ state of the kaonic-helium atom.

The electromagnetic X-ray energies are calculated in the framework of the Klein-Gordon equation with finite-nuclear size, finite-particle size and vacuum-polarization corrections. The calculation results are listed in Table 1.1.

Table 1.1: Calculated values of pure-electromagnetic X-rays energy of kaonic-helium atom. [5, 15, 16].

Transition	X-ray name	Calculated X-ray Energy (eV)
$3d \rightarrow 2p$	Lα	6463
$4d \rightarrow 2p$	Lβ	8722
$5d \rightarrow 2p$	Lγ	9767
$6d \rightarrow 2p$	Lδ	10331

1.2.2 Previous Experiments

As mentioned in section 1.1.1, three experiments have been performed in the 1970's and 1980's [3–5]. In previous experiments, a liquid helium target was used in oder to stop a sufficient number of kaons, and the X-rays were detected by Si(Li) detectors. The energy resolution of the Si(Li)s was 250-360 eV (FWHM) at 6.4 keV. The X-ray energy was calibrated by radiative sources. Figure 1.6 shows previous experimental X-ray spectra.

When we read the papers, we notice a large background of X-ray spectrum. The background was originated from Compton scattering in the thick Si(Li) detector by high-energy γ-rays and the contamination of other X-rays. The latter was because

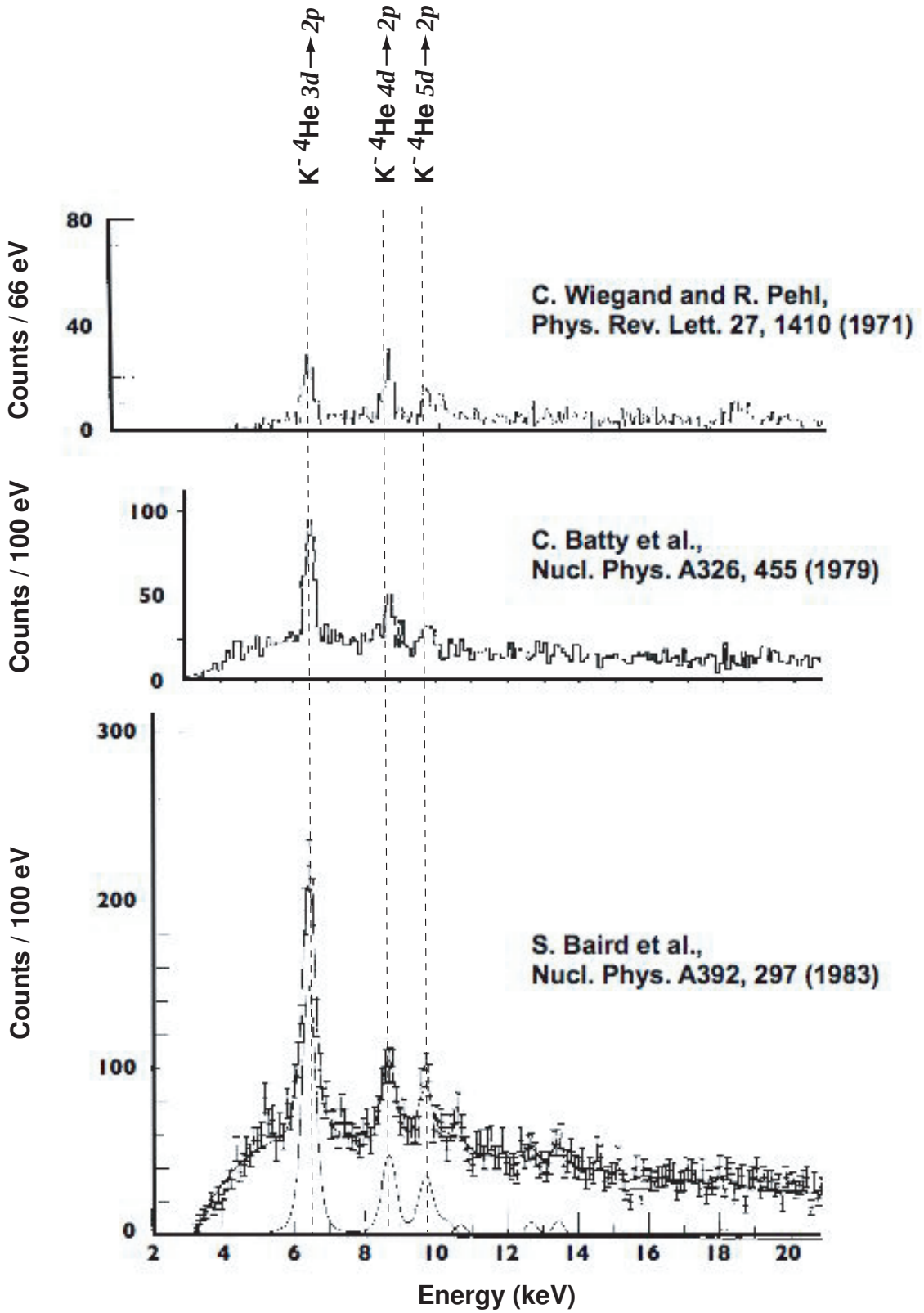

Figure 1.6: X-ray spectra obtained in previous experiments. The dashed lines show the kaonic helium-4 atom X-rays, transitions $3d \rightarrow 2p$, $4d \rightarrow 2p$ and $5d \rightarrow 2p$.

the incident kaons were not identified as 'stopped' one in the target. In addition, the calibration method was not enough to monitor the time-dependent gain drifts of the X-ray detectors.

The results of previous measurements are summarized in Table 1.2. The measured shift and width are both too large to be reconciled with the theoretical predictions.

Table 1.2: Previous experimental results for the strong interaction shift and width of the kaonic helium $2p$ state and their weighted average.

Reference	ΔE_{2p} (eV)	Γ_{2p} (eV)	Si(Li) detector area, thickness	Resolution @ 6.4 keV (eV FWHM)
[3]	-41 ± 33	–	254 mm^2, 4 mm	340
[4]	-35 ± 12	30 ± 30	300 mm^2, 5 mm	250
[5]	-50 ± 12	100 ± 40	300 mm^2, 5 mm	360
Average	-43 ± 8	55 ± 34		

1.2.3 E570 Approach

The improvements of our experiment are summarized as follows,

1. good energy resolution using silicon drift detectors,
2. background suppression by reconstructing a reaction point of a kaon and target material,
3. in-beam energy calibration.

- **Good Energy Resolution**

Instead of Si(Li) detectors, we used silicon drift detectors (SDDs), which will be described in section 2.6.1. The SDD has a good energy resolution of $\sim$ 180 eV at 6.4 keV and a reasonable timing resolution of $\sim$ 0.5 μs. In addition, even though it has a large 100 mm^2 effective area, its thickness is only about 0.3 mm, one order magnitude thinner than conventional Si(Li). This is because the background from Compton scattering in the detector can be reduced. The high resolution and the large effective area result in a high-statistics measurement.

- **Background Suppression**

To suppress the background and improve the signal-to-noise ratio, we required a coincidence of a SDD signal with a secondary charged particle which was emitted

from the K^{-}^{4}He reaction in the target. The secondary charged particle was tracked by drift chambers, and the reaction point was reconstructed with beam tracking information. Then by applying the target-fiducial-volume cuts, we can ensure the X-ray signal came from within the target.

- **In-beam Energy Calibration**

Energy calibration is most significant for precision spectroscopy. The accuracy of the calibration depends on the gain stability. We realized the in-beam energy calibration using energy of two different characteristic X-rays of titanium and nickel. The calibration X-rays are listed in Table 1.3 [21]. These X-rays were emitted from pure-metal foils ionized by charged particles (mainly contamination pions in the beam).

Table 1.3: Calibration X-rays energy [21]. Only K_{α} lines were used for the calibration.

Metal	X-ray name	Energy (eV)
Ti	$K_{\alpha 1}$	4510.84
	$K_{\alpha 2}$	4504.86
	$K_{\beta 1}$	4931.81
Ni	$K_{\alpha 1}$	7478.15
	$K_{\alpha 2}$	7460.89
	$K_{\beta 1}$	8264.66

Chapter 2

Experimental Setup

2.1 Overview

The E570 experiment has been performed at K5 beam line in the north counter hall of the KEK[(i)] 12-GeV Proton Synchrotron. The K^- beam was obtained as a secondary beam from a production target hit with the primary proton beam, and the beam momentum was selected as ≈ 650 MeV/c in order to maximize the number of stopped K^- on a target.

An overview of the experimental setup is shown in Figure 2.2 with detail around the target shown in Figure 2.3. Negative kaons from the K5 beam line were degraded with carbon degraders and stopped in a superfluid liquid helium-4 target. The X-rays generated from the stopped K^- position were measured with silicon drift detectors (SDDs) installed downstream of the target.

Two Lucite Čerenkov counters were used to separate the timing of kaons and contaminating pions. Under our experiment conditions, the K^- : π^- ratio was $\sim 1:200$ at T0 counter. The large amount of pions was used to induce calibration X-rays by hitting pure-metal foils put downstream of the target.

The beam track was measured by beam-line drift chambers (BLC) just after the T0. In order to reconstruct the stopping position of kaons, tracks of secondary charged particles emitted from nuclear reactions of a kaon and a target nucleus were measured with a vertex drift chamber (VDC) or proton drift chamber (PDC). VDCs were positioned top and bottom of the target to cover $\sim 34\%$ of a total solid angle seen from the target center. On the other hand PDCs were positioned left and right of the target, and it covered $\sim 7\%$ of the total solid angle. The secondary charged particles were detected by trigger counters (TCs), PA and PB after the tracking devices.

The experimental setup consisted of four major parts, namely: the beam-line detector system, the target system, the vertex detector system and the X-ray detector system. In addition to these parts, the data acquisition system is also one of the

[(i)] High Energy Accelerator Research Organization

important elements of the experiment. In this chapter, each of them is described.

2.2 KEK 12-GeV Proton Synchrotron and K5 Beam Line

2.2.1 KEK 12-GeV Proton Synchrotron

The protons were accelerated up to 12 GeV and were introduced to experimental halls through slow extraction lines. The extract-repetition cycle of the synchrotron was 4 seconds with the pulse duration of 2 seconds. The typical beam intensity was 1.7×10^{12} protons per pulse at the time of E570.

2.2.2 K5 Beam Line

The K5 beam line, where our experiment has been performed, is located in the north counter hall. The configuration of K5 beam line is shown in Figure 2.1 and its parameters are summarized in Table 2.1. The primary proton beam bombards the production target made of 60-mm-thick Pt. The target provides secondary particles to the low-momentum (0.4-0.6 GeV/c) separated beam line using D1 magnet. The secondary particles (π^-, K^-, $\bar{p}$, etc.) are introduced into the electrostatic (DC) separator which has an electric-field gradient in the vertical direction. The charged-particle beams are focused in the horizontal plane. The specification of the field of the DC separator is 50 kV/cm (+375 kV/−375 kV at the electrodes). It was operated at +275 kV/−325 kV during the first cycle of E570 and +300 kV/−350 kV during the second cycle. The typical number of injected kaons was about 20 k/spill, that of detected kaons at LCs was 5 k/spill and that of stopped kaons was ∼300/spill (spill=2 s with an interval of 2 seconds).

2.3 Beam Line Detector System

In this section, the detector system of the beam line, especially for the kaon beam, is described.

2.3.1 Kaon Trigger Counters

To tag the kaons of the beam, Lucite Čerenkov counters (LC1 and LC2) were used as threshold counters (the refractive index was 1.49). The 2-inch photomultiplier tubes (PMTs) were attached to the left and right side of the Lucite radiator. Another plastic scintillation counter T1 was installed just upstream of the carbon degraders. The T1 had 2-inch PMTs on both its ends.

After kaons were degraded by carbon degraders (1.99 g/cm^3), the beam was finally defined by T0 counters. Figure 2.4 shows a schematic view of the T0 counters.

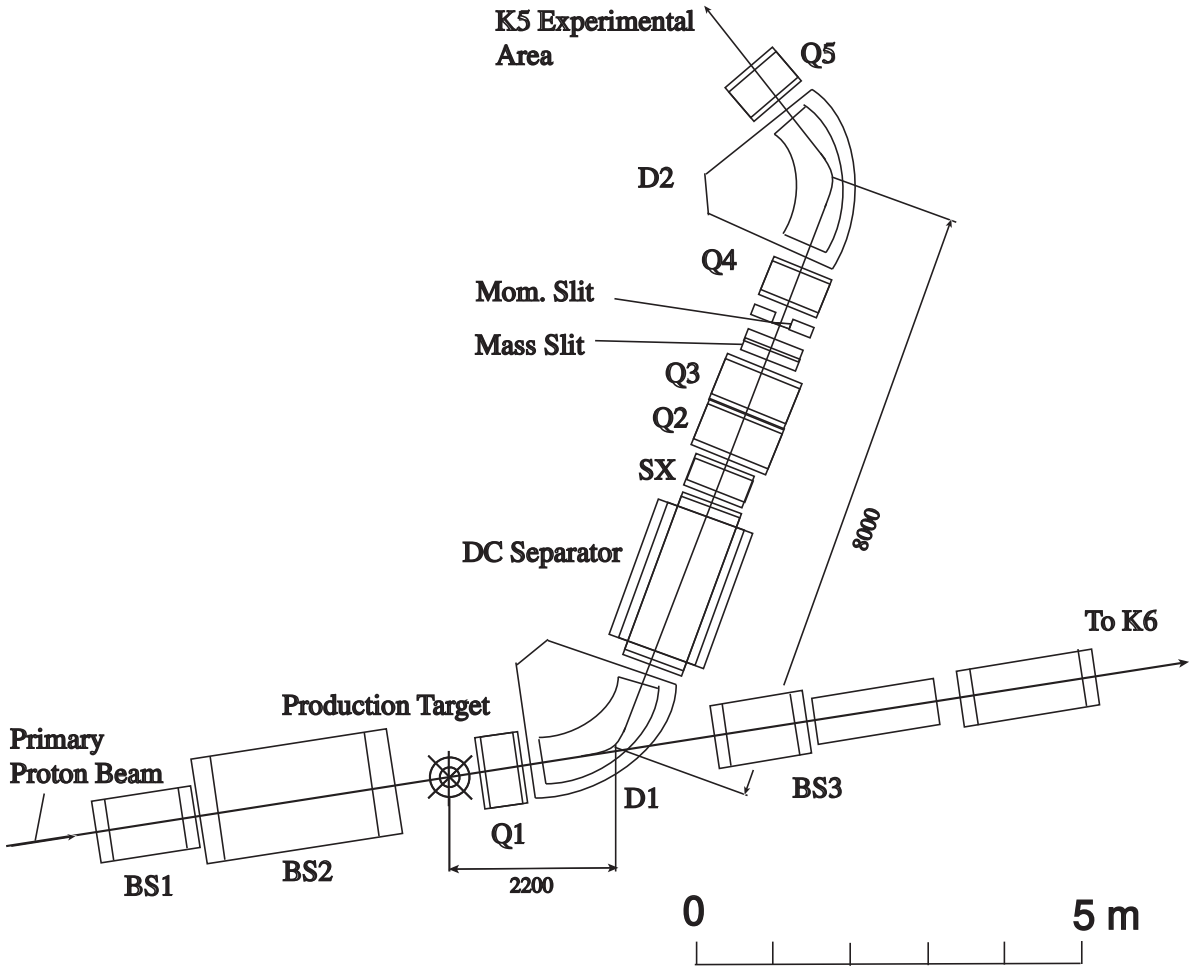

Figure 2.1: Schematic view of the K5 beam line of the KEK 12-GeV PS.

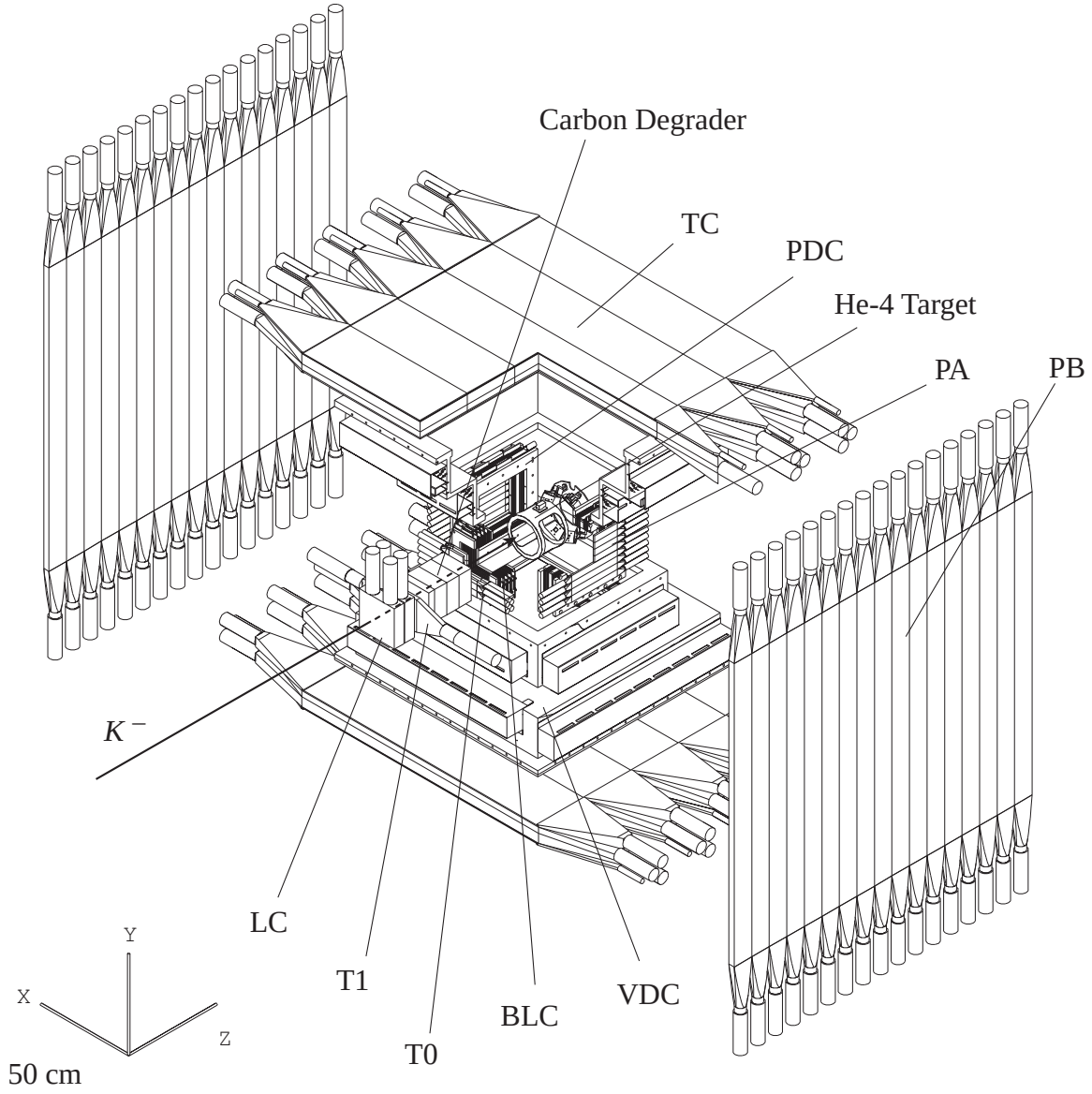

Figure 2.2: Schematic view of the experimental setup of E570.

Table 2.1: Parameters of the K5 beam line. H, V and L describe horizontal, vertical and longitudinal direction respectively [18].

Momentum range	0.65 GeV/c maximum
Production target	Pt (6 mm(V)×10 mm(H)×60 mm(L))
Beam length	12.5 m
Solid angle acceptance 10 msr	
	±180 mrad (H)
	±18 mrad (V)
Momentum bite	±4%
Electrostatic separator	length 2 m
	gap 15 cm
	field 50 keV/cm
Beam characteristics at the beam end	
Magnification	2.2 (H), 1.1 (V)
Dispersion	−0.28 (cm/% dp/p)
Image size	5 mmϕ
Divergence	±130 mrad (H)
	±13 mrad (V)

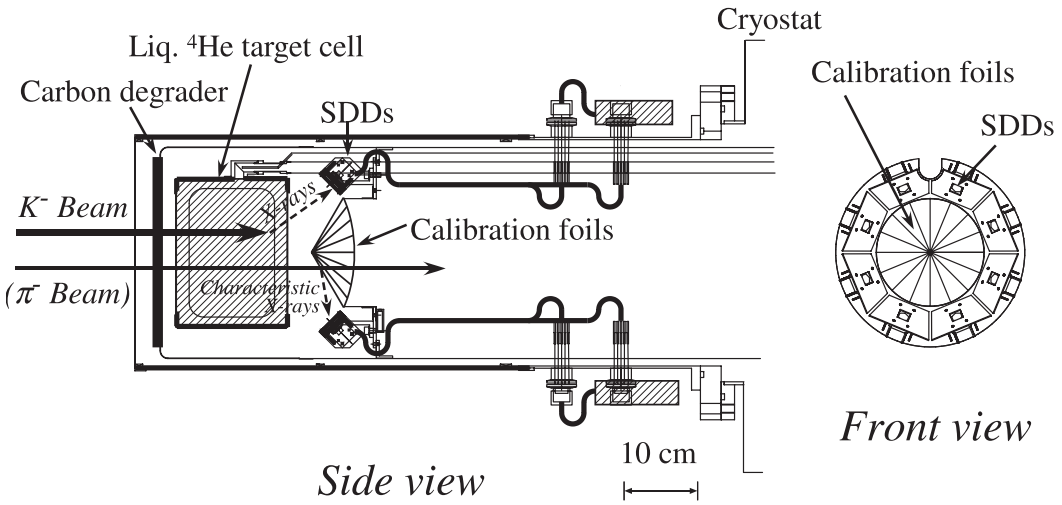

Figure 2.3: Schematic view around the liquid helium-4 target.

The T0 counters consisted of two identical layers which were divided into five segments to keep good time resolution under the high-rate condition. Each segments had a plastic scintillator (Saint-Gobain), Lucite light guides and 3/4-inch PMTs on both ends. These counters are used as dE/dx counters for stopped K^- events selection (see appendix A.3).

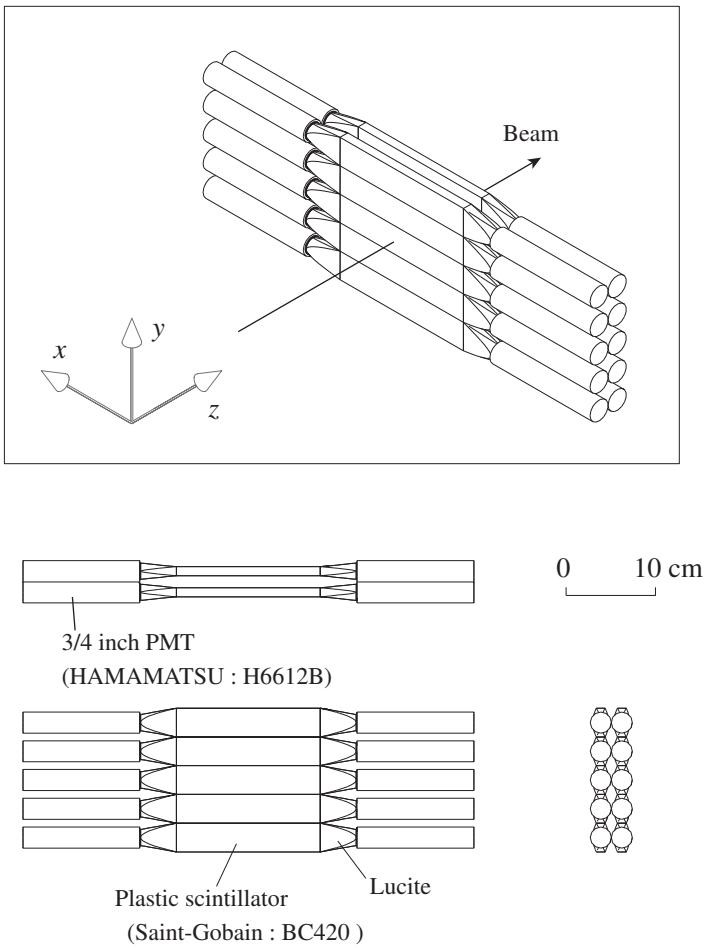

Figure 2.4: Schematic view of T0 counters.

2.3.2 Beam Line Drift Chamber

A reaction vertex in the target was determined by tracking the incident kaons and the secondary charged particles with high-rate drift chambers. The incident-kaon beam was tracked by beam-line drift chambers (BLC). Figure 2.5 shows a schematic view of the BLC. The BLC consisted of four sets of chamber units. Each unit had four layers of sense wire planes (XX′YY′), the prime means the half-cell-shifted sense-wire plane. The shifted plane was used to resolve the left-right ambiguity. A plane had 32 wires, and the total number of planes was $4 \times 4 = 16$, so the number of

readout channels was $32 \times 16 = 512$. 32 amplifier-shaper-discriminator (ASD) cards were used for readout (1 ASD cards had 16 channels).

A wire structure and a cross-sectional drawing of the chamber is shown in Figure 2.6. The sense wire (anode) and the potential wire (cathode) were supplied the negative high voltages with, -1.25 kV and -1.30 kV for cathode planes and cathode wires, respectively. The sense wire and the potential wire were made of gold-plated tungsten with 3% rhenium ($\phi 12$ μm) and gold-plated copper-beryllium ($\phi 75$ μm), respectively. The cathode planes were made of 1.5-μm-thick aluminized Mylar. The sense-wire spacing was 2.5 mm, and the gap between the wire and the cathode plane was 2.5 mm. Each BLC was operated with Ar - isobutane 80 : 20 gas mixture with a small amount of methylal. The typical gas consumption in the BLC was 35 cc/min.

The BLC tracking resolution was $\sigma \sim 0.12$ mm for zx and zy planes, and the average tracking efficiency was about 74%[ii].

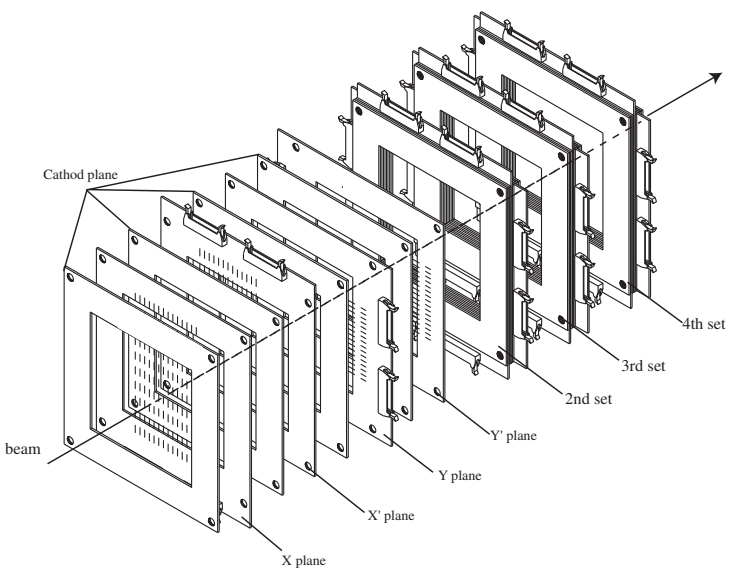

Figure 2.5: Schematic drawing of beam-line drift chamber (BLC).

[ii] In this work, the tracking efficiency is defined by the number of tracked events divided by the number of triggers.

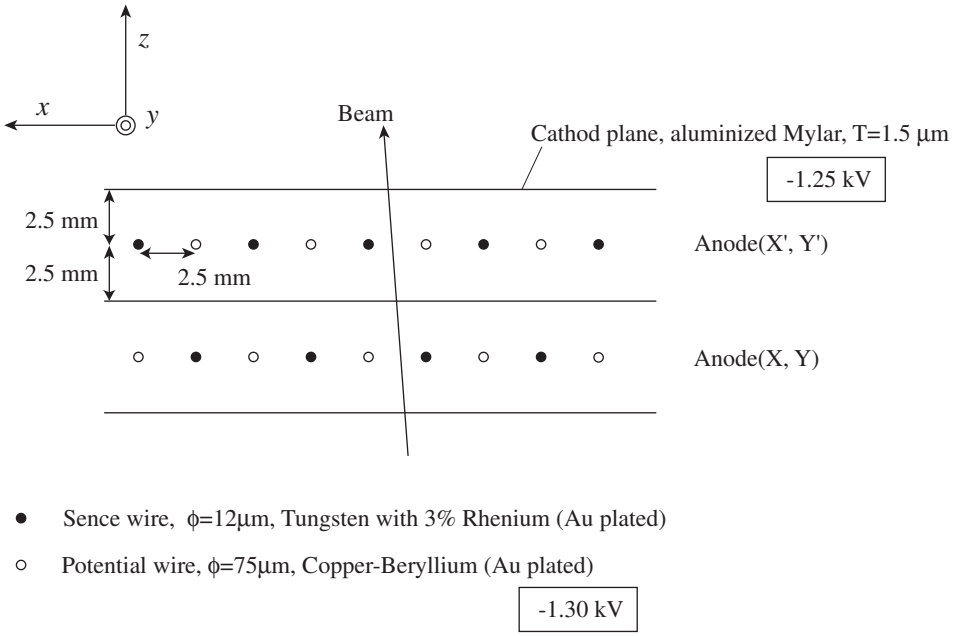

Figure 2.6: Cross-sectional view of the BLC and its structure.

2.4 Liquid Helium-4 Target

There were two crucial requirements for the target system of the experiment. First, the target must be covered by large-acceptance tracking devices to increase the geometrical efficiency for reconstructing vertex points. Second, the material surrounding the target must be reduced to not attenuate the X-rays from the target and to improve the position resolution of the vertex reconstruction. The first requirement was realized by using a long-tube-type vacuum vessel. To keep 1 atmosphere pressure in the vessel and to reduce the material between the target and tracking devices, 0.9-mm-thick Carbon Fiber Reinforced Plastic (CFRP) at a density of 1.70 g/cm^3 was used. The second requirement was realized by using superfluid liquid helium-4 as a target. One of the characteristics of the target is low pressure and high density. The low pressure made it possible to use a very thin Mylar-film cell, and the high density increased the stopping power for the K^- beam.

A schematic view of the target system is shown in Figure 2.7. The target was superfluid helium-4, 23.5 cm in diameter and 15.0 cm in thickness (2.18 g/cm^2) along the beam direction. The cylindrical cell was made of a 0.8-mm-thick aluminum frame which had two types of windows, 75.0 μm thickness of Mylar for the beam direction and 188 μm thickness of Mylar for the side of the PDC-acceptance direction. Our X-ray detectors could view the target through the thin 75.0 μm Mylar, so the attenuation loss at the window is only 13% for 6.4 keV X-ray. To contain the contamination X-rays from the target cell, 0.3 mm in thickness pure-aluminum foils were put on the inner surface of the cell.

The thermal-radiation shield around the target was created by 0.3-mm-thick pure aluminum sheets put on a 0.6-mm-thick aluminum frame. As is the case of the target cell, since the purity of the frame was not as high so its inner surface was covered with additional 0.3-mm-thick pure aluminum foils to shield the contamination X-rays in induced by the beam. The thermal-radiation shield was cooled by liquid nitrogen (∼77 K). The cooling fingers of X-ray detectors were connected with the thermal-radiation shield. As a result X-ray detectors were cooled down to ∼ 83 K during the experiment.

To minimize the flight-time dependence on K^- beam stopping positions, 0.3-cm-thck carbon degrader (0.6 g/cm^2) was installed just in front of the thermal-radiation shield.

To realize the in-beam calibration using characteristic X-rays of titanium and nickel induced by the charged particles (mainly contamination pions), pure-metal foils were put on a pure-aluminum cone-shape support just downstream of the target. The foil specification is summarized in Table 2.2.

Table 2.2: Specification of pure foils used for in-beam calibration.

Foil	Purity (%)	Thickness (mm)	Location
Ti	99.99+	0.05	aluminum cone support downstream of the target cell
Ni	99.999	0.125	aluminum cone support
Al	99.999	0.3	inner surface of the target inner surface of the radiation shield

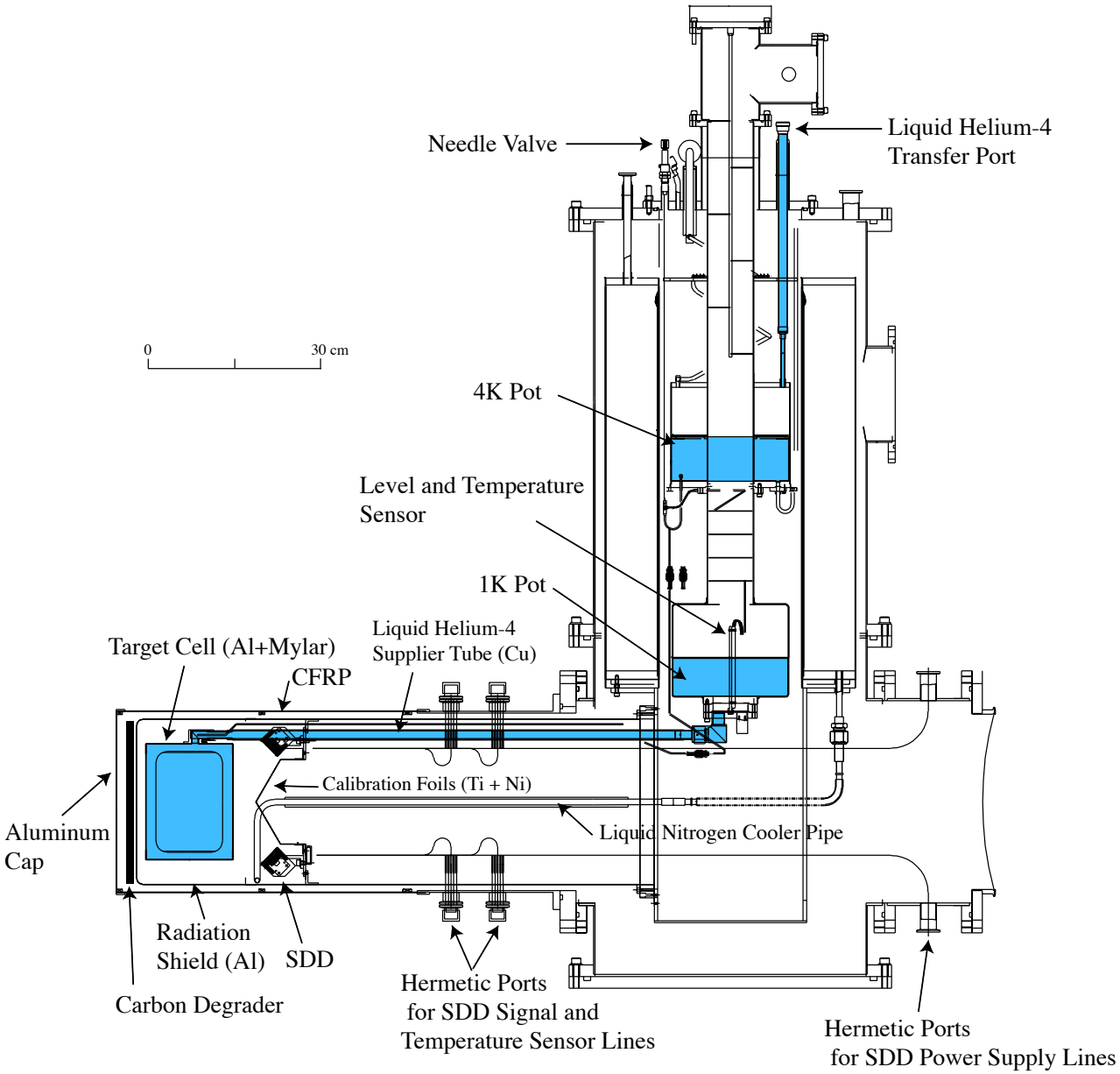

Figure 2.7: Schematic view of the target system.

2.5 Vertex Detector System

The detector system to reconstruct the reaction vertex of a K^- and a target nucleus consisted of two types of drift chambers, a vertex drift chamber (VDC) and a proton drift chamber (PDC). A sufficient number of plastic scintillation counters covered the chambers to trigger the secondary charged particles. We call these counters TC for the VDC, PA and PB for the PDC.

2.5.1 Vertex Drift Chamber

The VDCs were installed at the top and bottom of the target. They covered about 34% of the total solid angle from the view point of the target center. The charged particles emitted from the target were tracked by the VDC to reconstruct a reaction point of the stopped K^- using a track from the BLC.

Figure 2.8 shows a schematic view of the bottom VDC. Each VDC consisted of four modules (X1, Z1, X2, Z2). Each module was composed of three sensitive planes (X,X′,X″), Figure 2.9 shows its hexagonal-cell structure. The negative-high voltages were -2.60 kV and -2.35 kV for potential wires and guard wires, respectively. The sense and potential wires were made of gold-plated tungsten with 3% rhenium ($\phi 30$ μm) and gold-plated copper-beryllium ($\phi 100$ μm), respectively. The sense-wire spacing was 2 cm, and the number of channels was 420 for each VDC. The total of 840 channels were read by $28 \times 2 = 56$ ASDs. Each VDC was operated with Ar-isobutane 1 : 1 gas mixture. The typical gas consumption was 80 cc/min, and the typical tracking resolution and efficiency of the VDCs are summarized in Table 2.3.

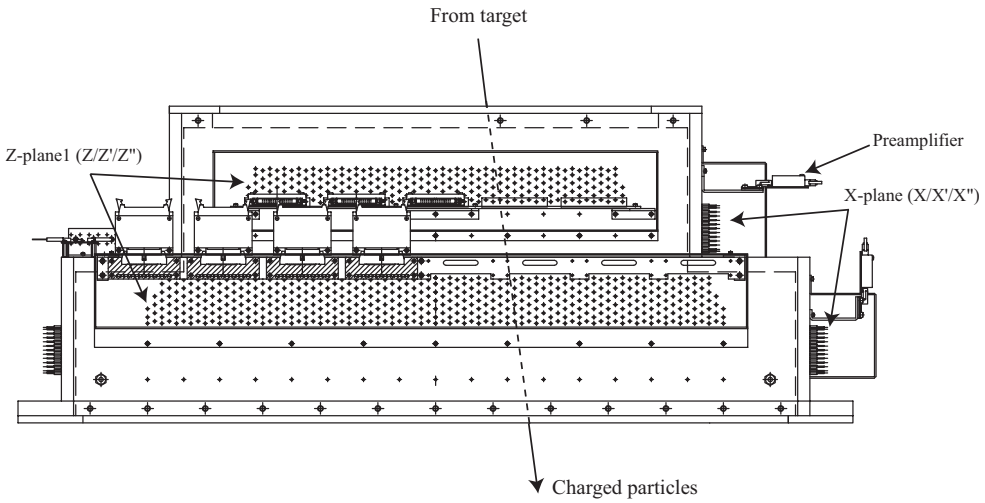

Figure 2.8: Schematic drawing of the bottom VDC.

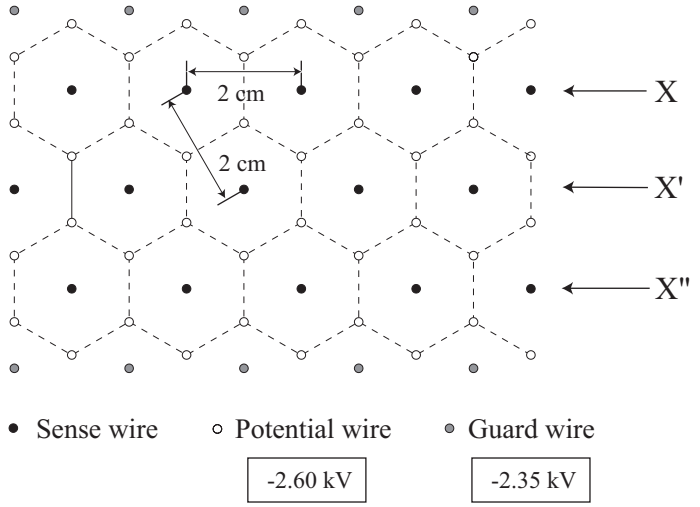

Figure 2.9: Cross-sectional view of a VDC and its cell structure.

Table 2.3: Typical tracking resolution and efficiency of the VDCs.

Experiment	VDC	resolution σ (mm)	efficiency (%)
E570 first cycle	top	0.33	40
	bottom	0.25	43
E570 second cycle	top	0.33	40
	bottom	0.25	44

2.5.2 Proton Drift Chamber

The PDCs were installed just left and right of the target to track the charged particles emitted from the target. It covered 7.2% of the total solid angle from the view point of the target center.

A PDC had the same configuration as half of a BLC. The difference was the 4.0-mm sense-wire spacing for PDCs. Figure 2.10 shows a wire structure and a cross-sectional view of the chamber. The negative-high voltages were -1.25 kV and -1.25 kV for cathode planes and cathode wires, respectively. Each PDC was operated with Ar - isobutane 80 : 20 gas mixture with a small amount of methylal. The typical gas consumption was 35 cc/min.

The tracking resolution of a PDC was $\sigma \sim 0.14$ mm for xz and xy planes, and the tracking efficiency was about 37% during the first cycle of E570.

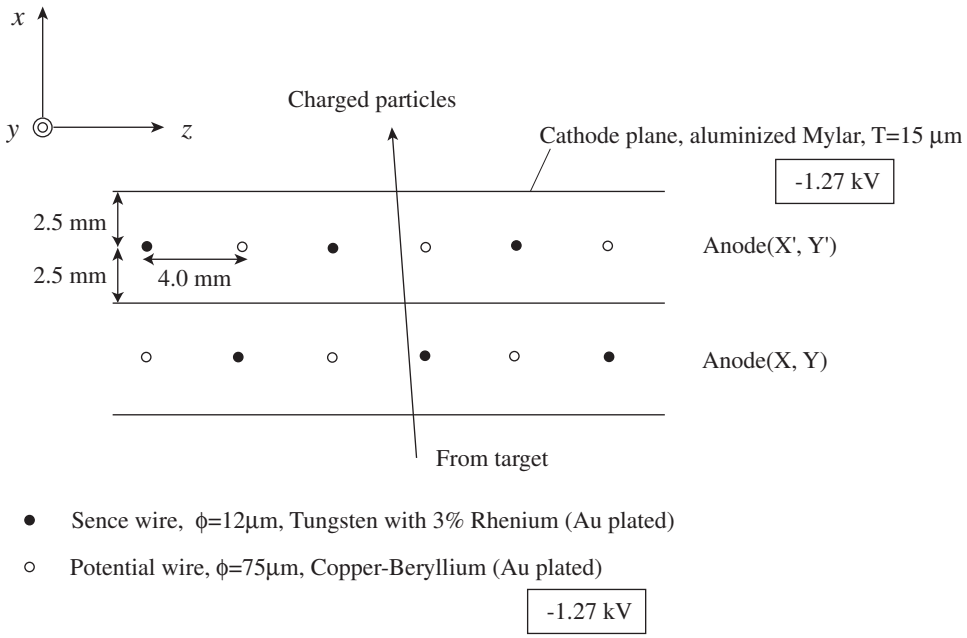

Figure 2.10: Wire structure and cross-sectional view of a PDC.

2.6 X-ray Detector System

Our goal is to measure the kaonic-helium X-rays whose energy is about 6.4 keV with a statistical accuracy of $\sim$ 2 eV. To realize this accuracy three features were required for the X-ray detector; 1) good energy resolution, 2) a very thin detector to reduce the background due to the Compton scattering in the detector and 3) a large effective area. Silicon drift detectors (SDDs) were chosen.

In this section, a brief description of SDDs is given, and the readout system of the raw signal from a SDD to the input of an ADC will be described later.

2.6.1 Silicon Drift Detectors

SDDs are based on the principle of sideward depletion introduced by Gatti and Rehak in 1984 [19]. Figure 2.11 shows a schematic cross-section of a cylindrical SDD. Electrons are guided by an electric field to the collecting anode in the center. This type SDD is operated with three external-voltage supplies for the back contact p^+ junction and first and last p^+ rings.

The good resolution is realized by the small value of the anode capacitance, which is almost independent of the detector area. Compared to a conventional Si(Li) detector of equal size, the resolution of a SDD is about twice better, and it is about 10 times thinner. As a result, the background of the Compton scattering occurring in the detector is suppressed about one order of magnitude.

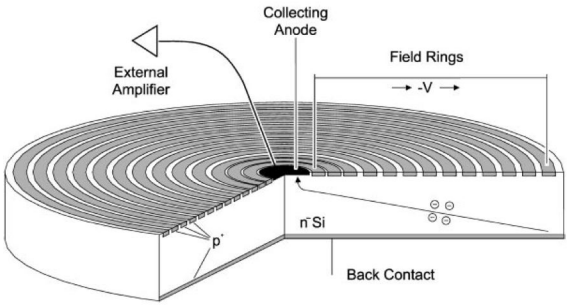

Figure 2.11: Cross-section view of a silicon drift detector (SDD). Electrons are guided by an electric field to the collecting anode in the center [20].

The SDDs used for the experiment were produced by Ketek GmbH. Each SDD had 100 mm^2 effective area and about 260 μm thickness. Its entrance window was created as a hexagonal shape, and the SDD chip was mounted on a 20-pin ceramic board. The signal and high-voltage-supply wires were bonded with gold on the board. The bonding plan is shown in Figure 2.12. Negative high voltages were supplied to Ring 1, Ring X and Back pins, and the OS and IS pins were connected to a ground line. Signal lines consisted of five independent lines, Feed Back (FB), Drain, Reset, Bulk (SUB) and Source.

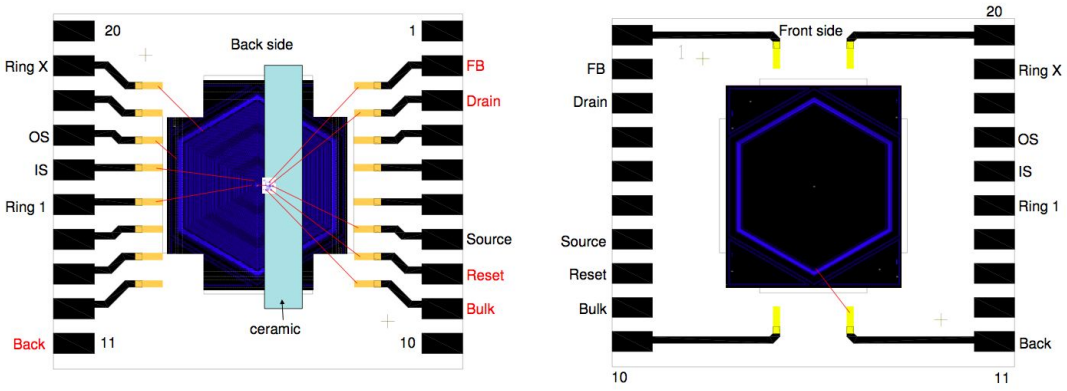

Figure 2.12: Bond plan of the 100 mm^2-SDD used for the experiment, produced by Ketek GmbH. The FET is located on the ceramic bridge just backside of the small anode. Wires are bonded with gold (yellow square).

We used 8 SDDs and tilted them 45 degrees to see the center of the target. The most important point was to hide the SDD chip from the view of contamination materials around the target. To shield the contamination X-rays induced by the beam or charged particles, we covered the SDD with a 3-mm-thick pure aluminum plate which had a window to see the target. Figure 2.13 shows a schematic drawing of the setup. The SDD-holder drawing is also shown in Figure 2.14.

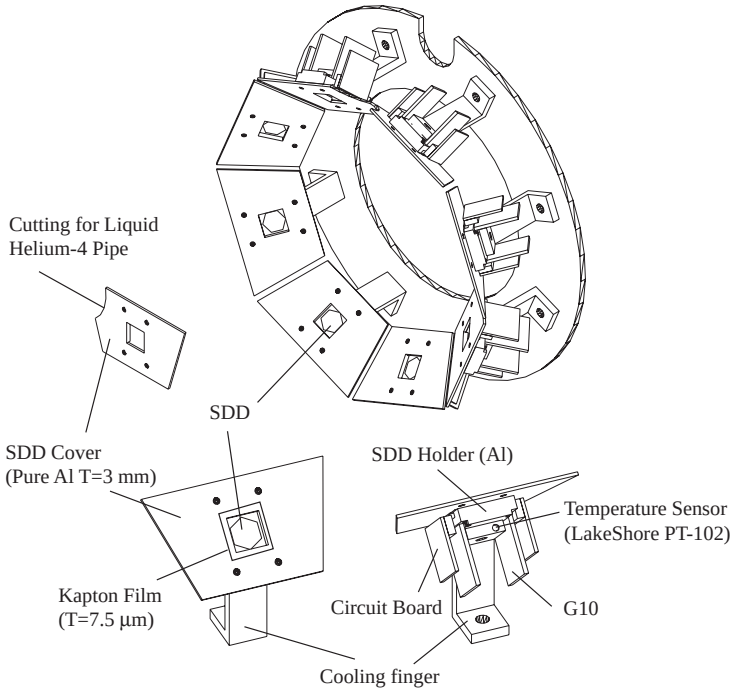

Figure 2.13: Schematic view of 8 SDDs and their support. The SDDs were tilted 45 degrees to see the center of the target. To shield the contamination X-rays, each SDD was covered with a pure-aluminum plate which had a square window.

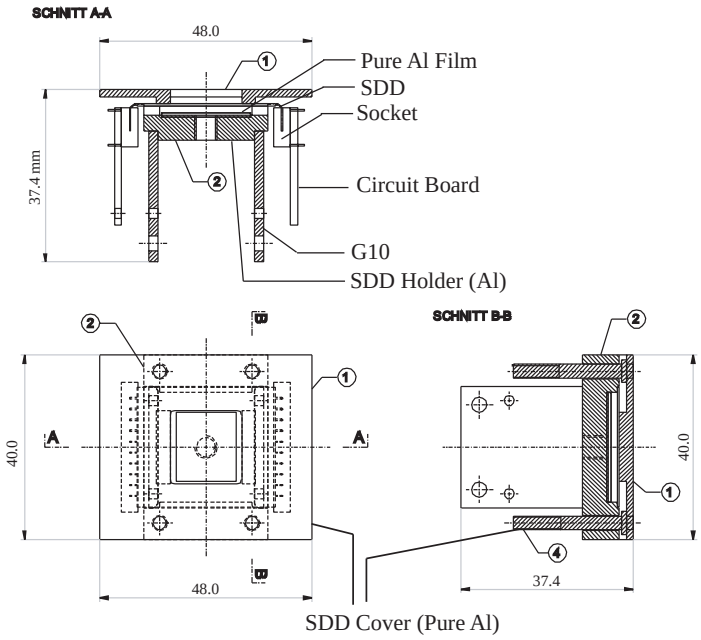

Figure 2.14: Design of the SDD-holder. Since the purity of aluminum used for the holder was not so good, a pure-aluminum film was put on between the SDD and the holder.

The SDDs were cooled by liquid nitrogen through their cooling fingers attached on the SDD support. The temperature of the SDDs was measured by LakeShore PT-102 sensors and monitored by a LakeShore-340 with a GPIB controller. Although two heaters were set just below the SDD support, they were not used. Because the equilibrium temperature ($\sim$83 K) was more stable than with heaters on, and because the FET worked well enough at that temperature.

2.6.2 Signal Readout System

A schematic diagram of the signal flow from the SDD is shown in Figure 2.15. The charge-pulse signal from the SDDs was taken out through hermetic ports. The cable length between the SDD and the preamplifier was about 70 cm. This length was near a limit of the tolerable cable capacitance. When we used thick cables or longer cables, the signal caused resonance with the cable capacitance. The feedback line (FB) was made of an especially-thin single wire ($\phi = 0.32$mm).

The charge pulse was integrated by the charge-sensitive preamplifier. The transistor reset method was used to eliminate the feedback resistance. This resulted in suppressing the thermal-noise contribution to the preamplifier noise. On the other hand, a giant negative pulse invoked an overshoot peak just after the reset timing. This was because a hardware VETO was needed to not trigger the reset peak (Reset VETO). Moreover, the reset pulse caused cross talk with the neighboring SDD

which shared a hermetic port. This was also included in hardware VETOs.

The output signal of the preamplifier was amplified and shaped by a CAEN 16-channel spectroscopy amplifier module in the experimental area. This amplifying and shaping made it possible to minimize the noise pick-up during transmission of the signal through a 15 m BNC cable from the experimental area to the counting room.

The CAEN shaping amplifier had 16 inputs, 16 outputs (OUT), 16 fixed-gain outputs (XOUT) and 16 fast-timing outputs (FOUT). The front panel is shown in Figure 2.16. We used 8 channels of OUT as ordinary-shaped outputs with 3 μs shaping time and the other 8 channels as the timing of the SDD triggers with 0.2 μs shaping time. The FOUT had a 100 ns differentiation-time constant and its typical rise time was 25 ns. This fast-timing lines were delayed using 120 m BNC cables to coincide with the timing of OUT. In order to convert the output connector, 17+17 pin double-row-strip header, into 16-channel LEMOs, we used a conversion board (Figure 2.17). The cross talk in the connector was tested and it was only 0.2% of the neighboring outputs.

We used three types of ADCs, peak-hold ADCs, flash ADCs and Wilkinson-type ADCs. Since the Wilkinson-type ADC had a bit-inverse problem for its bottom two bits and a large differential-non-lineality, it was not analyzed.

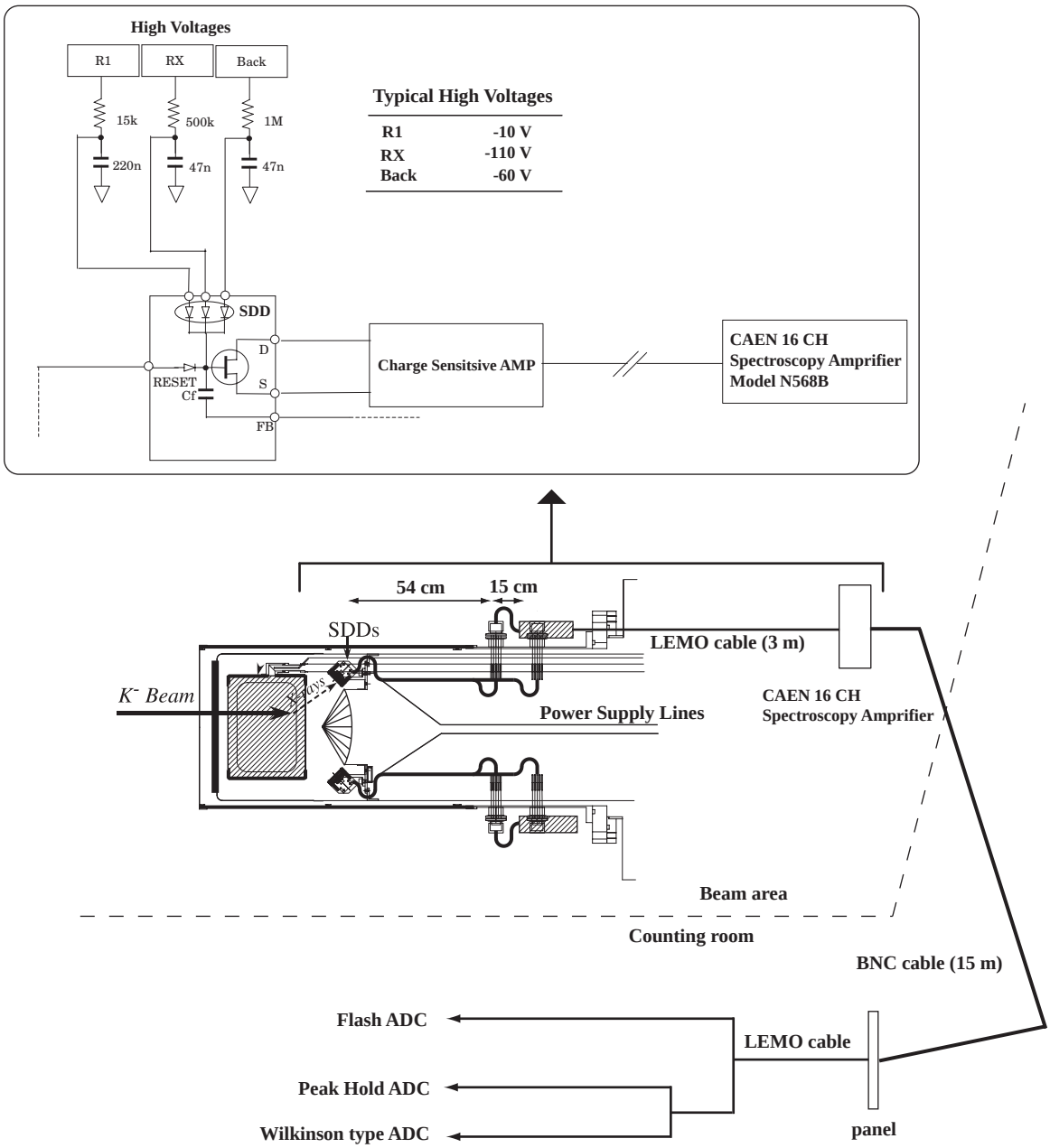

Figure 2.15: Schematic diagram showing the flow of the signal from the SDDs. The shaping amplifier was in the experimental area to minimize the noise pick-up during transmission of the signal. We used three types of ADCs, peak-hold ADCs, flash ADCs and Wilkinson-type ADCs, for data taking.

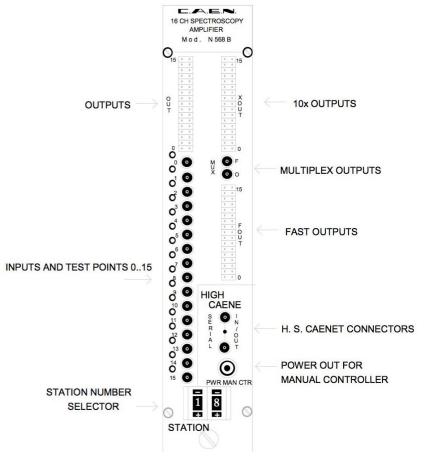

Figure 2.16: Front panel of a CAEN spectroscopy amplifier module.

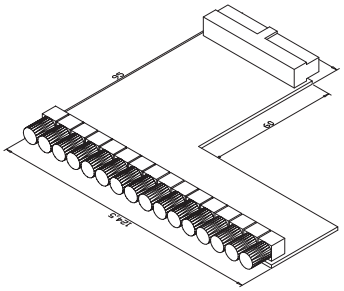

Figure 2.17: Conversion board from the double-strip-header connector into LEMOs.

2.7 Trigger Logic and Data Acquisition System

The pulse-height data and timing information of all the raw signals were fed into the ADC and the TDC modules of the TKO standard which was developed at KEK. In addition, VME scalers were read spill-by-spill.

In E570, we constructed three types of trigger logic, "E549 trigger", SDD self-trigger and flash ADC trigger. In this section, the details of them are described.

2.7.1 E549 Trigger

The E570 experiment was carried out in conjunction with the search for deeply-bound $\bar{K}$-nucleus states in ^{4}He(*stopped* K^-, N) reactions (KEK-PS E549). The E549 trigger was constructed to tag the secondary charged particles for the reconstruction of the kaon-reaction vertex.

A logic diagram of the E549 trigger is shown in Figure 2.18. The E549 trigger consisted of a kaon beam trigger, a PA-PB-coincidence trigger for the PDC and a TC trigger for the VDC. The stopped-kaon trigger was constructed by the coincidence of the incident-kaon trigger and VETO counters on the beam line and downstream of the cryostat. Finally, "Kstop Charged" and "Kstop VTC" were constructed, and their OR trigger retimed by the T1 was the hardware-level E549 trigger. At the off-spill timing, the cosmic-ray trigger was included in order to calibrate the chambers. Therefore the E549 trigger condition was

$$\text{E549 Trigger} = (\text{Kbeam/prescale}) \cup \text{Kstop} \cdot (PA \cap PB) \cup \text{Kstop} \cdot \text{VTC} \qquad (2.1)$$

where,

$$\text{Kbeam} = T0 \cap T1 \cap \overline{(LC1 \cup LC2)}, \quad (2.2)$$

$$\text{Kstop} = \text{Kbeam} \cap \overline{\text{KstopVETOs}} \quad (2.3)$$

The typical trigger rate of Kstop-Charged and Kstop-VTC were 100/spill and 700/spill, respectively.

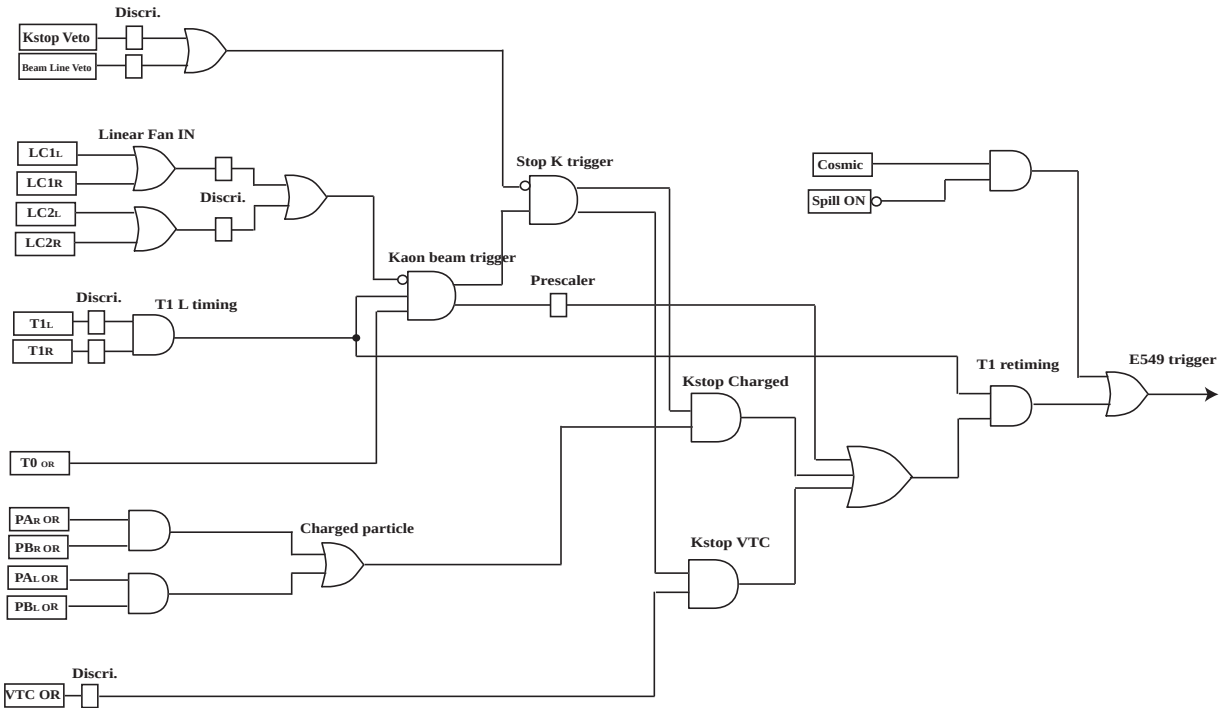

Figure 2.18: E549 trigger logic diagram.

2.7.2 SDD Self Trigger

A logic diagram of the SDD self-trigger is shown in Figure 2.19. To suppress the trigger rate, two leading-edge-type discriminators were used with different thresholds. One was "lower" for getting the trigger of X-ray events, and the other was "upper" for eliminating the overflow events due to charged-particle direct hits (mainly by pions in the beam). The "upper" was coincided with the "lower" as a VETO. Finally, the SDD self-trigger was constructed by the coincidence of three types of VETO and the spill-on timing. The typical rate of self triggers per SDD was 30/spill.

There was an additional discriminator "lower-2." This was introduced to see the much lower energy region by offline cuts using TDC data (SDDT3). However,

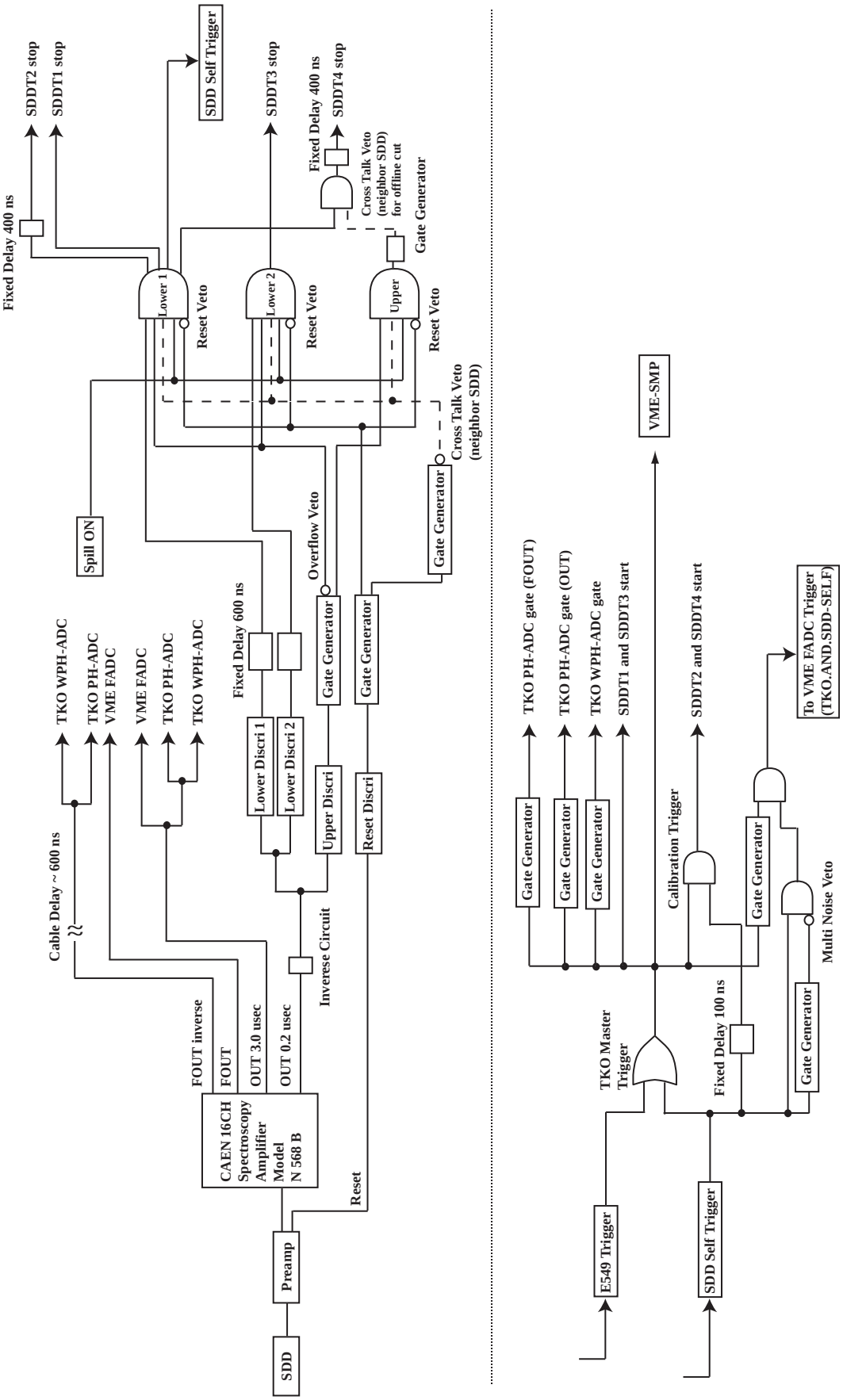

Figure 2.19: SDD self trigger logic diagram.

the noise level was too high to analyze, and the acceptance of the $\sim$ 2 keV X-rays generated in the target was too small due to attenuation.

The master trigger was defined by E549.OR.SDDSELF. A complicate point of this trigger system was that the E549 triggers came always *earlier* than the self-triggers in all *dual-triggered* events. Because the E549 triggers had nano-second-order timing in contrast with micro-second-order timing of the self-triggers. Moreover, since the analog-to-digital conversion time of all ADC and TDC modules was 200 μs, the self-triggers were killed when the E549 triggers came simultaneously. This means the E549 triggers were given priority over the self-triggers.

Four types of TDC data were taken to perform offline cuts. The summary is shown in Table 2.4. The incident-kaon timing was chosen by the SDDT1, and the energy calibration data were given by the SDDT2.

Table 2.4: Summary of TDC data for offline cuts.

TDC data	Start	Stop	Comment
SDDT1	E549	SDD self	to select the kaon beam timing
SDDT2	SDD self	SDD self (delayed)	for energy calibration
SDDT3	E549	SDD self (lower-2)	to see lower energy region (not used)
SDDT4	SDD self	SDD self (neighbor)	for cross talk VETO (not used)

2.7.3 Flash ADC Trigger

A logic diagram of the flash ADC trigger is shown in Figure 2.20. Since the flash ADC data were taken via VME system independently of the TKO side (peak-hold ADC data), the event verifying between TKO and VEM was a very important task.

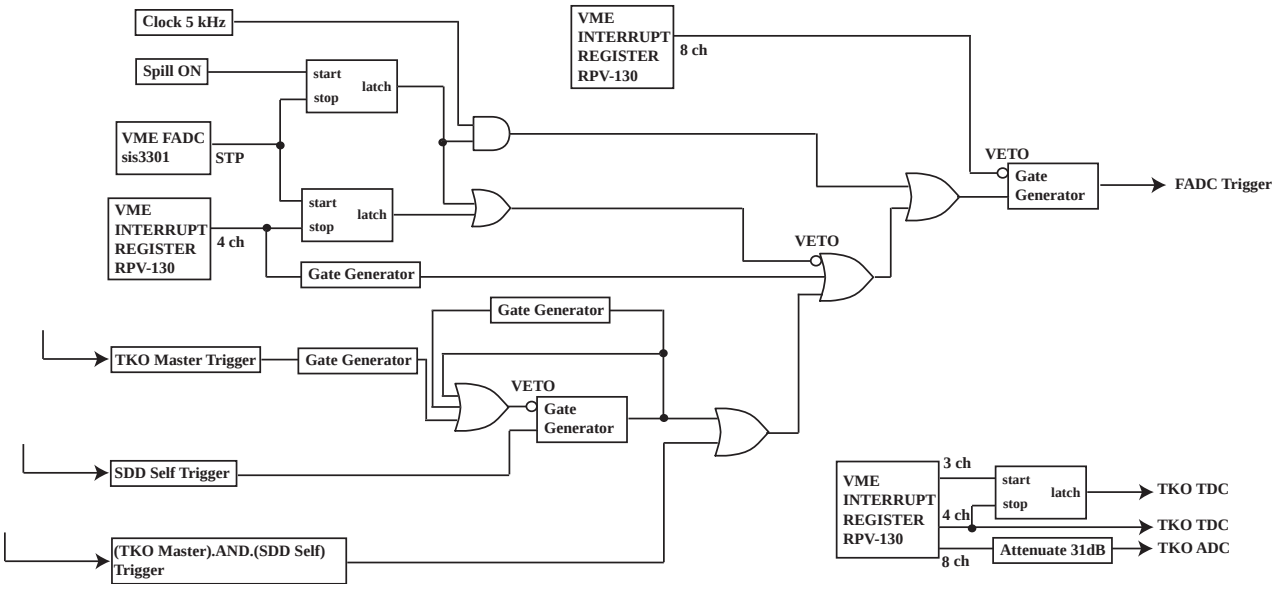

Figure 2.20: VME flash ADC trigger-logic diagram.

2.8 Experimental Conditions

Here the experimental conditions of SDDs, discriminators and gate-generators are summarized.

2.8.1 SDDs

Though we used 16 SDDs in total for the first and second cycles of E570, the number of well-conditioned SDDs was 10, three in the first cycle and seven in the second cycle. From now on, we regard the 10 SDDs as individual detectors and rename them as in Table 2.5. The detector numbers were defined along the clockwise direction as shown in Figure 2.21. Three SDDs (SDD2, SDD4 and SDD5) were used in both cycles of E570.

Table 2.5: Names of the SDDs. In the second cycle, the five SDDs were replaced by new detectors.

Experiment	Detector #	Name	Comments
First cycle	#1	SDD1-1st	not used
	#2	**SDD2-1st**	
	#3	SDD3-1st	not used
	#4	**SDD4-1st**	
	#5	**SDD5-1st**	
	#6	SDD6-1st	not used
	#7	SDD7-1st	not used
	#8	SDD8-1st	not used
Second cycle	#1	**SDD1-2nd**	new
	#2	**SDD2-2nd**	**same as SDD2-1st**
	#3	**SDD3-2nd**	new
	#4	**SDD4-2nd**	**same as SDD4-1st**
	#5	**SDD5-2nd**	**same as SDD5-1st**
	#6	SDD6-2nd	not used
	#7	**SDD7-2nd**	new
	#8	**SDD8-2nd**	new

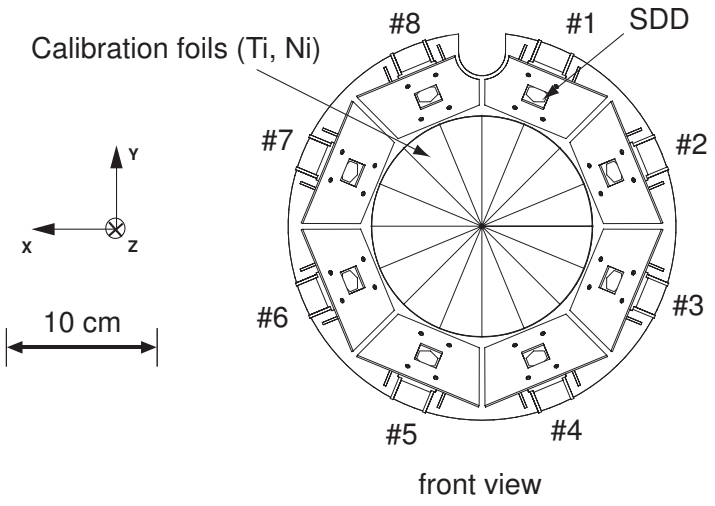

Figure 2.21: A front view of the SDDs assembly. The detector numbers are defined along the clockwise direction.

The negative high-voltages were summarized in Table 2.6

Table 2.6: The negative high-voltages of the SDDs (see Figure 2.12 for the line names).

Detector	Ring X (V)	Ring 1 (V)	Back (V)
SDD2-1st	-110.5	-10.36	-64.3
SDD4-1st	-99.8	-5.99	-64.2
SDD5-1st	-105.0	-10.44	-63.2
SDD1-2nd	-107.4	-9.97	-59.6
SDD2-2nd	-110.3	-10.05	-64.2
SDD3-2nd	-109.7	-9.63	-60.0
SDD4-2nd	-99.5	-5.93	-59.9
SDD5-2nd	-105.0	-10.05	-63.2
SDD7-2nd	-109.4	-10.43	-64.1
SDD8-2nd	-105.4	-9.93	-62.4

2.8.2 Discriminators

The thresholds of the discriminators are summarized in Table 2.7.

Table 2.7: The thresholds of the discriminators.

Detector	Lower (mV)	Upper (mV)	Reset (mV)
SDD2-1st	-202.8	-899	-47.4
SDD4-1st	-202.8	-822	-53.6
SDD5-1st	-203.6	-852	-44.9
SDD1-2nd	-119.0	-803	-44.7
SDD2-2nd	-100.3	-807	-48.6
SDD3-2nd	-121.3	-800	-51.7
SDD4-2nd	-91.7	-819	-57.1
SDD5-2nd	-129.7	-849	-45.6
SDD7-2nd	-109.3	-795	-45.3
SDD8-2nd	-138.5	-807	-45.0

2.8.3 Gate Generators

The VETO widths are summarized in Table 2.8. The reset timing period was about 30 ms and 50 ms for the first and second cycles of E570, respectively. The external-gate width of the peak-hold ADCs was 7.9 μs and 2.9 μs for the OUT and FOUT signals, respectively.

Table 2.8: The VETO widths.

Detector	Reset VETO (ns)	Upper VETO (ns)	Cross Talk VETO (μs)
SDD2-1st	400	620	–
SDD4-1st	510	610	14.8
SDD5-1st	400	610	–
SDD1-2nd	600	500	13.0
SDD2-2nd	400	880	10.0
SDD3-2nd	400	820	15.0
SDD4-2nd	500	805	13.8
SDD5-2nd	400	840	13.6
SDD7-2nd	600	2080	15.0
SDD8-2nd	296	2880	15.0

2.9 Data Summary

Table 2.9 shows the data summary for E570 first cycle and second cycle. N_{K^-} and N_{π^-} denote the number of particles detected at Lucite Čerenkov counters. In the second cycle, the K/π ratio was improved by the separator-voltage tuning (see section 2.2.2). The number of SDD self-trigger was included in that of Trigger (for example, the 46 M self-tirggers of the first cycle were included in the 450 M triggers). These numbers were given by VME-scaler data.

Table 2.9: Data summary of E570 first cycle and second cycle. N_{K^-} and N_{π^-} denote the number of particles detected at Lucite Čerenkov counters.

Experiment	Date	Time	N_{K^-}	N_{π^-}	Trigger	SDD self
E570 first cycle	2005/Sep/27-Oct/31	536 h	2.7 G	660 G	450 M	46 M
E570 second cycle	2005/Dec/13-Dec/28	272 h	1.1 G	210 G	180 M	50 M

Chapter 3

Analysis I : Detector Analysis

3.1 Overview

The off-line detector analysis procedure is described in this chapter. Two stages of analysis were carried out as follows:

3.1.1 Target Fiducial Volume Cuts

A K^- reaction point was reconstructed as a vertex of the K^- beam track and the emitted charged particle track measured by the BLC and the VDC/PDC, respectively. We can define the target-fiducial-volume cuts by the vertex coordinates of the events in which an incident K^- reacted in the helium-4 target. This procedure makes it possible to reduce the background coming from outside the target. However, the number of real X-ray events are also reduced depending on the tracking efficiencies.

3.1.2 Silicon Drift Detectors

The SDD signals which have a hit coincidence with the E549 trigger can be selected by the TDC data of SDDT1. It is easy to select the incident kaon timing by seeing a correlation between TDC and ADC. Finally, by applying the target fiducial volume cuts using reconstructed vertices, we are able to obtain X-ray energy spectra.

At the same time, the calibration data can be selected by the SDDT2 data. The gain drifts of SDDs are able to be corrected by the in-beam calibration.

3.2 Target Fiducial Volume Cuts

A vertex was reconstructed by a incident-beam-particle track and a secondary-charged-particle track. In this section, the target images obtained from a K^- beam run are shown, and the target fiducial volume cuts are defined.

3.2.1 BLC-VDC Images

Figure 3.1 shows the target image of the yz-vertex reconstructed by the BLC-VDC, and Figure 3.2 shows its projection on the z coordinate (beam direction). The images of the carbon degrader, the liquid ^{4}He target and the SDDs were clearly separated. The target region was selected as -70.0 mm $\leq z \leq 90.0$ mm.

The yx vertex image with selection of the above z vertex region is shown in Figure 3.3, and its projection on the radius coordinate is also shown in Figure 3.4. The target region was selected as $r \leq 110.0$ mm loosely.

3.2.2 BLC-PDC Images

Here, the images of BLC-PDC were checked. They are consistent with the BLC-VDC images. The target region selections were just same as the case of BLC-VDC.

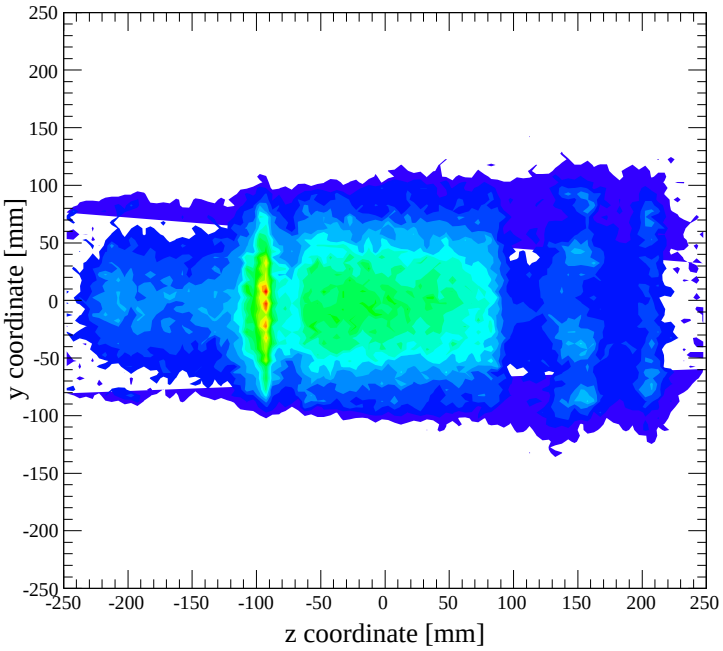

Figure 3.1: Distribution of yz vertex points reconstructed by BLC-VDC.

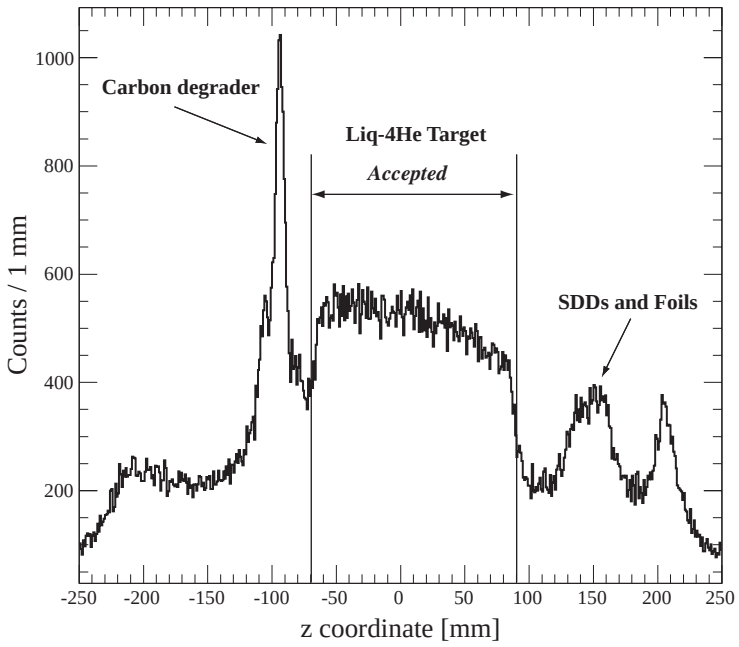

Figure 3.2: Distribution of z vertex points reconstructed by BLC-VDC. Carbon degrader, liquid ^{4}He target and SDDs images were clearly seen. The target region was selected as -70.0 mm $\leq z \leq 90.0$ mm.

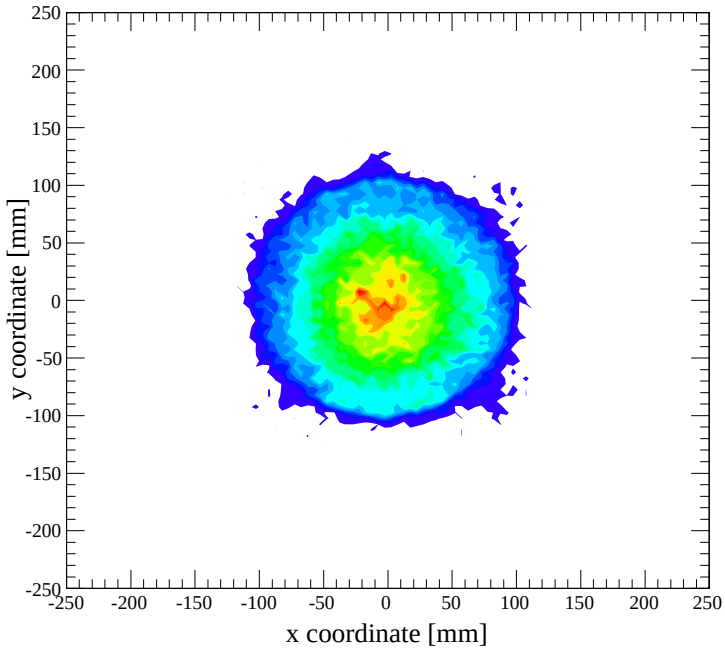

Figure 3.3: Distribution of yx vertex points reconstructed by BLC-VDC. The z vertex was already selected by the above target region.

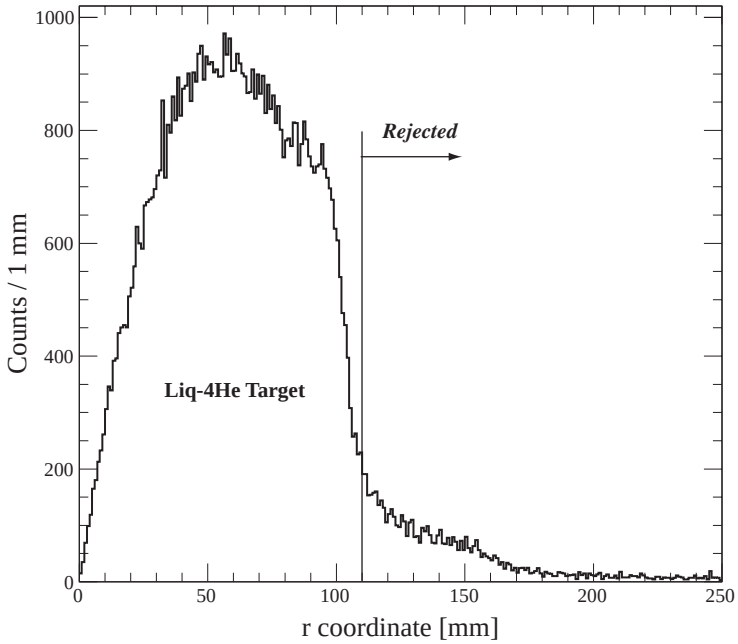

Figure 3.4: Distribution of vertex points in radius coordinate reconstructed by BLC-VDC. Here, the target region was selected as $r \leq 110.0$ mm.

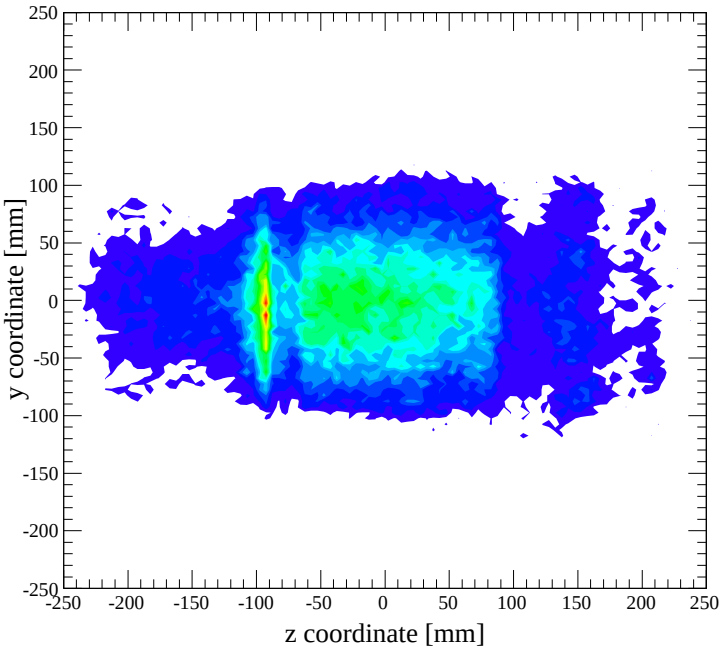

Figure 3.5: Distribution of yz vertex points reconstructed by BLC-PDC.

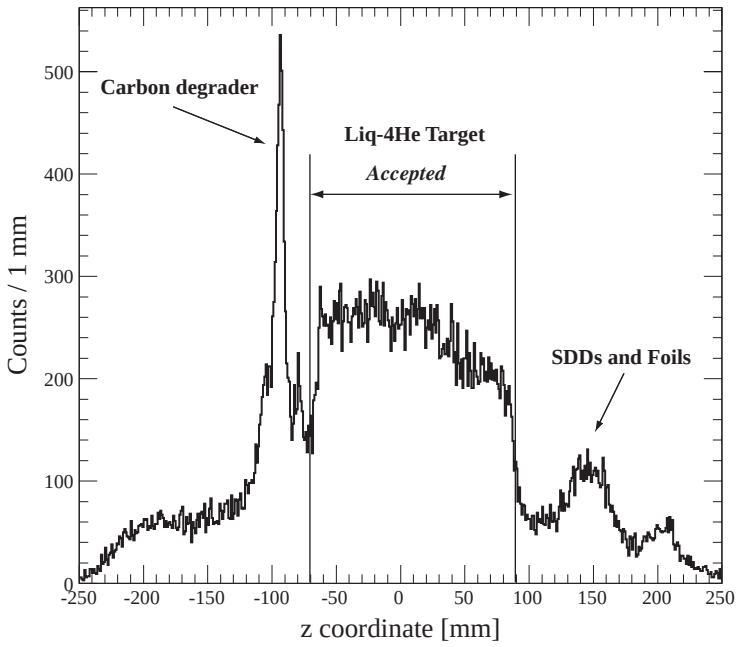

Figure 3.6: Distribution of z vertex points reconstructed by BLC-PDC. Carbon degrader, liquid ^{4}He target and SDDs images were clearly seen. The target region was selected as -70.0 mm $\leq z \leq 90.0$ mm.

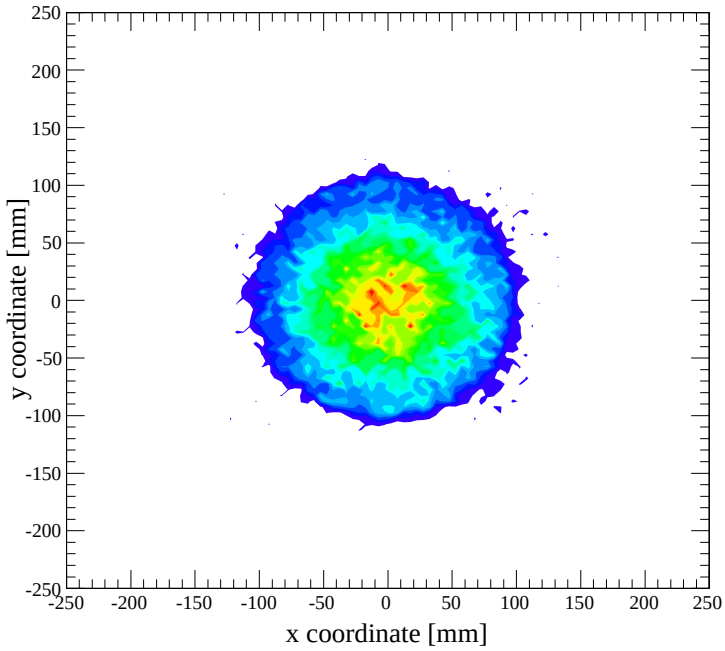

Figure 3.7: Distribution of yx vertex points reconstructed by BLC-PDC. The z vertex was already selected by the above target region.

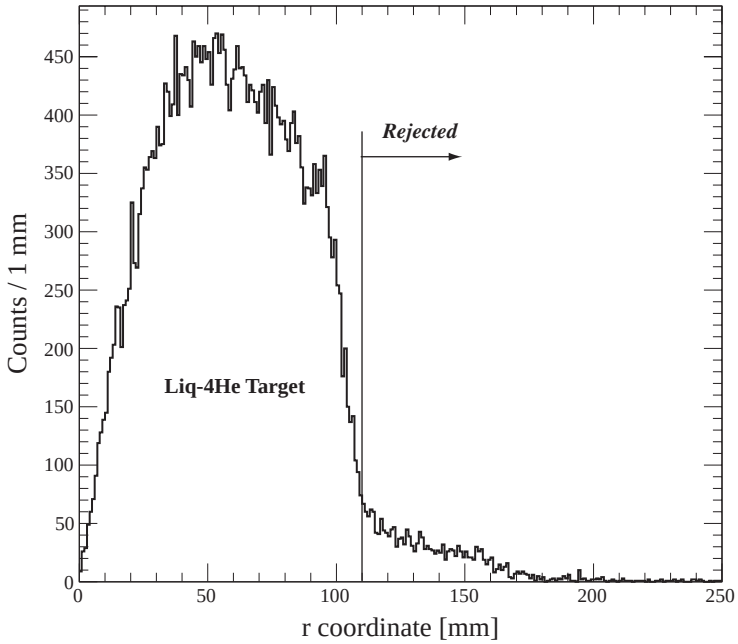

Figure 3.8: Distribution of vertex points in radius coordinate reconstructed by BLC-PDC. Here, the target region was selected as $r \leq 110.0$ mm.

3.3 Silicon Drift Detectors

3.3.1 Run Packing

The data were taken in about 2-hour interval which was so-called "run". Since the time-depedent gain drifts of the SDDs influence the accuracy of the energy calibration, the calibration should be performed as often as possible in short intervals. In contrast, the statistics of the calibration data taken in a run was limited, we must do pack some runs.

We employed two criteria to ensure the run packing was optimized. One of them was pedestal fluctuations of SDDs, and the other was statistical error associated with conversion to energy from ADC channel.

- **Pedestal**

The pedestal of the SDDs had only $\sim \pm 3$ eV fluctuation through out the experiment. Since some jumping was observed once in a while, we considered the jumping and run breaks in the run packing.

- **Statistical Error Associated with Converted Energy**

When we convert an ADC channel into an energy, an unavoidable quantization error exists. The error is

$$\sigma_Q^2 \approx \frac{\Delta^2}{12} \tag{3.1}$$

where Δ is the width of the quantization region. In addition, the statistical error of the calibration parameters must be considered when we estimate the converted energy. The total error is

$$\sigma_C \approx \sqrt{\sigma_Q^2 + \sigma_S^2} \tag{3.2}$$

where σ_S is the statistical error. Needless to say, the smaller σ_S is, the better for the calibration. Since the amount of data was limited, we must find a point of compromise. Here, we kept the σ_S smaller than the quantization region Δ. This means the energy was converted within the quantization region with more than 68.3% probability.

We could check the run packing relevance by comparing the width of the calibration peaks. An estimation of the systematic error associated with this procedure will be described in section 4.2.2.

3.3.2 In-beam Stability

Titanium and nickel K_α X-rays were used to monitor the gain and its stability when the beam was on. The shift of the interval between these two peaks indicate the changes of gain and pedestal.

A typical spectrum of the self-triggered events used for in-beam calibration is shown in Figure 3.9. The calibration data of this spectrum was accumulated for about 26.5 hours at the second cycle of E570. We fitted this spectrum with six Gaussians and a 2-dimensional polynomial function. The Gaussians were composed of Ti $K_{\alpha1}$, Ti $K_{\alpha2}$, Ti K_β, Ni $K_{\alpha1}$, Ni $K_{\alpha2}$ and Ni K_β.

The intensity ratio of $K_{\alpha1}$ to $K_{\alpha2}$ was fixed to a known value [21] in the fit, this was because the magnitude of X-ray attenuation effect was almost the same. The centroid of the $K_{\alpha2}$ peak was also fixed to the energy difference between $K_{\alpha2}$ and $K_{\alpha1}$. The width of $K_{\alpha2}$ was fixed by using a resolution function mentioned later. On the other hand, all K_β parameters were treated as free. This means the K_β lines were regarded as background. We used only K_α lines for energy calibration.

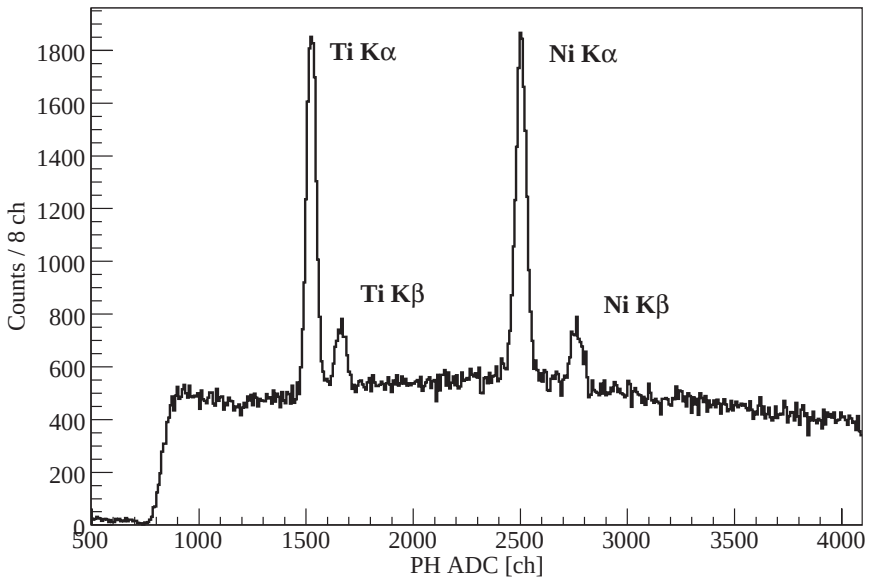

Figure 3.9: Typical spectrum of SDD self-triggered data used for in-beam energy calibration. Ti and Ni peaks are clearly observed. The horizontal axis is peak-hold ADC channel, the peak around 1500 ch corresponds to TiK_α energy 4.5 keV.

As is usually the case for silicon detectors, we assumed the energy resolution had the following energy dependence,

$$\Delta E(\mathrm{FWHM}) = 2.35\ \omega\sqrt{N^2 + \frac{FE}{\omega}}\ \ [\mathrm{eV}] \tag{3.3}$$

where N is noise (independent of the X-ray energy), E is the X-ray energy, F is the Fano factor and ω is the amount of energy needed to create an electron-hole pair (3.81 eV at 77 K). Because of the good energy resolution of the SDDs, the energy dependence term can not be negligible in the region of interest. Therefore, we introduced two parameters, N and F, in our fits. N was based on the value at Ti $K_{\alpha 1}$. The free Fano factor enabled us to treat the temperature difference of the SDDs. The fitted values of the Fano factor are shown in Table 3.1. A measured value of a SDD was 0.123±0.002 at 5.9 keV (−30°C) [22].

Table 3.1: Free Fano factors of the SDDs. The fitted values of the individual SDDs are listed.

Detector	Fano factor
SDD2-1st	0.154±0.005
SDD4-1st	0.139±0.005
SDD5-1st	0.182±0.008
SDD1-2nd	0.135±0.006
SDD2-2nd	0.159±0.009
SDD3-2nd	0.172±0.008
SDD4-2nd	0.148±0.006
SDD5-2nd	0.166±0.008
SDD7-2nd	0.179±0.012
SDD8-2nd	0.154±0.007

The energy resolution of SDD2-1st and SDD1-2nd as a function of the run-packing number is shown in Figure 3.10 and Figure 3.11, respectively. The energy resolution seems to be stable through the experiment from these figures. Although more run-packing may be expected, the time-dependent gain drifts must be considered.

To estimate the gain drifts, we paid attention to the converted energy from the 2000 ch of peak-hold ADC. The converted energy of SDD2-1st and SDD1-2nd as a function of the run-packing number is shown in Figure 3.19 and Figure 3.20, respectively. In sharp contrast with the energy resolution, the gain drifts were large. This was because we must be careful in packing the runs.

The attached errors were statistically derived from the error propagation on the conversion process. The distribution of the error against ADC channel is shown in

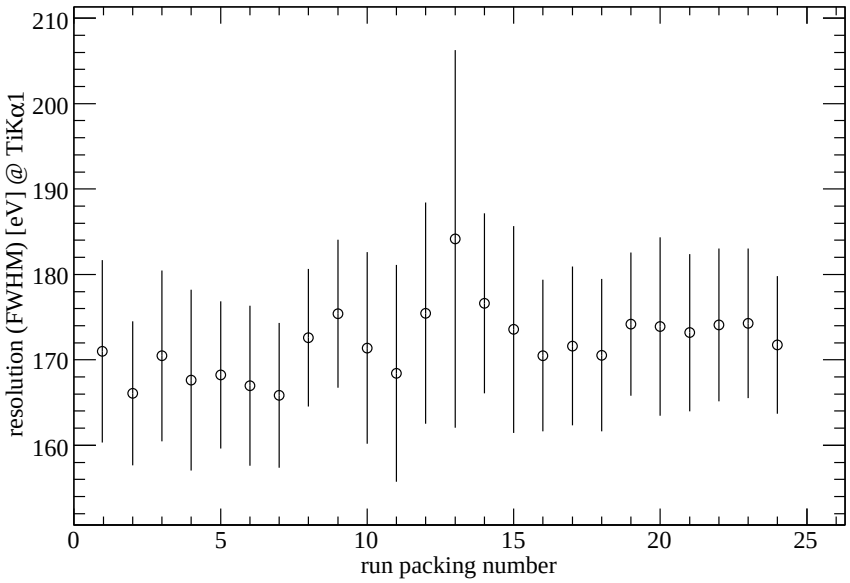

Figure 3.10: Energy resolution of SDD2-1st as a function of the run-packing number. The large error point at 13 is K^+/π^+ runs, so this point is not included in the analysis.

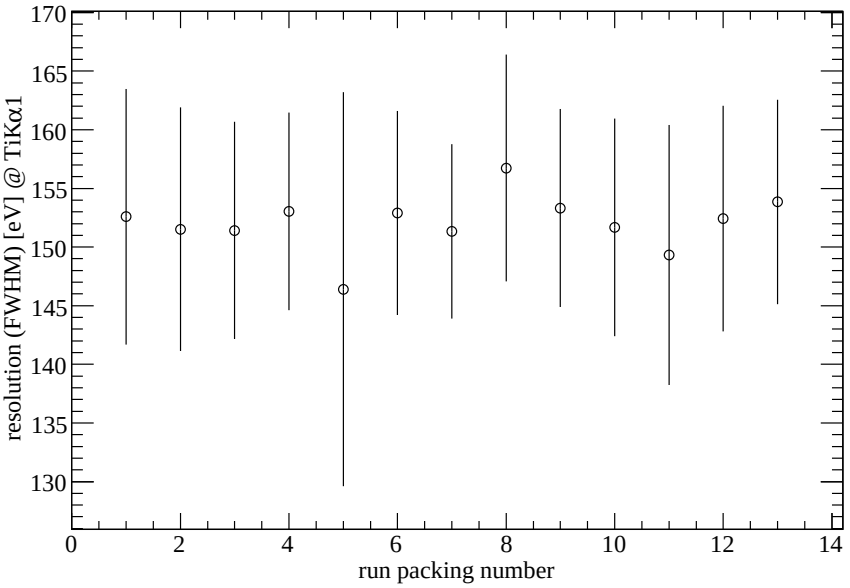

Figure 3.11: Energy resolution of SDD1-2nd as a function of the run-packing number. The poor-statistics point at 5 is not included in the analysis.

Figure 3.14. These statistical errors cause an ambiguity for the bin-increment of the histograms when we sum over all data, and the ambiguity depends on the bin width of the histograms. To estimate the systematic error associated with this procedure, we checked different-bin histograms (section 4.2.2).

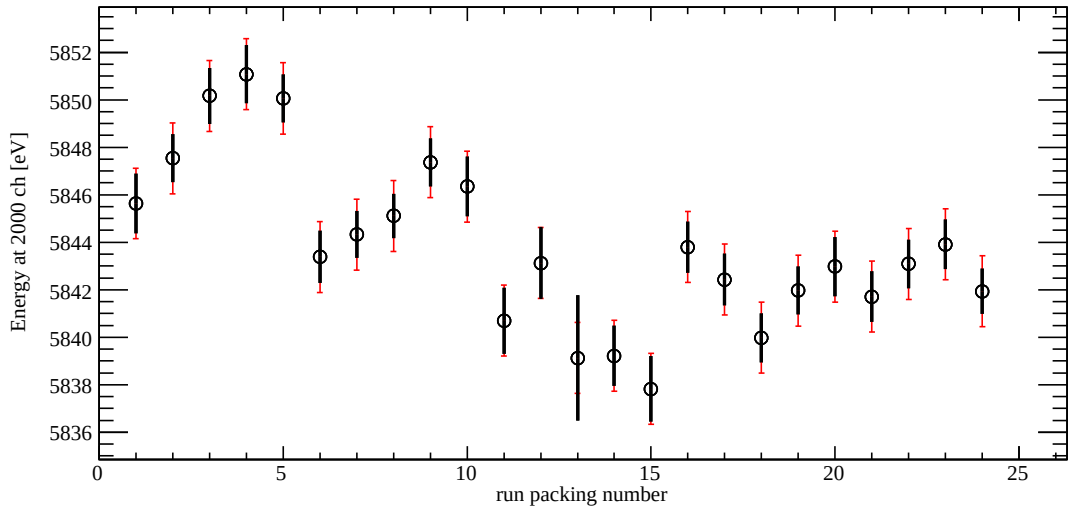

Figure 3.12: Converted energy of SDD2-1st as a function of the run packing-number. The black bar denotes the statistical error propagated from the uncertainty of calibration parameters. The red bar denotes the quantization error associated with the dynamic range of the ADC.

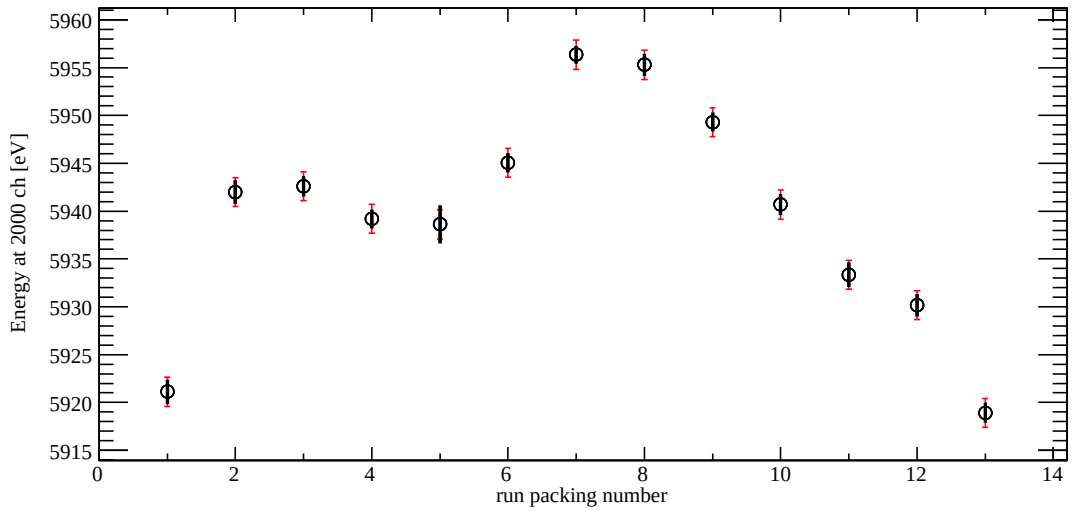

Figure 3.13: Converted energy of SDD1-2nd as a function of the run-packing number. The black bar denotes the statistical error propagated from the uncertainty of calibration parameters. The red bar denotes the quantization error associated with the dynamic range of the ADC.

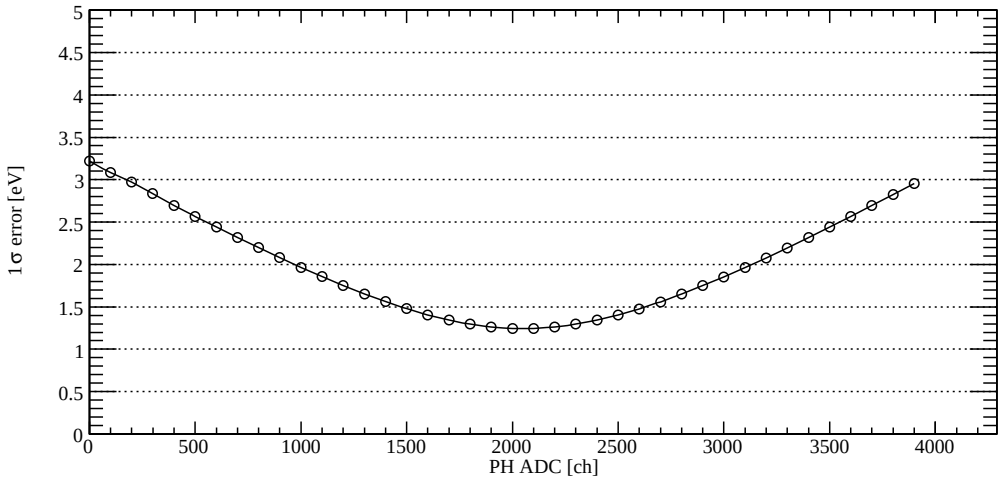

Figure 3.14: Typical distribution of statistical error attached on the energy conversion. Vertical axis is the 1 σ statistical error (eV). The error was propagated from the uncertainty of calibration parameters.

3.3.3 An Estimation of Systematic Error using Flash ADC Data

To estimate the systematic error associated with the energy calibration, flash ADC data were used. The waveform obtained by flash ADC data was useful to identify the pileup events. Since the pre-pileup events cause a high-energy-side tail and some excesses among high-statistics peaks, the elimination of them is important to realize the more accurate energy calibration. In this sub-section, the flash ADC data analysis is described.

Figure 3.15 shows waveforms of the typical pileup events, pre-pileup and post-pileup. The flash ADC covered about a 10 μs region in total, and we can search the pileup events just before or after the shaped signals.

A normal event was measured as shown in Figure 3.16. Non-hit SDD channels are also shown with red and green lines to see the base-line. When we relate the flash ADC data with the peak-hold ADC data, we must consider the maximum-peak position and the base-line at that point. However, the base-line was not so clear due to a long-time-period noise. With that we defined "base-line" of flash ADC as the average of the data point between 0 and 40, just before rising (see Figure 3.16).

A correlation contour between "base line" of the flash ADC and the PH ADC data is shown in Figure 3.17. Most calibration events were within the noise-level of the flash ADC. However some events had a positive correlation. This means the peak height was increased by the pre-pileup. We cut the correlation at the $+2.5\sigma$ (of single Gaussian) line of the noise-level, with the result shown in Figure 3.18 in red. These events corresponded to the excess between K_α and K_β.

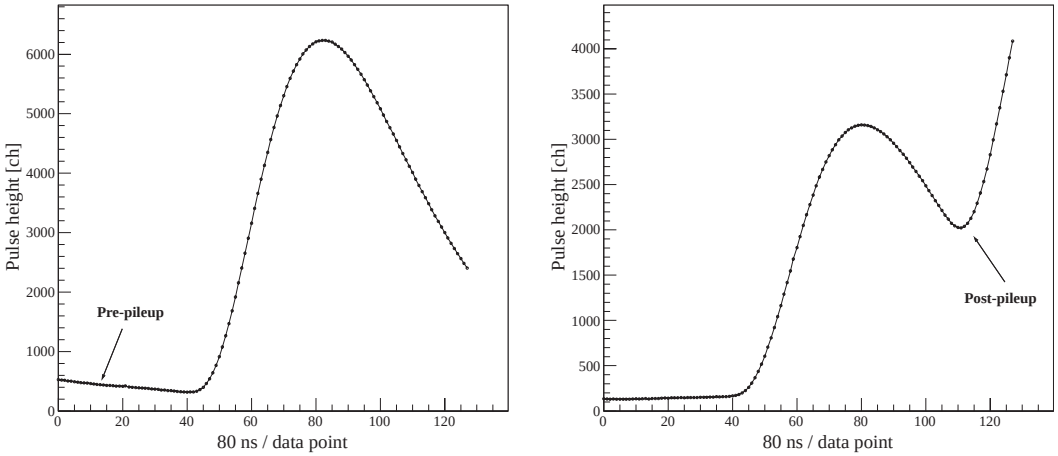

Figure 3.15: Typical pileup events measured by a flash ADC. Left is a pre-pileup event and right is a post-pileup one.

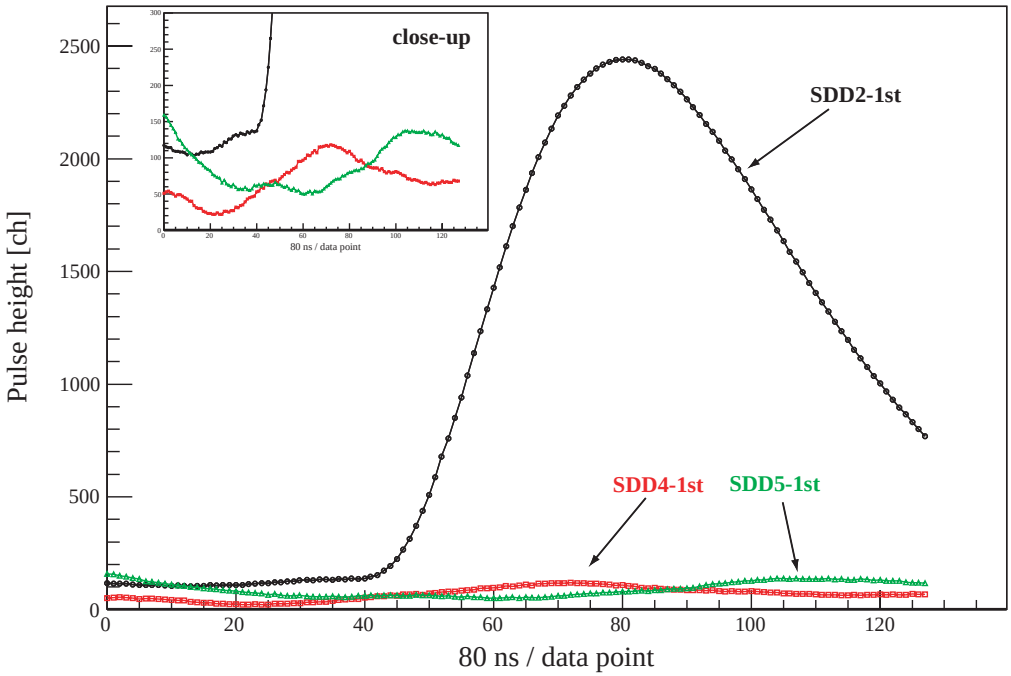

Figure 3.16: Waveform of a normal event. Non-hit SDD channels are also shown with colored lines. A "base-line" of a waveform was defined as the average of the data points between 0 and 40, just before rising.

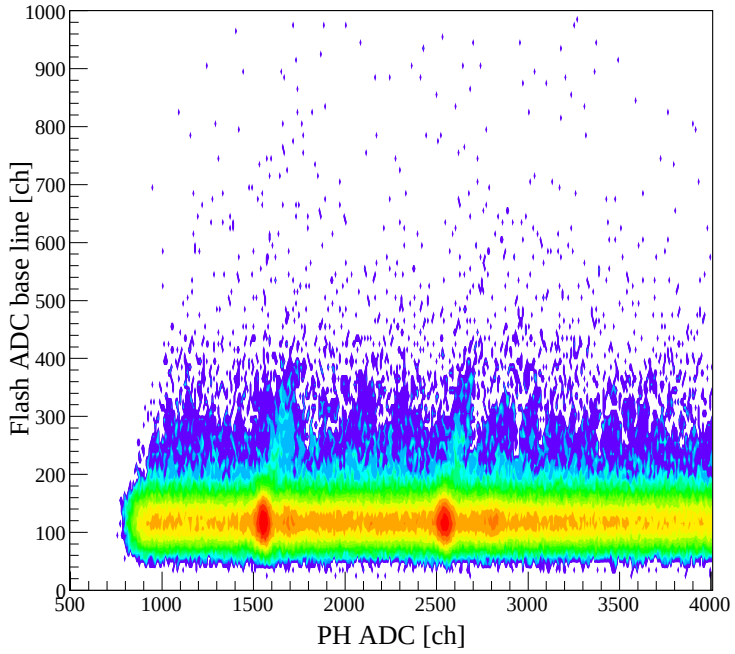

Figure 3.17: Correlation between "base-line" of the flash ADC and the PH ADC of SDD2-1st. Some events had a positive correlation with the "base-line". This means the peak height was increased by the pre-pileup.

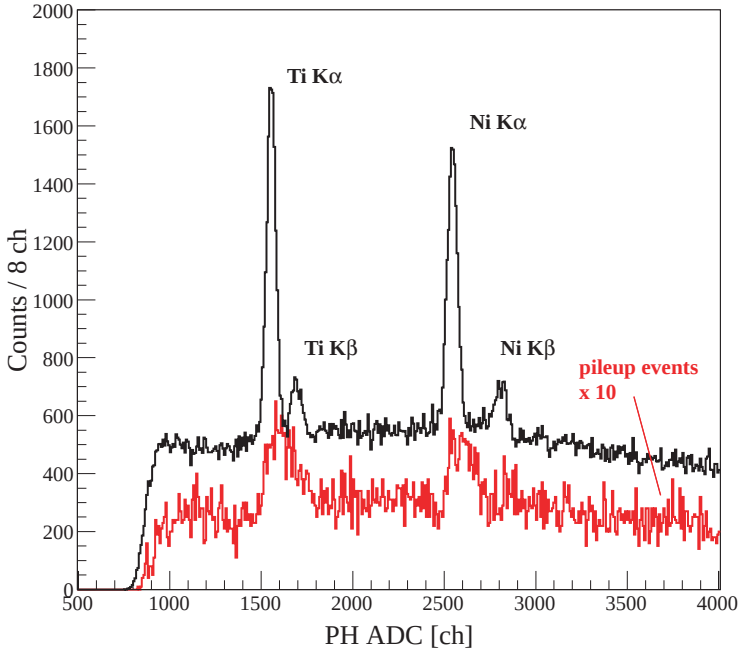

Figure 3.18: Pre-pileup events obtained by analysis of the flash ADC data. The red histogram was selected an over $+2.5\sigma$ of the noise-level of the flash ADC (base line $\geq$177 ch for SDD2-1st).

The excess influenced the determination of calibration parameters. For example, the K_β lines were pulled toward K_α lines in the fit, and the linearity was distorted. Figure 3.19 and Figure 3.20 shows the distorted linearity of energy calibration.

Now we are interested in the difference of energy calibration, when we use more significant events with a pre-pileup cut. The difference is shown in Figure 3.21. Though this is only a part of first-cycle data, the converted energy has a systematic shift $\sim +1$ eV. Since the analysis of flash ADC data has not been finished, we must consider this shift as a systematic error.

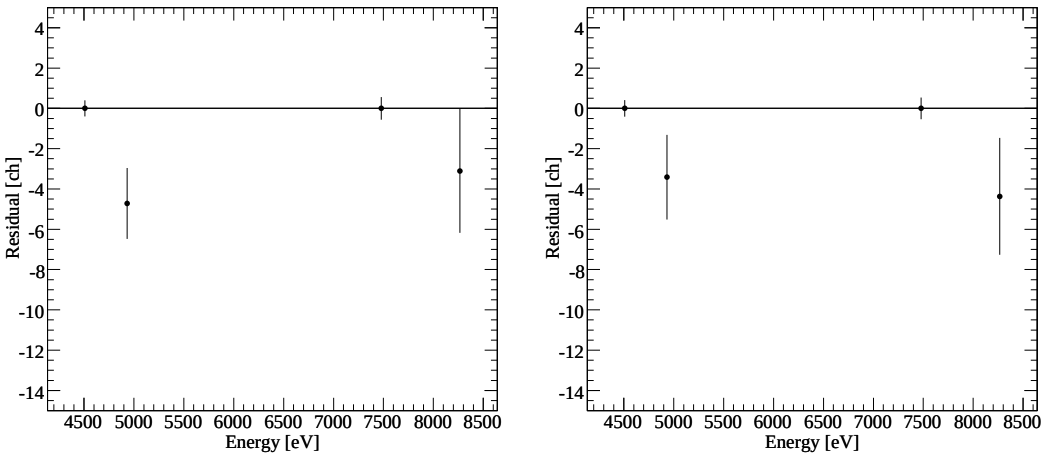

Figure 3.19: Linearity of energy calibration (first cycle). Vertical axis is the residual from the calibration line deduced from Ti $K_{\alpha 1}$ and Ni $K_{\alpha 1}$.

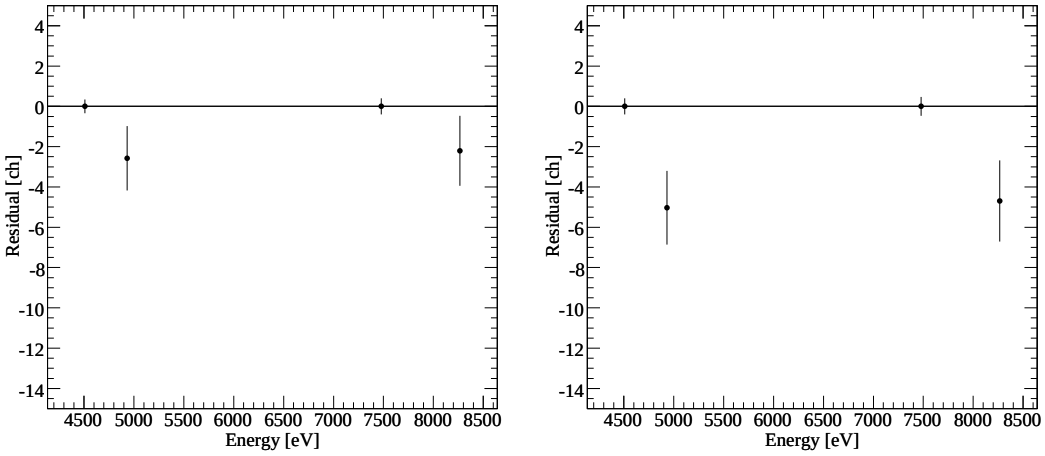

Figure 3.20: Linearity of energy calibration (second cycle). Vertical axis is the residual from the calibration line deduced from Ti $K_{\alpha 1}$ and Ni $K_{\alpha 1}$.

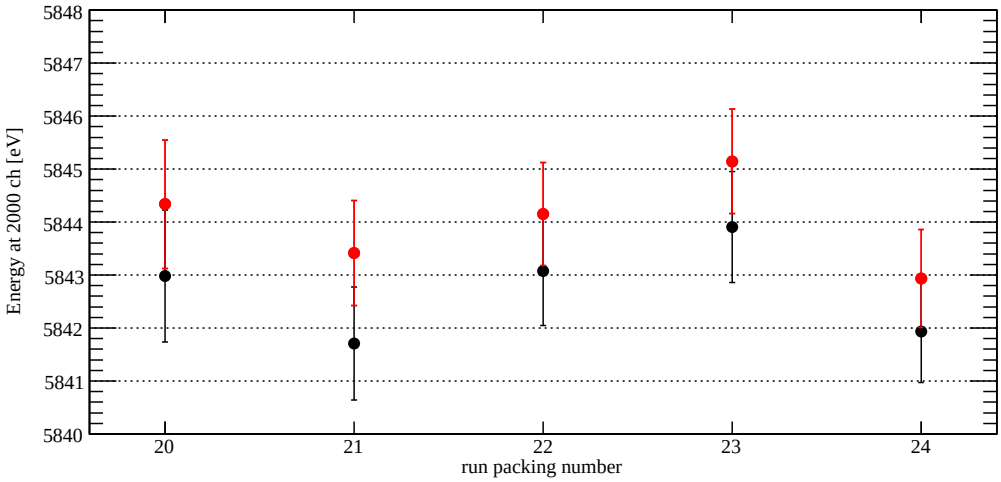

Figure 3.21: Difference of energy calibration using the events with pre pileup events cut. The red points denote the new calibration with pre-pileup cuts.

3.3.4 Timing Selection

Since ∼200 times the amount of pions was contaminated in the kaon beam, the timing resolution is important to reduce the accidental background due to pions. To improve the timing resolution, we corrected the time-walk of the individual SDDs. We used a following function for the slewing-correction between the ADC and the TDC.

$$\mathrm{TDC} = p1 + p2 \times \mathrm{ADC} + p3 \times \log\left(|\mathrm{ADC} - p4|\right) \tag{3.4}$$

where $p1$, $p2$, $p3$ and $p4$ are parameters determined by fitting the profile of the correlation.

In Figure 3.22, the typical correlation between the TDC and the ADC before slewing-correction is shown, and the slewing-corrected plot is shown in Figure 3.23.

The TDC spectra of E549-trigger data are shown in Figure 3.24 and Figure 3.25. The slewing-correction removed a tail structure and improved the timing resolution. We set the TDC-gate $\pm 2.5\sigma$ loosely as shown in Figure 3.25.

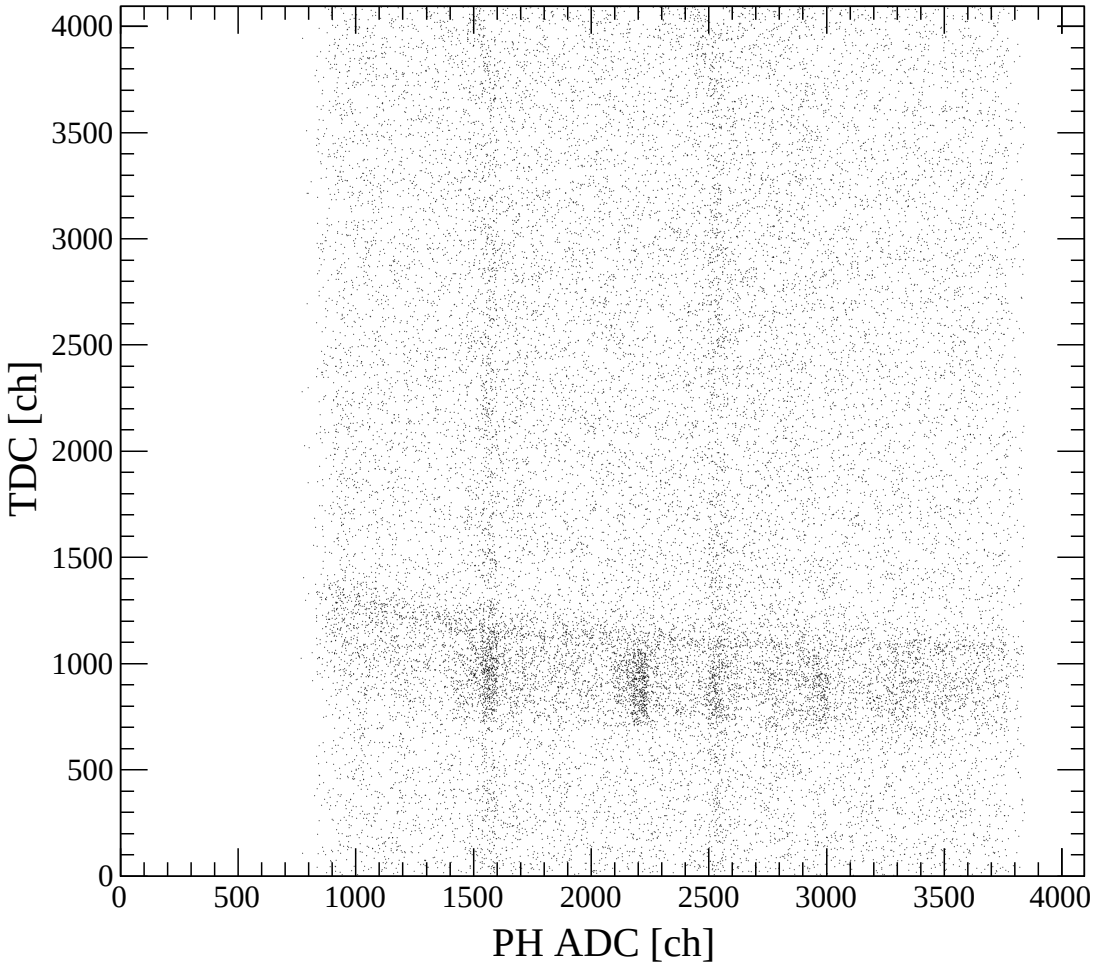

Figure 3.22: Typical correlation between the TDC and the ADC *before* slewing-correction (E549 trigger data).

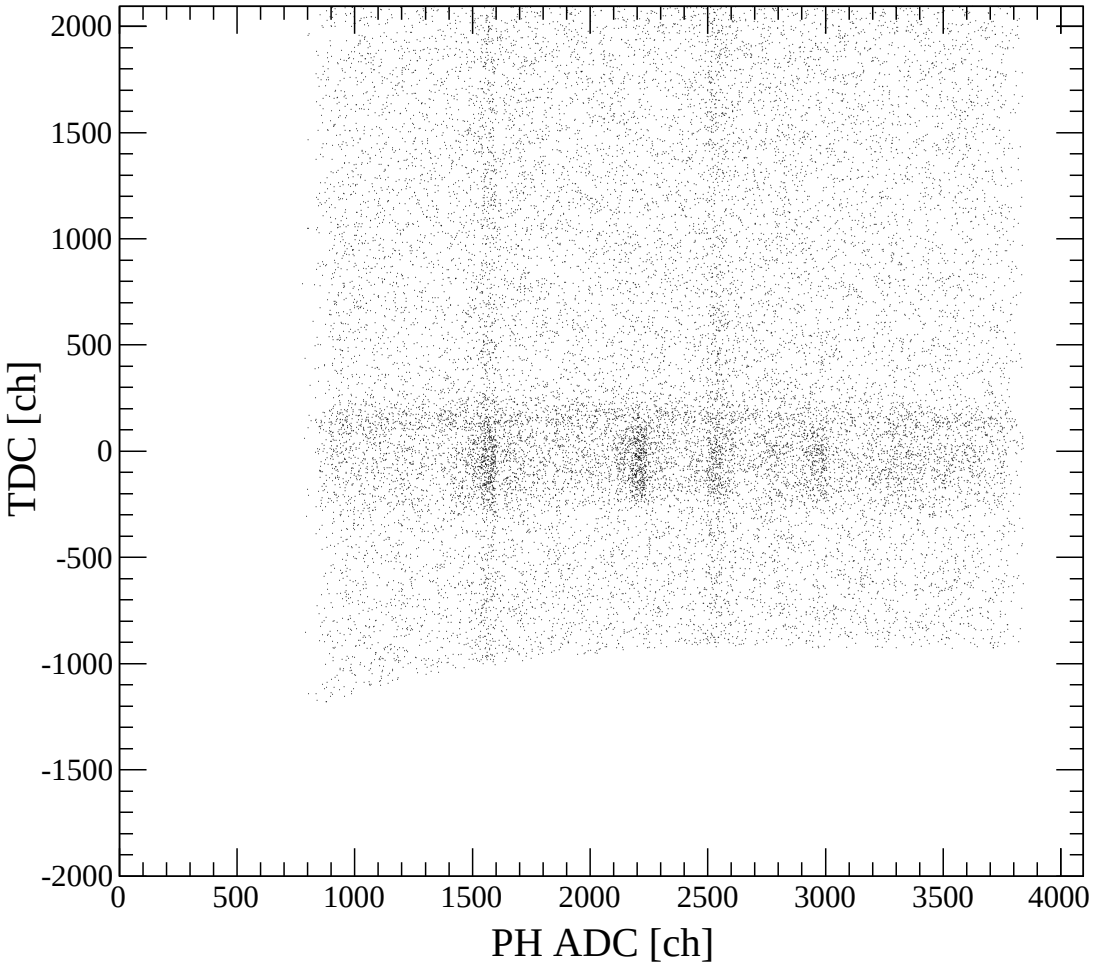

Figure 3.23: Typical correlation between TDC and ADC *after* slewing-correction (E549 trigger data).

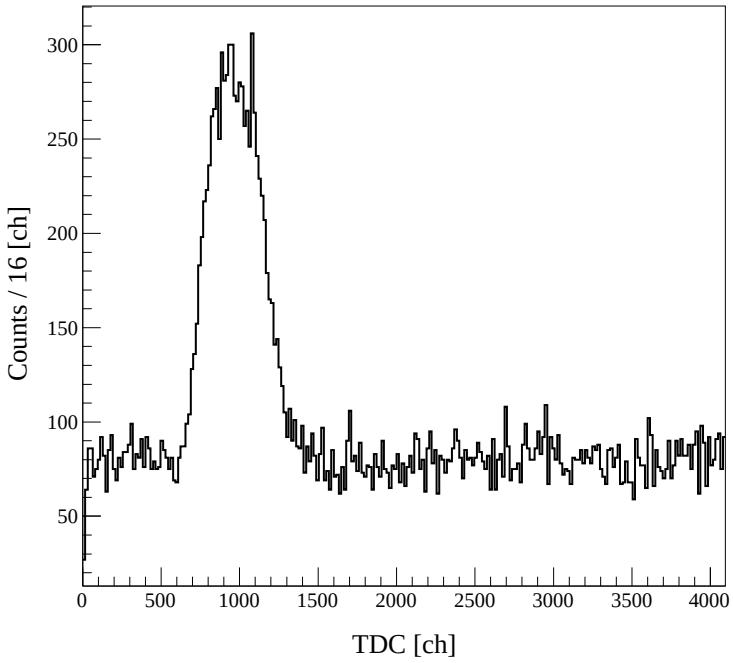

Figure 3.24: Typical TDC spectrum *before* slewing-correction.

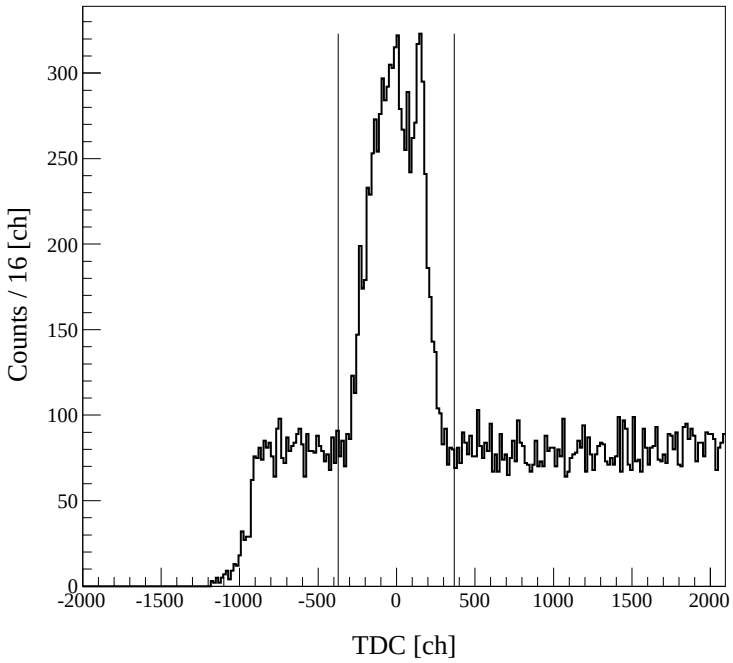

Figure 3.25: Typical TDC spectrum *after* slewing-correction. The solid lines denotes the time-gates of the TDC ($\pm 2.5\sigma$).

3.3.5 Summary of Detector Analysis

Here, let us summarize the detector analysis.

1. The fiducial-volume cuts were defined by

$$-70.0 \text{ mm} \leq z \leq +90.0 \text{ mm, and } r \leq 110.0 \text{ mm}$$

2. The energy calibration was performed with checks on the in-beam stability of energy resolution and time-dependent gain drifts.

3. Timing resolution for the kaon beam was improved by the slewing-correction of the individual SDDs using E549-trigger data. The time-gate was set loosely to $\pm 2.5\sigma$.

The energy resolution and timing resolution of SDDs are listed in Table 3.2.

Table 3.2: Summary of energy resolution at 6.4 keV and timing resolution for kaon-beam timing, SDD-by-SDD.

Detector	ΔE (FWHM) [eV]	Δt (FWHM) [ns]
SDD2-1st	188 ± 2	436 ± 7
SDD4-1st	187 ± 2	481 ± 9
SDD5-1st	226 ± 3	398 ± 8
SDD1-2nd	169 ± 3	479 ± 11
SDD2-2nd	194 ± 4	365 ± 7
SDD3-2nd	193 ± 3	456 ± 10
SDD4-2nd	171 ± 3	428 ± 10
SDD5-2nd	200 ± 4	366 ± 8
SDD7-2nd	214 ± 5	440 ± 13
SDD8-2nd	185 ± 3	454 ± 10
Total-1st	200 ± 1	-
Total-2nd	188 ± 1	-

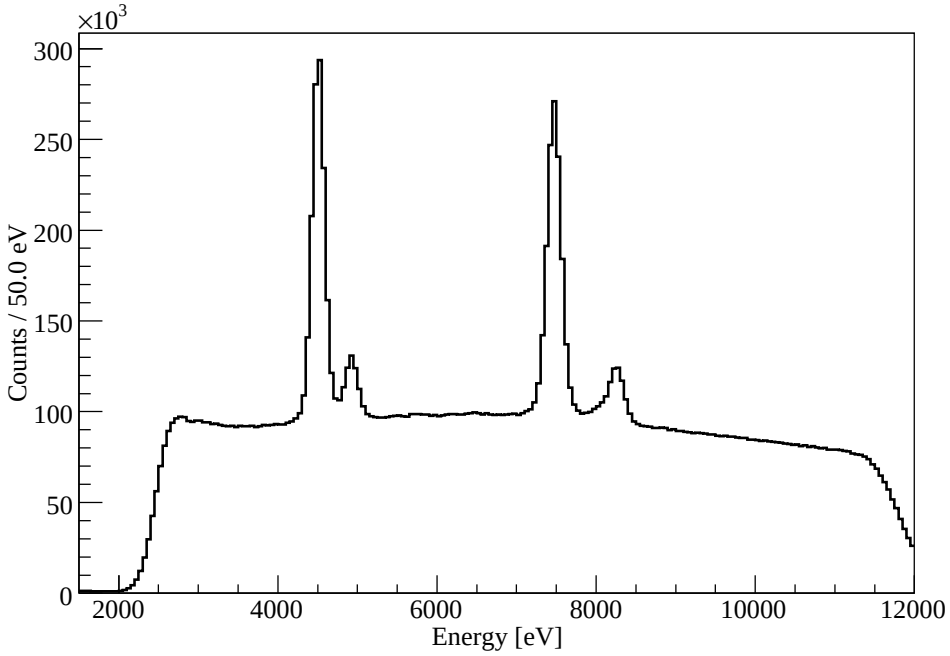

Figure 3.26: Energy spectrum summed over all the SDDs (first-cycle self-trigger data).

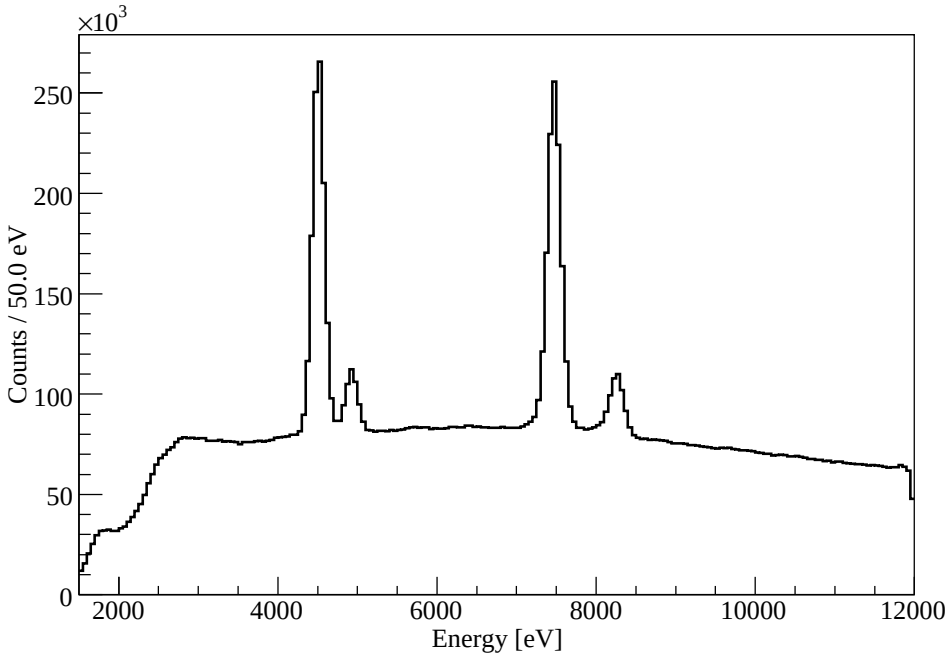

Figure 3.27: Energy spectrum summed over all the SDDs (second-cycle self-trigger data).

Chapter 4

Analysis II : Interpretation of Obtained Spectra

4.1 Obtained Kaonic Helium X-ray Spectra

By applying the fiducial-volume cuts and the kaon-timing cuts, we obtained the kaonic-helium X-ray spectra shown in Figure 4.1 and Figure 4.2. The top figure is the data of the first-cycle of E570, and the bottom one is the that of the second-cycle. All SDDs were calibrated individually using calibration spectra described in the previous chapter.

The kaonic-helium $3d \rightarrow 2p$ L_α X-ray is clearly observed at around 6.4 keV, and the $4d \rightarrow 2p$ L_β and $5d \rightarrow 2p$ L_γ X-rays are also observed. We can also see the titanium and nickel peaks (K_α and K_β) as self-trigger events due to the accidental coincidence with the kaon-timing and the contamination pion-timing.

4.2 Fits to the Measured Spectra

To get the position and the width of L_α peak, we fit the spectra by an appropriate function. In this section, the fitting procedure is described.

In fitting a function, we used the method of maximum likelihood. Assuming that the number of counts in the data obeys Poisson statistics, the negative-logarithm of the likelihood function is

$$\sum_i [(f_i - N_i) - N_i(\log f_i - \log N_i)] \tag{4.1}$$

where N_i and f_i are the observed number of counts in the i-th bin and most probable function predicted in fitting, respectively. To minimize this value, we used the calculation code MINUIT [23].

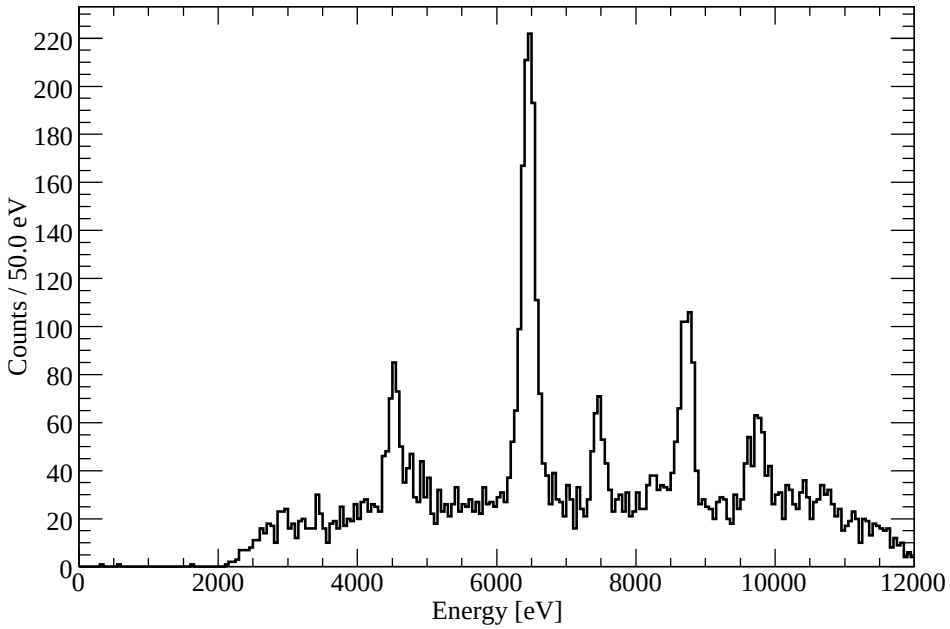

Figure 4.1: X-ray spectrum obtained after applying all cuts (first cycle data).

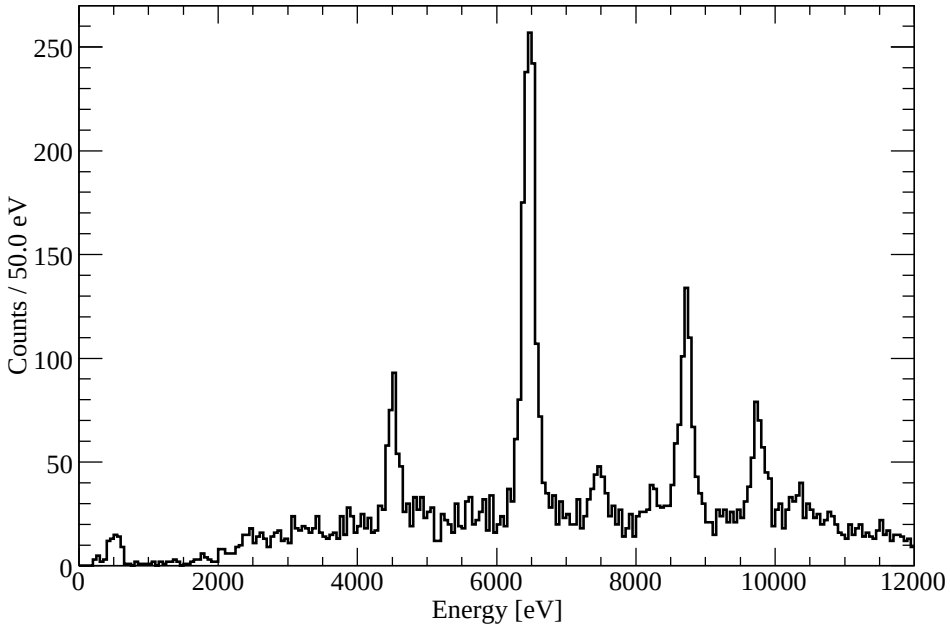

Figure 4.2: X-ray spectrum obtained after applying all cuts (second cycle data).

4.2.1 Fitting Function

The kaonic-helium X-ray has a natural-line width due to the strong interaction, so its shape is expected to be Lorentzian. If the detector-response function is approximated by a Gaussian, the kaonic-helium X-ray line is represented by a convoluted function of a Gaussian and a Lorentzian. This function is called a Voigt function. The function we used here has three parameters Voigt(E, σ, Γ), where E is the center, σ is the Gaussian sigma, and Γ is the Lorentzian width.

We introduced four Voigt functions to fit L_α, L_β, L_γ and L_δ X-rays. The sigma of the Gaussian was fixed by the calibration spectrum, and its energy dependence was given by equation (3.3).

The intensity ratios of the individual X-rays are unknown. While several atomic-cascade calculations have been done [24], the definite answer has not yet been provided. Due to the ambiguity of the absorption, especially from the collision process with surrounding helium atoms, the s- and p-orbits absorption ratio has not been determined. Therefore, no restriction was placed in the intensity parameters.

The strong-interaction shift and width of the L_β, L_γ and L_δ were assumed to be the same as L_α, because the calculated ratio of d-orbits absorption is small (0.4 %) [24, 25]. This means the shifts on the $4d$-, $5d$- and $6d$-orbits were negligible.

Similar to the calibration spectra, the background was assumed to be a smooth function and was fitted by a quadratic function. For the calibration peaks, six Gaussians were used with fixed width and calibration spectra energies of known values [21].

A summary of the fit parameters is listed in Table 4.1.

Table 4.1: Summary of fit parameters.

Number	Parameter name	Description	State
1	a	background (constant)	free
2	b	background (bx)	free
3	c	background (cx^2)	free
4	H_{Ti}	Ti $K_{\alpha 1}$ height	free
5	H_{Ni}	Ni $K_{\alpha 1}$ height	free
6	$R_{\mathrm{K}\beta/\mathrm{K}\alpha 1}$ (Ti)	K_β / $K_{\alpha 1}$ ratio of Ti	free
7	$R_{\mathrm{K}\beta/\mathrm{K}\alpha 1}$ (Ni)	K_β / $K_{\alpha 1}$ ratio of Ni	free
8	$H_{\mathrm{KHeXL}_\alpha}$	kaonic-helium L_α height	free
9	$R_{L\beta/L\alpha 1}$	L_β / L_α ratio	free
10	$R_{L_\gamma/L_\alpha 1}$	L_γ / L_α ratio	free
11	$R_{L_\delta/L_\alpha 1}$	L_δ / L_α ratio	free
12	ΔE_{2p}	strong-interaction shift	free
13	Γ_{2p}	strong-interaction width	free
14	N	constant noise	fixed
15	F	Fano factor	fixed
16	$E_{\mathrm{TiK}\alpha 1}$	4510.84 eV	fixed
17	$E_{\mathrm{TiK}\beta}$	4931.81 eV	fixed
18	$E_{\mathrm{NiK}\alpha 1}$	7478.15 eV	fixed
19	$E_{\mathrm{NiK}\beta}$	8264.66 eV	fixed

4.2.2 Fits and Results

Fitted X-ray spectra are shown in Figure 4.3 and Figure 4.4.

As mentioned in section 3.3.1, the energy calibration had an ambiguity in converting the ADC channel into the energy. The ambiguity came from the statistical error of the calibration parameters and the quantization error of the peak-hold ADC. Here, it was estimated by fitting different-bin histograms. In principle, the results have no dependence on the bin-width. A systematic difference, if it exists, indicates that the statistics of the energy calibration is not sufficient. We checked the binning effect at several bin-widths, and we defined the final statistical error and the systematic error associated with this procedure. That is,

$$\Delta E_{2p} = \frac{1}{N} \sum_{i=\{10,20,\ldots,80\}} \Delta E_{2p}^{(i)}, \tag{4.2}$$

$$\sigma_{stat}(\Delta E_{2p}) = \frac{1}{N} \sum_{i=\{10,20,\ldots,80\}} \sigma_{stat}(\Delta E_{2p}^{(i)}), \tag{4.3}$$

$$\sigma_{sys}(\Delta E_{2p}) = \sqrt{\frac{1}{N-1} \sum_{i=\{10,20,\ldots,80\}} (\Delta E_{2p}^{(i)} - \Delta E_{2p})^2} \tag{4.4}$$

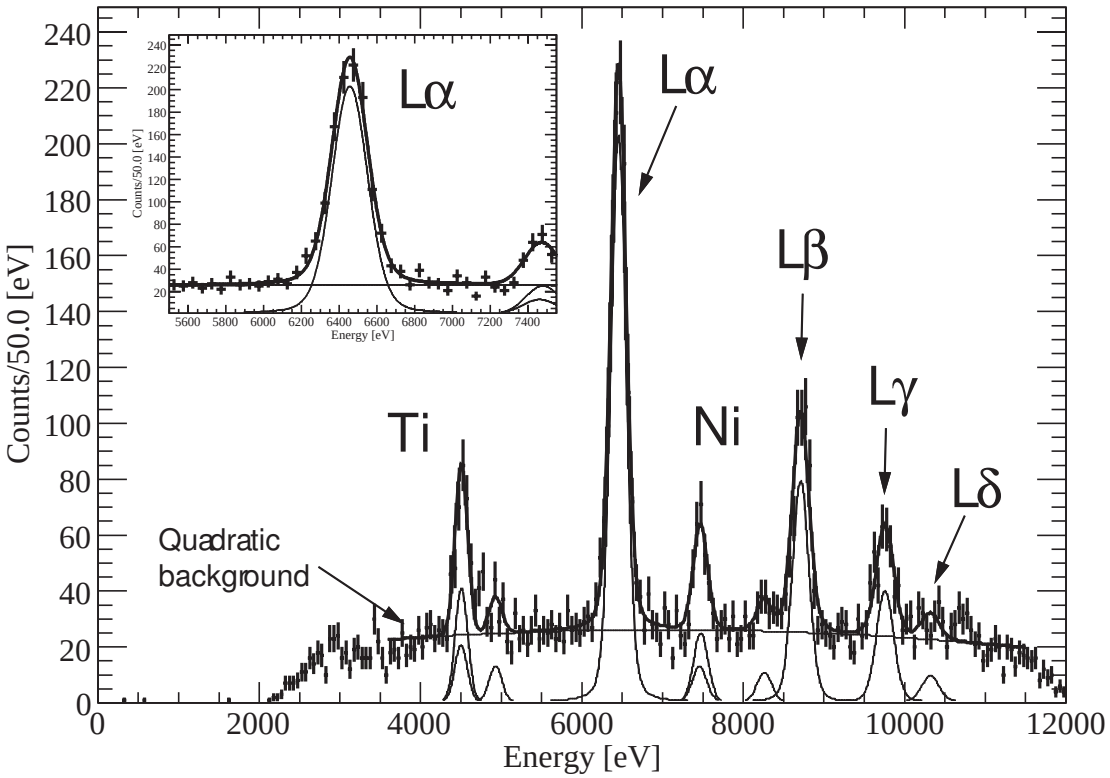

Figure 4.3: Fitted X-ray spectrum (first-cycle data). The inset shows an enlarged view of the L_α region.

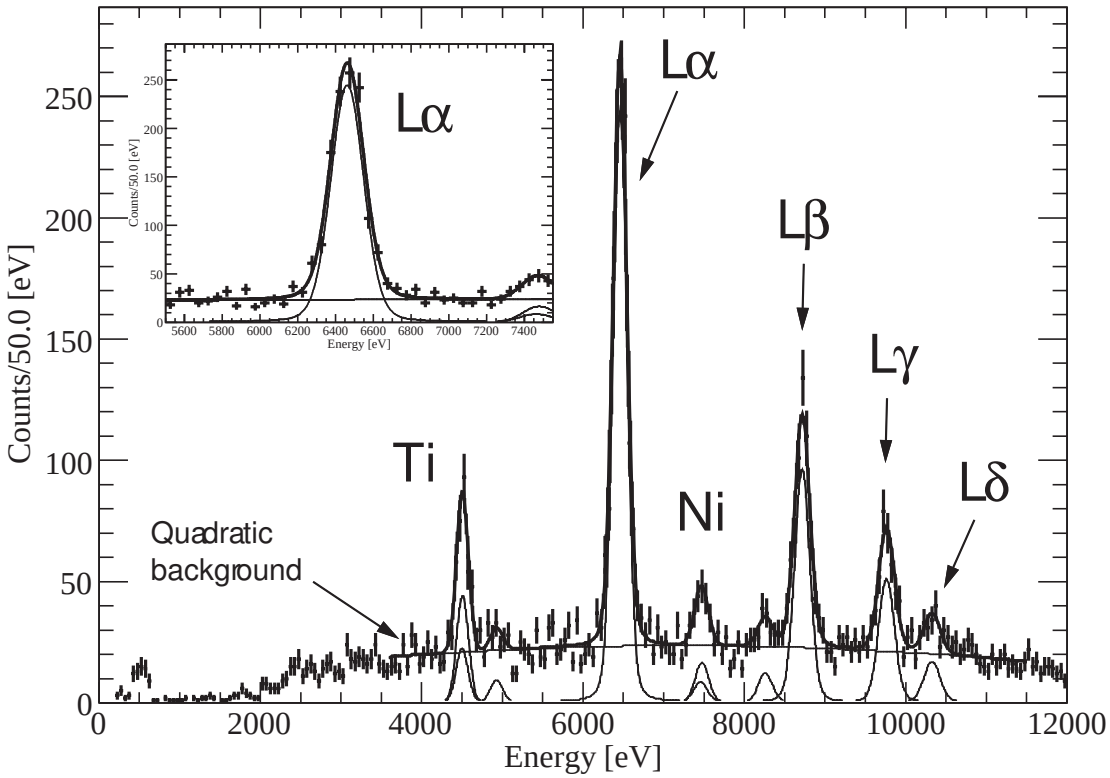

Figure 4.4: Fitted X-ray spectrum (second-cycle data). The inset shows an enlarged view of the L_α region.

where i denotes the bin-width of histograms and N is the number of histograms, here $N = 8$. Similar expressions are used for the natural-line width. Here it should be emphasized that this systematic error is statistical in nature.

The fitting results are shown in Figure 4.5 and the results obtained are listed in Table 4.2. Assuming the pure-electromagnetic energy is 6463 eV [16], the strong-interaction shift was $-6.6 \pm 3.5 \pm 0.4$ eV and $-1.1 \pm 2.9 \pm 0.5$ eV for the first and second cycle of E570, respectively. Where the first error is statistical and the second one is systematics associated with this procedure. The negative sign denotes the *repulsive* shift of the strong interaction. For the width, we obtained $42 \pm 10 \pm 2$ eV and $28 \pm 8 \pm 1$ eV for the first and second cycle of E570, respectively.

The individual-detectors analysis will be described in appendix D.

Table 4.2: Fit results of different bin histograms. The ΔE_{2p} is defined the energy difference from the pure electromagnetic calculation 6463 eV [16].

	1st cycle	2nd cycle
ΔE_{2p} (eV)	$-6.6 \pm 3.5 \pm 0.4$	$-1.1 \pm 2.9 \pm 0.5$
Γ_{2p} (eV)	$42 \pm 10 \pm 2$	$28 \pm 8 \pm 1$

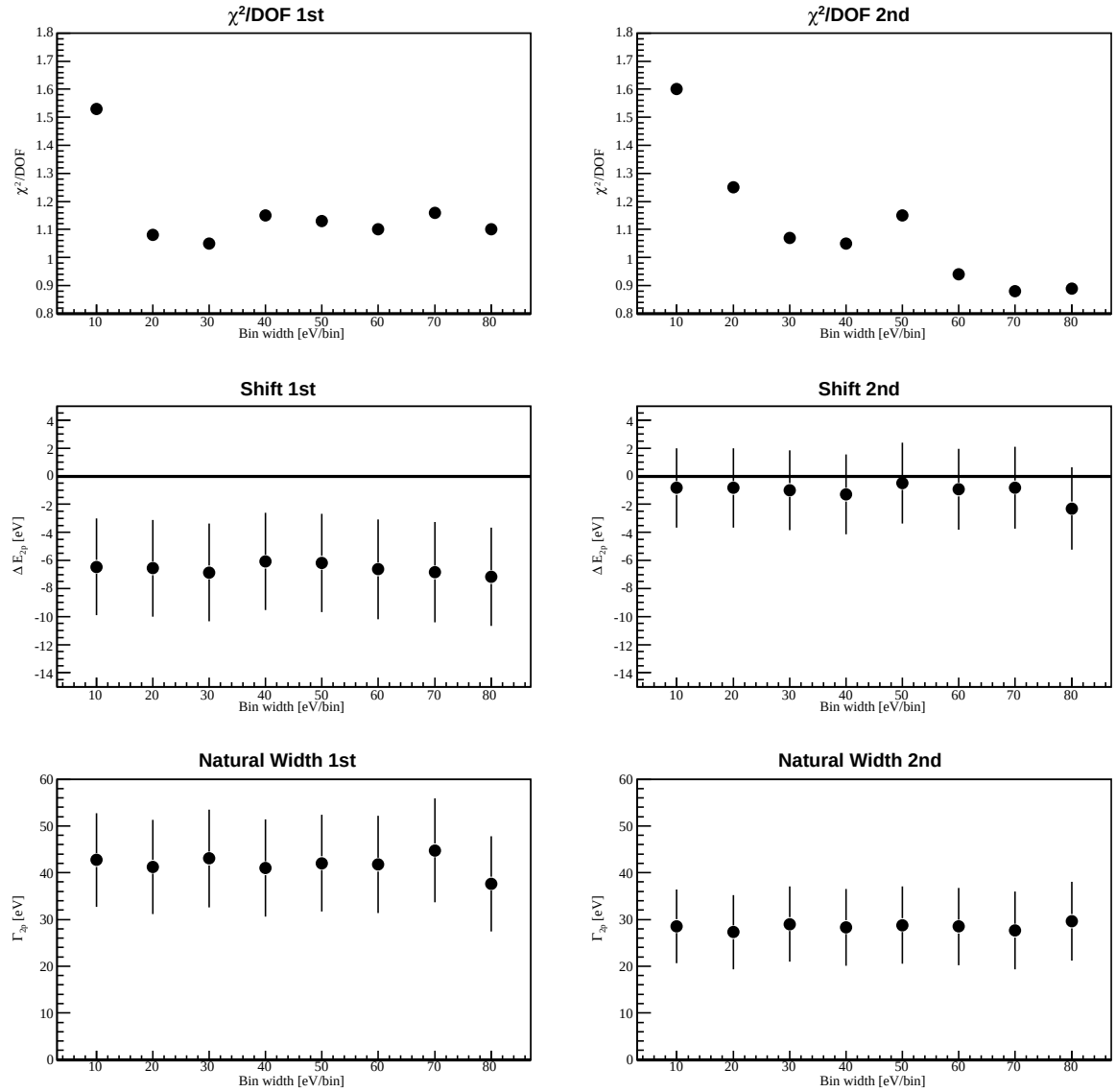

Figure 4.5: Fit results of different bin histograms for estimation of the systematic error associated with the ambiguity of the calibration parameters. Tops are reduced χ^2, centers are the $2p$-orbit energy shift and the bottoms are the natural width. There is not so much difference between different bin histograms.

4.3 Systematic Errors

There are three types of systematic errors for ΔE_{2p} and Γ_{2p}, associated with the background estimation of the spectra obtained, the energy calibration and the energy loss of X-rays due to Compton scattering in the target. In this section, these systematic errors are evaluated. The results are listed in Table 4.3.

4.3.1 Background

The systematic error associated with the background was evaluated by changing the function from a quadratic function to a constant line.

4.3.2 Energy Calibration

The energy resolution calculated from electronic noise and the Fano factor was fixed in fitting by the calibration spectrum. The systematic error associated with these fixed parameters was evaluated by varying them by the one standard deviation. Note that this error is statistical in nature.

As seen in section 3.3.3, the converted energy of the channel 2000 was shifted by +1 eV systematically due to the pileup events. Since the analysis of flash ADC data has not yet been finished, we can not provide a definite number for the systematic error, especially for the second cycle.

4.3.3 Compton Scattering in the Target

The most significant systematic error is the energy loss of X-rays due to Compton scattering in the target materials. Scattered X-rays give rise to tail structure $\sim$100 eV lower than the original peak. The tail structure influences the estimation of ΔE_{2p} and Γ_{2p}.

The size of the tail structure was estimated at $\sim$12 % by a GEANT simulation using the Low Energy Compton Scattering (LECS) package [26]. Figure 4.6 shows a simulation result of the Compton and Rayleigh scattering in liquid helium-4. The threshold of binding energy of the atom is clearly reproduced, and the energy distribution of the Compton scattered photons is agree a the theoretical one [27].

When we fitted the simulated histogram by single Gaussian response-function, the center shifted by -10 eV. The shift as a function of the percentage of Compton scattering (corresponding to the ambiguity of the cross section) at 6.4 keV is shown in Figure 4.7.

Due to the energy dependence of Compton scattering and the convolution with a Lorentzian, the correction of this effect is not simple and is not yet finished. Note that the shift of the center ΔE_{2p} due to this effect is expected on one side only, the direction is *attractive* shift.

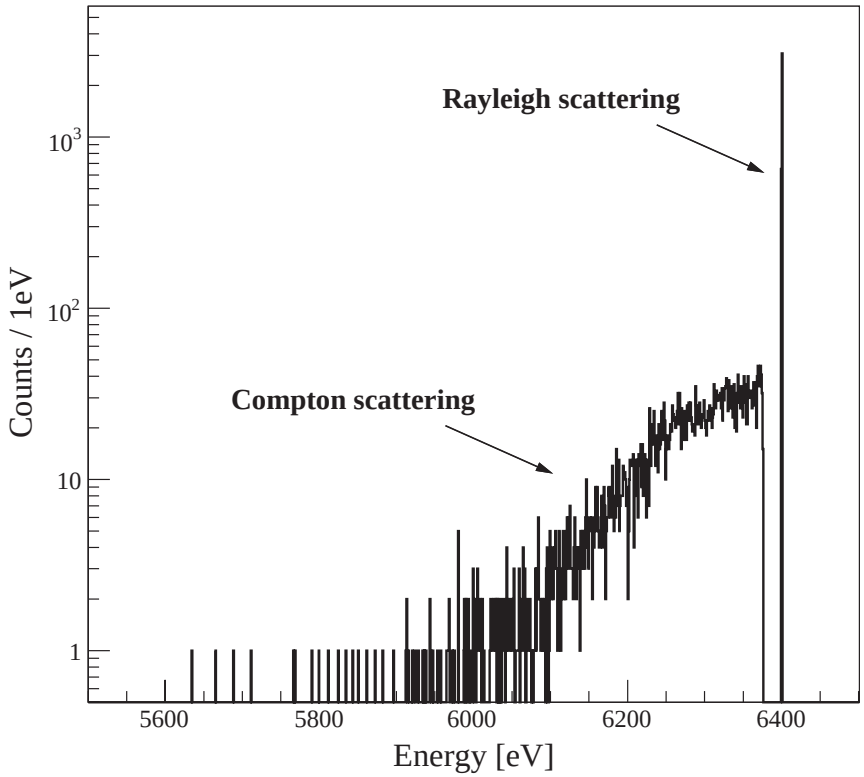

Figure 4.6: A simulated result of Compton scattering in the liquid ^{4}He target by GEANT 4.8.2 using the LECS package [26]. The threshold of binding energy of helium-4 atom is clearly reproduced, and the energy distribution of the Compton scattered photons is agree with a theoretical one [27].

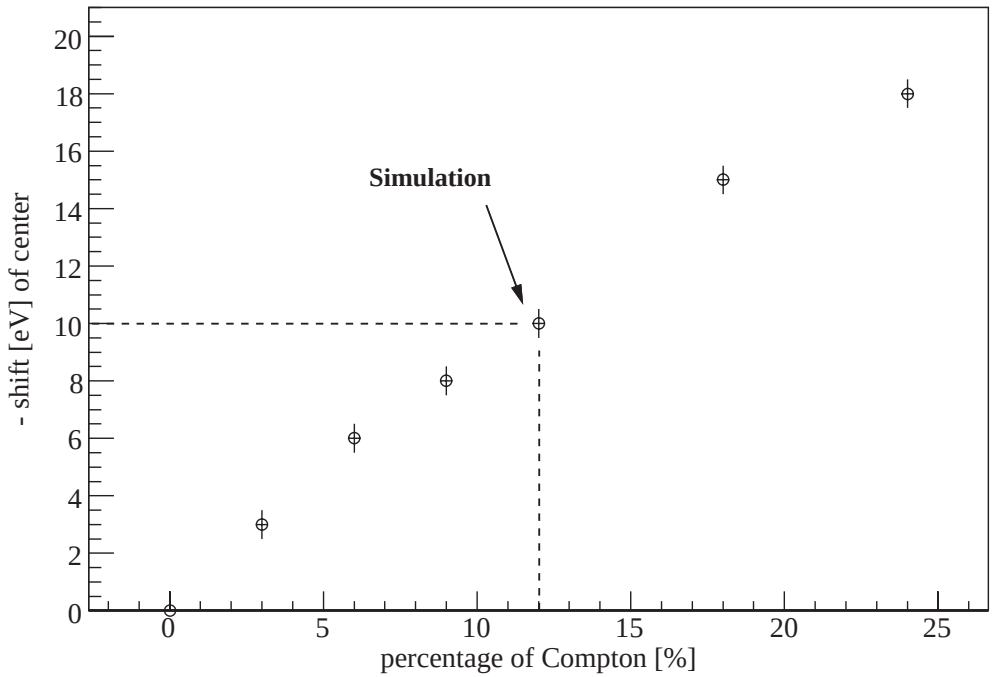

Figure 4.7: Simulated systematic shift of the centroid of the peak due to Compton scattering. The dashed line shows this simulation. Other points are given by scaling the amount of Compton scattering, which corresponds to changing the cross section.

The Compton tail influences the estimation of the natural-line width Γ_{2p} also. The systematic error of Γ_{2p} was evaluated at $\sim$ 14 eV by the simulation conservatively without Compton scattering correction.

Note that, finally, the systematic errors from the pileup problem and the Compton tail can be corrected in principle and will be corrected in the near future. After the correction, the systematic error will be re-evaluated as an uncertainty of the correction.

Table 4.3: Systematic errors. Note that the errors from Compton scattering will be corrected.

	δ (eV)	1st cycle	2nd cycle
Background estimation	δE_{2p}	$^{+0.0}_{-0.3}$	$^{+0.0}_{-0.1}$
	$\delta\Gamma_{2p}$	$^{+12}_{-0}$	$^{+11}_{-0}$
Energy resolution	δE_{2p}	$^{+0.0}_{-0.1}$	$^{+0.0}_{-0.0}$
	$\delta\Gamma_{2p}$	$^{+4}_{-4}$	$^{+2}_{-3}$
Pileup problem	δE_{2p}	+1.0	+1.0
	$\delta\Gamma_{2p}$	-	-
Compton scattering	δE_{2p}	(+10)	(+10)
	$\delta\Gamma_{2p}$	(−14)	(−14)

4.4 Estimation of Relative X-ray Yields

The estimation of the number of stopped K^- on helium-4 is complicated due to the existence of the meta-stable state [28] and the tracking efficiency for fiducial-volume cuts. This detail will be described in appendix B. Here, let us estimate the relative X-ray yields.

The observed number of X-rays is listed in Table 4.4. It was calculated by integrating the Voigt function. The error was estimated by changing the height of the Voigt function by $\pm 1\sigma$ (the integral depends on the height mainly). The average acceptance for the X-rays was calculated by a Monte Carlo simulation using the measured K^- stopping distribution with the GEANT4.8.2 LECS package. In the simulation, X-ray attenuation and Compton scattering with bound electrons were considered.

Table 4.4: Observed number of X-rays and averaged acceptance.

X-rays		L_α	L_β	L_γ	L_δ
Observed number	(1st cycle)	1041±46	439±31	228±24	54±18
	(2nd cycle)	1126±45	482±31	264±24	88±18
Acceptance (%)		0.083	0.099	0.102	0.100

Assuming the other efficiencies (tracking, DAQ accept, dead time of SDDs, etc) were the same when the X-rays were measured, the relative yields with acceptance correction can be calculated. The results are listed in Table 4.5 with references [4,5].

Table 4.5: Relative X-ray yields with acceptance correction.

X-rays		L_α	L_β	L_γ	L_δ
Relative yields	(1st cycle)	100±6	35±3	18±2	4±1
	(2nd cycle)	100±6	36±3	19±2	6±1
	Average	100±4	36±2	19±1	5±1
	[4]	100±4	37±5	20±4	-
	[5]	100±6	26±4	18±3	4±3

Chapter 5

Results and Discussion

We obtained for the strong interaction shift and width of the kaonic helium-4 atom $2p$ state,

$$\text{1st cycle:} \quad \Delta E_{2p} = -6.6 \pm 3.5(\text{stat.}) \text{ eV}$$

$$\text{1st cycle:} \quad \Gamma_{2p} = 42 \pm 10(\text{stat.}) \text{ eV}$$

$$\text{2nd cycle:} \quad \Delta E_{2p} = -1.1 \pm 2.9(\text{stat.}) \text{ eV}$$

$$\text{2nd cycle:} \quad \Gamma_{2p} = 28 \pm 8(\text{stat.}) \text{ eV}$$

respectively. The average of these individual results is

$$\Delta E_{2p} = -3.3 \pm 2.2(\text{stat.}) \text{ eV}$$

$$\Gamma_{2p} = 33 \pm 6(\text{stat.}) \text{ eV}$$

where **only the statistical error was considered**. The systematic error is not definite, since the correction of Compton scattering is not finished yet. Its estimation is work in progress.

A comparison with the previous experiments is shown in Figure 5.1 and Figure 5.2. We can expect that the present result of ΔE_{2p} is outside the previous world average with greater than 99% confidence, **even if we consider the most conservative systematic error without Compton scattering correction** for our result.

When we compare these results with theoretical calculations, our results agree, especially for ΔE_{2p}. Γ_{2p} is expected to have a large systematic error in contrast to the shift. This is because it is difficult to justify the existence of a deeply-bound kaon-nucleus state. The most important fact is that our results are consistent with the theoretical predictions discussed over the years. We can conclude that *the long-standing kaonic helium puzzle is resolved.*

The next step for further understanding of the strong interaction between the kaon and the helium nucleus would be a measurement of kaonic helium-3 atom X-rays, which have not been measured yet. According to Akaishi's prediction, kaonic helium-3 atom X-rays also have a large strong-interaction shift and width, if the deeply-bound kaon-nucleus states do exist. The measurement will give us not only a cross check of the present results but also new and conclusive aspects of the deeply-bound states. An experiment to measure them has been planed at J-PARC [(i)] K1.8 branch beam-line.

For the low energy $\bar{K}N$ interaction, a high precision spectroscopy experiment using about two hundreds SDDs has been planed at DAΦNE at LNF [(ii)]. The experiment aims to measure kaonic hydrogen X-rays with a few eV accuracy and also kaonic deuterium. The measurements will provide the most accurate information on the kaon-proton and kaon-deuteron scattering lengths. They will shed light on the isospin dependence of the $\bar{K}N$ interaction at threshold.

[(i)] Japan Proton Accelerator Research Complex (J-PARC) in Tokai.
[(ii)] Frascati National Laboratory, Italy

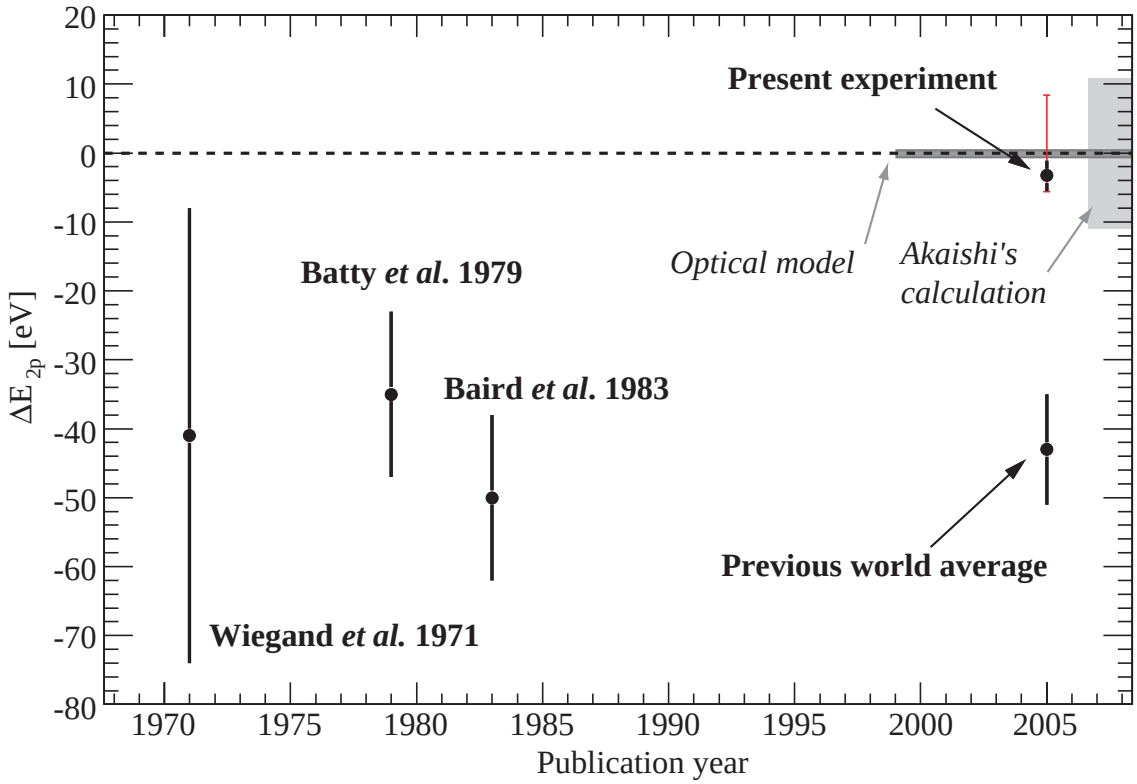

Figure 5.1: $2p$ state energy shift obtained in the present experiment. The black error bar denotes only the statistical error, and the red error bar denotes **the most conservative error without Compton scattering correction** (its estimation is work in progress). In comparison, the previous measurements and their average are also plotted [3–5]. The conventional optical-potential model and Akaishi's calculations are also shown [6, 17].

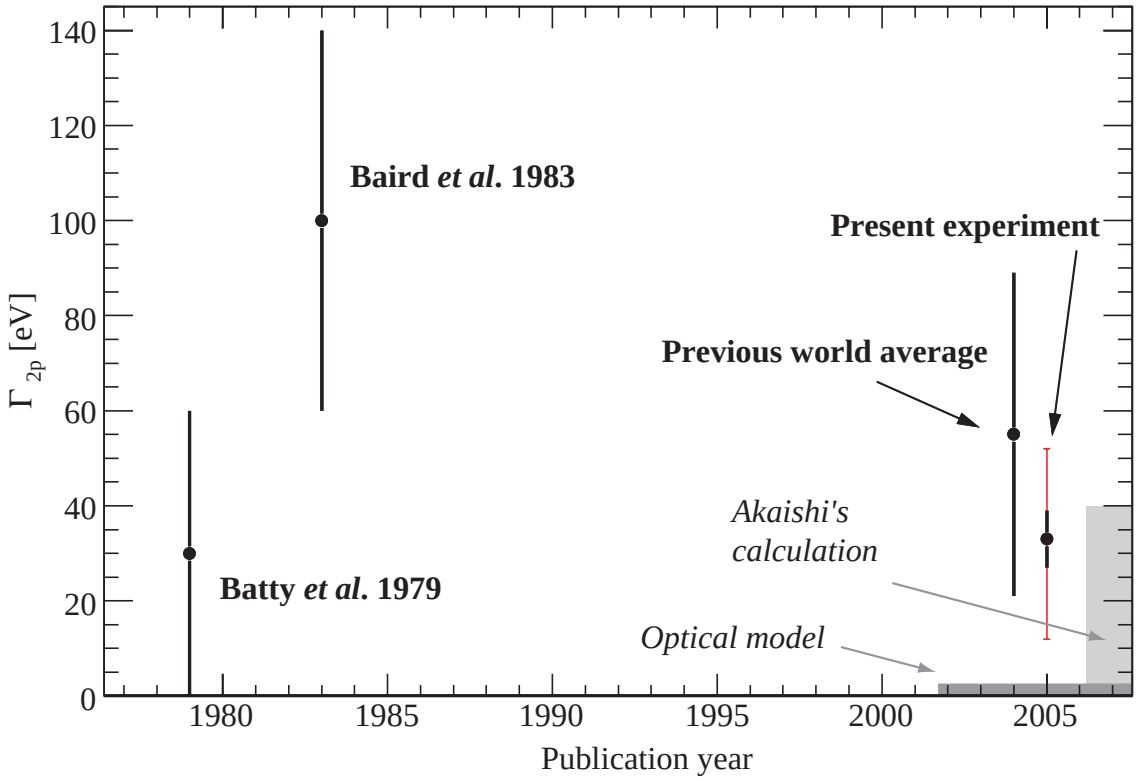

Figure 5.2: $2p$ state natural width obtained in the present experiment. The black error bar denotes only the statistical error, and the red error bar denotes **the most conservative error without Compton scattering correction** (its estimation is work in progress). In comparison, the previous measurements and their average are also plotted [4, 5]. The conventional optical-potential model and Akaishi's calculations are also shown [6, 17].

Chapter 6

Summary

We have measured kaonic helium-4 atom X-rays with the best statistical accuracy to date. As X-ray detectors, we used silicon drift detectors which have high energy resolution and small detector thickness. The experimental method of vertex reconstruction of the K^--^{4}He reaction point improved the signal-to-noise ratio drastically. To realize in-beam energy calibration, titanium and nickel characteristic X-rays induced by the charged particles contaminated in the beam were used. This method was critically needed for the precision spectroscopy.

We obtained for the strong-interaction shift and width of the kaonic helium-4 atom $2p$ state

$$\begin{aligned} \Delta E_{2p} &= -3.3 \pm 2.2(\text{stat.}) \text{ eV (repulsive)} \\ \Gamma_{2p} &= 33 \pm 6(\text{stat.}) \text{ eV} \end{aligned}$$

where only the statistical error was considered. Since the analysis has not been finished, the systematic error is not definite and its estimation is work in progress. Even if a conservative error is considered, our results are consistent with the theories discussed over the years. This resolves the long-standing kaonic helium puzzle.

Acknowledgments

I would like to express my sincere gratitude to my supervisor Prof. Ryugo S. Hayano, who guided me this interesting and exciting field of physics and gave me the opportunity to participate the experiment. His bright perspectives and his attitudes to enjoying physics have inspired me very much. I am grateful to him for continuous advice, encouragement and support I have been given for these two and a half years.

I would like to express my great thanks to Prof. Masahiko Iwasaki and Dr. Haruhiko Outa for their encouragement and advice. I have always been impressed by Prof. Iwasaki's sharp and deep knowledge and Dr. Outa's precise and speedy insight.

I am deeply grateful to Dr. Takashi Ishikawa, who taught me countless things from the basic of physic experiment to how to compose haiku (Japanese poems) and continuously encouraged me with friendly smile in my school days.

I am deeply grateful to Dr. Shinji Okada and Dr. Masami Iio, who taught me i-ro-ha (ABC) of experimental techniques when I went to KEK first time and gave me valuable friendship. We have worked together day and night (from evening till early morning), and I have learned many things.

I am grateful to Dr. Shigeru Ishimoto. He is one of the best specialists and advisers for cryogenic physics. He helped and encouraged me usually.

I would like to express my great thanks to Prof. Eberhard Widmann, Dr. Johann Zmeskal, Dr. Tomoichi Ishiwatari and other members of SMI[(i)], who rent us X-ray detectors and electric modules and taught us the operation and properties kindly.

I am grateful to Prof. George Beer, who taught me physics and English through the friendly discussions. His joyful talks and sincere curiosity about physics have encouraged me very much.

I am truly grateful to analysis core members, Dr. Kenta Itahashi, Dr. Takatoshi Suzuki and Mr. Masaharu Sato. Dr. Itahashi gave me full supports for basic analysis and analyzed the huge flash ADC data for me. Dr. Suzuki's grateful analysis for drift chambers is inimitable. And I have a lot of respect for his aggressive attitude toward physics, experiment and analysis. Mr. Sato usually encouraged and taught me many things in the last train home from RIKEN and gave me some drawings for this work.

I would like to express my best regards to the other collaborators of KEK-PS

[(i)] Stefan Meyer Institut für subatomare Physik, Austria

E570 experiment, Prof. Hyoungchan Bhang, Dr. Michael Cargnelli, Prof. Junsei Chiba, Prof. Seonho Choi, Dr. Catalina Curceanu, Mr. Yoshiyuki Fukuda, Mr. Toshio Hanaki, Dr. Masaaki Iwai, Dr. Bertalan Juhász, Prof. Paul Kienle, Dr. Johann Marton, Dr. Yasuyuki Matsuda, Dr. Hiroaki Ohnishi, Mr. Philipp Schmid, Dr. Shoji Suzuki, Dr. Dai Tomono, Prof. Toshimitsu Yamazaki, and Mr. Heejoong Yim. Their sincere and powerful collaborations led this experiment to successful and historic results.

I would like to express my great appreciation to Prof. Yoshinori Akaishi and again Prof. Toshimitsu Yamazaki for their invaluable contribution from the theoretical side. The experiment was motivated by their prediction of deeply bound kaonic nuclear states.

I also acknowledge Dr. Takashi Taniguchi for his advice and contribution in developing electronics. He gave a kind response to our requests after another.

I would like to express my special thanks to all the members of the nuclear experiment group and the fourth students, Mr. Hirokazu Odaka and Mr. Kohey Kamada at the University of Tokyo, and all the members of the Advanced Meson Science Laboratory at RIKEN for their contributions and encouragements.

Last but not least, I would like to express gratitude to my family and all my friends for their continuous supports and encouragements.

Appendix A

Background Contamination

In the z-coordinate vertex histogram, the following possible contaminations should be considered,

1. K^- in-flight decay,
2. K^- in-flight reactions

Stopped K^- events selection is one of the methods to reject the contaminations.

A.1 K^- In-flight Decay

A K^- passing the target may decay into charged particles ($K^- \rightarrow \mu^-\nu$, $\pi^-\pi^0$). Such muons and pions cause a background when they pass through drift chambers. In principle, the target-fiducial-volume cuts cannot reject those events in which the K^- decays in the target.

A.2 K^- In-flight Reaction

A K^- may react with a target nucleus before it stops. Since those K^- are not captured, kaonic helium X-rays are never emitted. So the vertex reconstruction of those events results in a background.

A.3 Stopped K^- Events Selection

In order to reject the above backgrounds, stopped K^- event selection is a useful method.

We have the z position of a vertex with good resolution ($\sim 0.3 - 0.5$ mm). This gives excellent resolution on the target material thickness to within 7 mg/cm^2. Assuming a K^- stops at the reaction point, the incident K^- energy just before the

target can be calculated from the range-energy relation. This means we can estimate the energy loss on the most downstream counter T0 using the z-vertex.

By comparing the real energy loss on the T0 with the estimated value from the z-vertex, some part of in-flight decay/reaction events can be rejected. Nevertheless, the author did not use this method, because the selection reduces both background and signals with some correlation of the z-vertex. On the other hand, the signal we want to observe has a strong correlation with the z-vertex (attenuation effects and Compton scattering). In addition, the T0 gain study must be done carefully.

Appendix B

Normalization

The X-ray yield per stopped K^- is one of the most important physical quantities to confirm the cascade model of kaonic atoms. However, it is not simple and not easy. Here, the outline of the normalization is described.

The number of stopped K^- is estimated by the observed number of $K_{\mu 2}$ peak (the muon peak of $K^- \to \mu^- + \bar{\nu}_\mu$). The relation is,

$$N_{K_{\mu 2}} = N_{stoppedK} f_{free} \epsilon_{time} B_{K_{\mu 2}} \epsilon_\mu \epsilon_{BLC_{K^-}} \epsilon_{PDC_\mu} \epsilon_{DAQ} \epsilon_{stoppedK} \tag{B.1}$$

where f_{free} is the free decay fraction of stopped K^- on ^{4}He, ϵ_{time} is the K^- survival rate within a time gate, $B_{K_{\mu 2}}$ is the branching ratio to the $K_{\mu 2}$ decay, ϵ_μ is the detection efficiency of muon from $K_{\mu 2}$ decay, $\epsilon_{BLC_{K^-}}$ is the tracking efficiency of BLC for K^-, ϵ_{PDC_μ} is the tracking efficiency of PDC for muons, ϵ_{DAQ} is the trigger accepted ratio and the efficiency of K^- identification and $\epsilon_{stoppedK}$ is the efficiency of the stopped K^- selection.

The number of X-ray peak is represented by,

$$N_X = N_{stoppedK} B_X \epsilon_{SDD} \epsilon_{BLC_{K^-}} (\epsilon_{PDC_{charged}} \,\mathrm{OR}\, \epsilon_{VDC_{charged}}) \epsilon_{DAQ} \epsilon_{stoppedK} \tag{B.2}$$

where B_X is the X-ray yield per stopped K^-, ϵ_{SDD} is the detection efficiency of SDDs and $(\epsilon_{PDC_{charged}} \,\mathrm{OR}\, \epsilon_{VDC_{charged}})$ is the tracking efficiency for secondary charged particles used to reconstruct a vertex.

Then we can obtain for the X-ray yield per stopped K^-,

$$B_X = f_{free} \epsilon_{time} \frac{N_X}{N_{K_{\mu 2}}} \frac{B_{K_{\mu 2}} \epsilon_\mu}{\epsilon_{SDD}} \frac{\epsilon_{PDC_\mu}}{(\epsilon_{PDC_{charged}} \,\mathrm{OR}\, \epsilon_{VDC_{charged}})} \tag{B.3}$$

f_{free} is known with very large uncertainty ($f_{free} = 3.5 \pm 0.5\%$ [29]) and ϵ_{time} is defined as

$$\epsilon_{time} = \exp\left(-\frac{T}{\tau^-}\right) \tag{B.4}$$

where $\tau^- \sim 10.24$ ns is the observed lifetime [29] of K^- trapped by meta-stable states and T is the time gate on the reaction timing.

Appendix C

Acceptance Estimation and Simulated Compton Scattering

In this thesis, the GEANT 4.8.2 simulation toolkit was used to estimate the acceptance of X-ray detection for SDDs and to evaluate the systematic error associated with Compton scattering effects in the target.

The geometrical acceptance was determined as 0.178%. Based on this , we calculated the acceptance for L_α X-rays to be 0.083%. This difference comes from the attenuation effect in the target. The simulated acceptance distribution for the target z coordinate is shown in Figure C.1. Some X-rays can not exit the back of the target due to attenuation.

Compton scattering of L_α X-ray seems to be like Figure C.2. The relation of the detected photon energy and the scattering angle is shown in Figure C.3. There is no free electron scattering curve, and the binding-energy threshold of an electron of helium atom is clearly seen. This indicates the simulation treats the atomic bound electrons correctly.

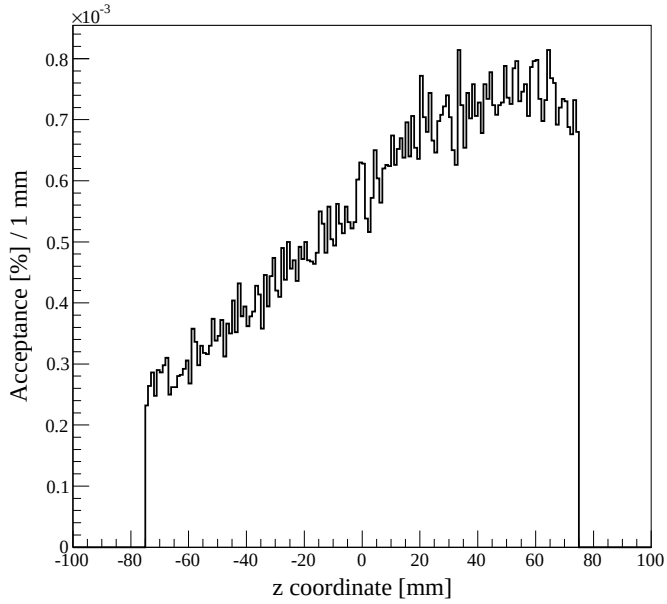

Figure C.1: Simulated acceptance distribution of L_α X-ray for the target z coordinate. The negative sign of z denotes the upstream of the target. The target-back acceptance is more than twice lower than the target-front one.

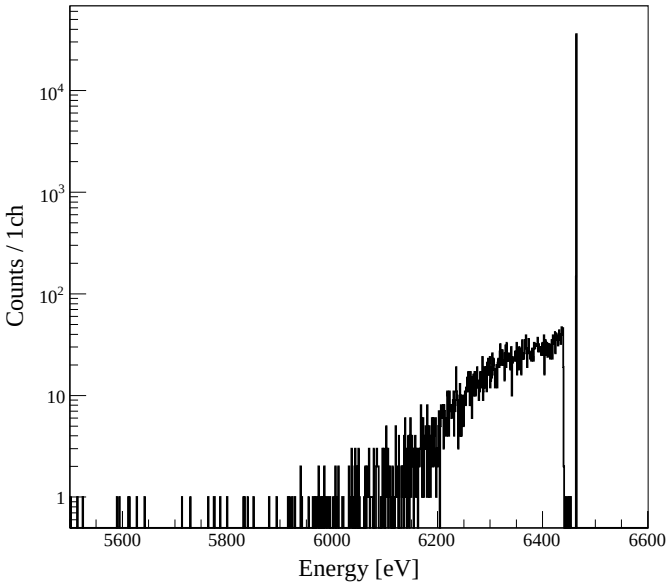

Figure C.2: GEANT4 simulation of L_α X-rays generated in the liquid helium-4 target. Scattered X-rays construct a tail structure ∼100 eV lower than the original peak. The tail structure influences the estimation of ΔE_{2p} and Γ_{2p}.

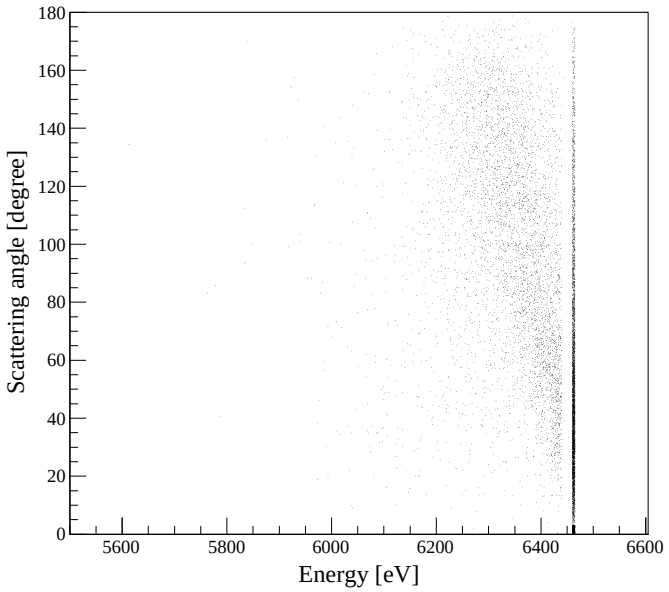

Figure C.3: Relationship between detected photon energy and Compton scattering angle. There is no free electron scattering curve.

Appendix D

Individual SDDs Analysis

In E570, we have the 10 SDDs in total. In this chapter, the individual SDDs analysis is described.

D.1 Local Fitting for Signal and Calibration Spectra

Since each SDD did not have enough amount of data to perform the global-fit, the individual spectra were fitted locally. In contrast to the summed-over analysis, which was described in the previous chapters, we assumed the kaonic-helium lines were represented by a response-function of single Gaussian. A Gaussian and a linear-background were used for fitting. Here, our objectives were the *mean* and the *sigma*.

To compare the sigma of the kaonic-helium X-ray with the individual-SDDs energy resolution represented by equation 3.3, the high-statistics self-trigger spectra were fitted globally. Moreover, to check the local-fit was consistent with the global-fit, the calibration spectra were also fitted locally by three Gaussians for $K_{\alpha 1}$, $K_{\alpha 2}$ and K_{β} lines. The summary of the fit method is shown in Table D.1.

Table D.1: Summary of the fit method for the individual SDDs analysis.

Data	Fit	Functions	Objectives
E549 trigger	local	single Gaussian + linear BG	mean and sigma
Self-trigger	local	three Gaussians + linear BG	mean and sigma
	global	six Gaussians + quadratic BG	SDD-resolution function

Figure D.1 shows an example of the fit method. The top figure a) is a calibrated kaon-trigger spectrum with a L_{α}-peak local fitting. The bottom one b) is a self-trigger spectrum. The kaonic-helium width was compared with the widths of calibration peaks.

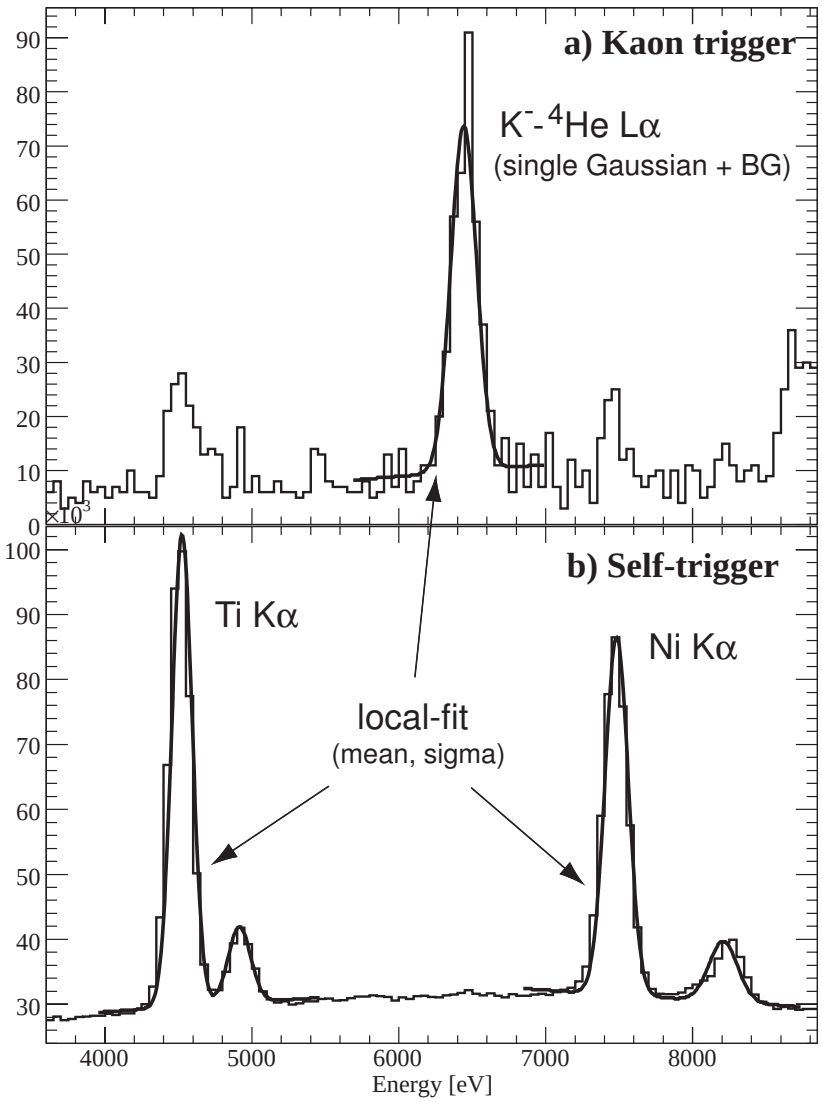

Figure D.1: Local-fit method to analyze the individual-SDDs data. The top a) is a kaon-trigger spectrum with a L_α-peak local fitting. The bottom b) is a self-trigger spectrum. The kaonic-helium width was compared with the widths of calibration peaks.

D.2 Fit Result of Width

The individual-SDDs spectra were fitted by the above method. The results are shown in the following figures. For comparison, the calculated-sigma from equation 3.3 is drawn in a solid line. Its parameters, noise and Fano factor, were obtained by a *global-fit*. The *local-fit* results are shown as black points with error bars.

There is a tendency that the kaonic-helium L_α line is *wider* than the detector resolution, which is consisted with the local-fits of the calibration spectrum. Even though some results of the second cycle shows no difference between the kaonic-helium 2p-level width and the detector resolution within large statistical errors, both the total of first and second cycle results indicate the existence of a *finite width* which can not be explained by the detector resolution (Figure D.22 and Figure D.23). This indication provides a positive opinion to the deeply-bound $\bar{K}$-nucleus state of the Akaishi-Yamazaki prediction [2]. In order to get a definite conclusion, we need more careful analysis with the estimation of the systematic error.

D.3 Fit Result of Mean

The obtained mean of the Gaussian are summarized in the Table D.2. Due to the large statistical errors, it is difficult to say a clear thing about the strong-interaction shift.

Table D.2: Obtained Gaussian mean of kaonic-helium L_α X-ray and the strong-interaction shift, assuming the pure-electromagnetic energy is 6463 eV [16].

Detector	Gaussian center (eV)	ΔE_{2p} (eV)
SDD2-1st	6455±6	-8±6
SDD4-1st	6443±7	-20±7
SDD5-1st	6467±8	4±8
SDD1-2nd	6467±6	4±6
SDD2-2nd	6471±9	8±9
SDD3-2nd	6450±10	-13±10
SDD4-2nd	6449±10	-4±10
SDD5-2nd	6454±11	-9±11
SDD7-2nd	6471±9	8±9
SDD8-2nd	6465±9	2±9

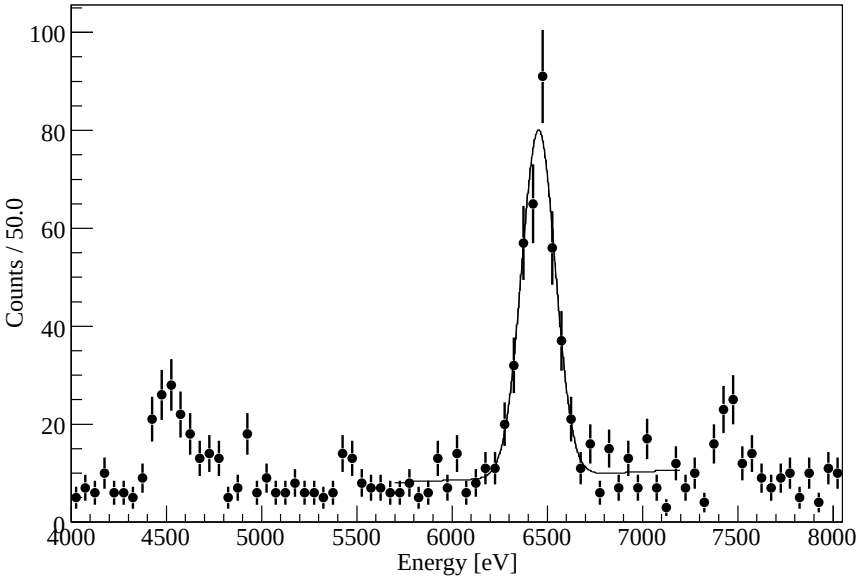

Figure D.2: Local-fit of the kaonic-helium L_α peak (SDD2-1st).

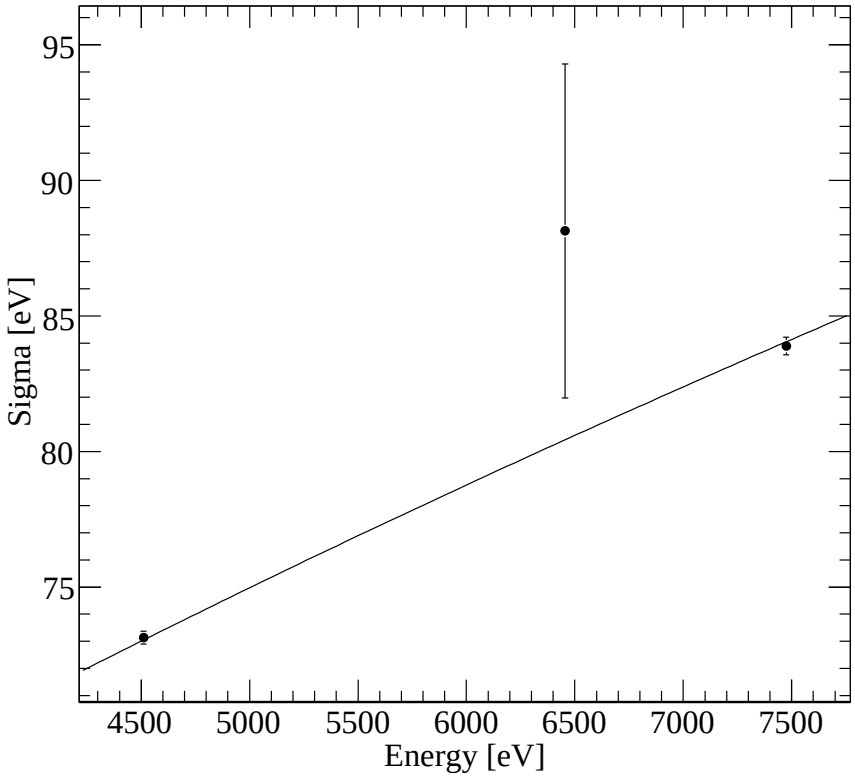

Figure D.3: Obtained sigma by the local-fits of the L_α X-ray and calibration lines (SDD2-1st). Solid line represents the SDD-resolution function.

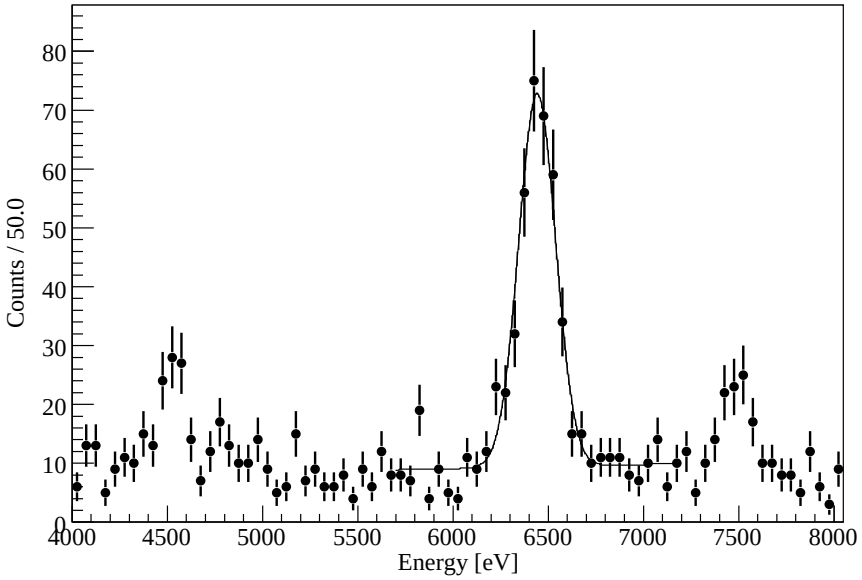

Figure D.4: Local-fit of the kaonic-helium L_α peak (SDD4-1st).

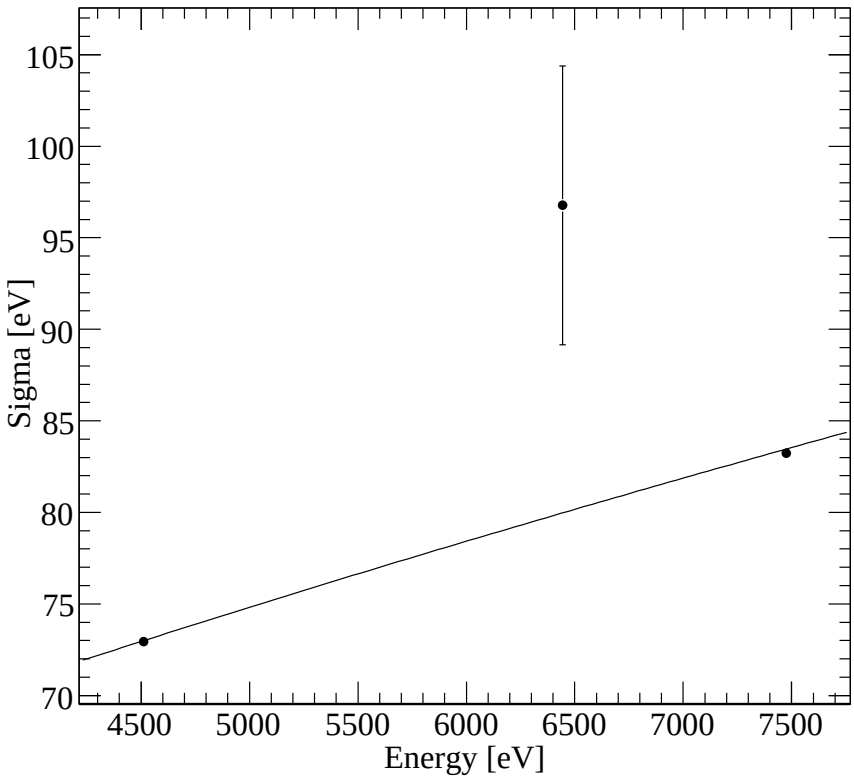

Figure D.5: Obtained sigma by the local-fits of the L_α X-ray and calibration lines (SDD4-1st). Solid line represents the SDD-resolution function.

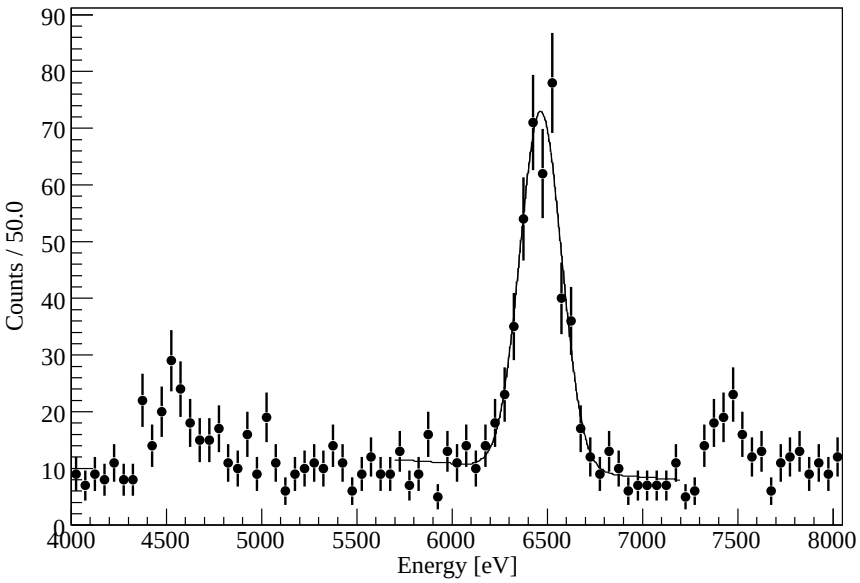

Figure D.6: Local-fit of the kaonic-helium L_α peak (SDD2-1st).

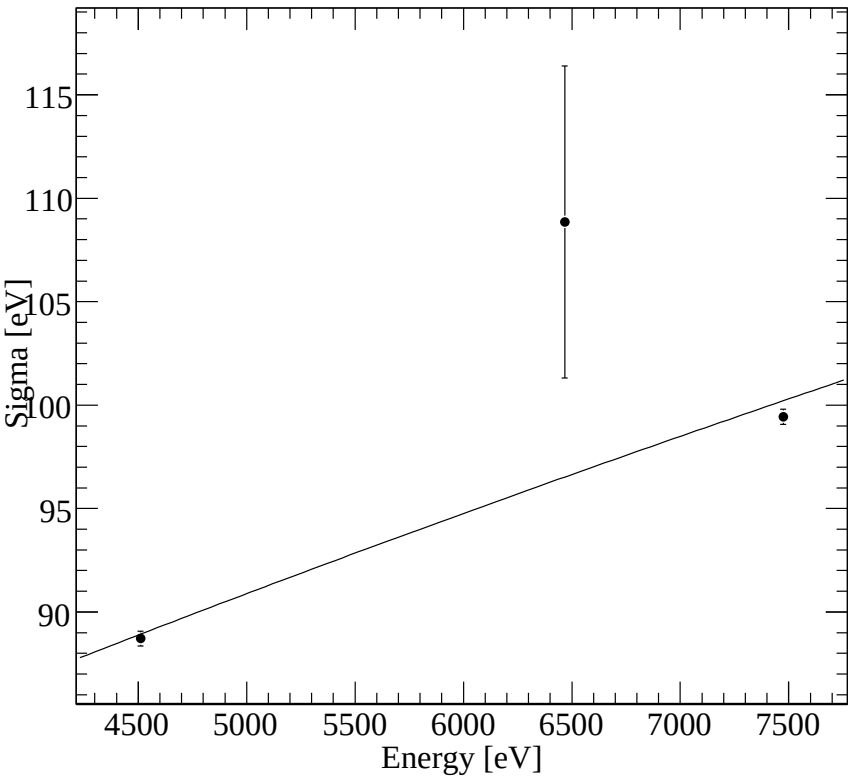

Figure D.7: Obtained sigma by the local-fits of the L_α X-ray and calibration lines (SDD5-1st). Solid line represents the SDD-resolution function.

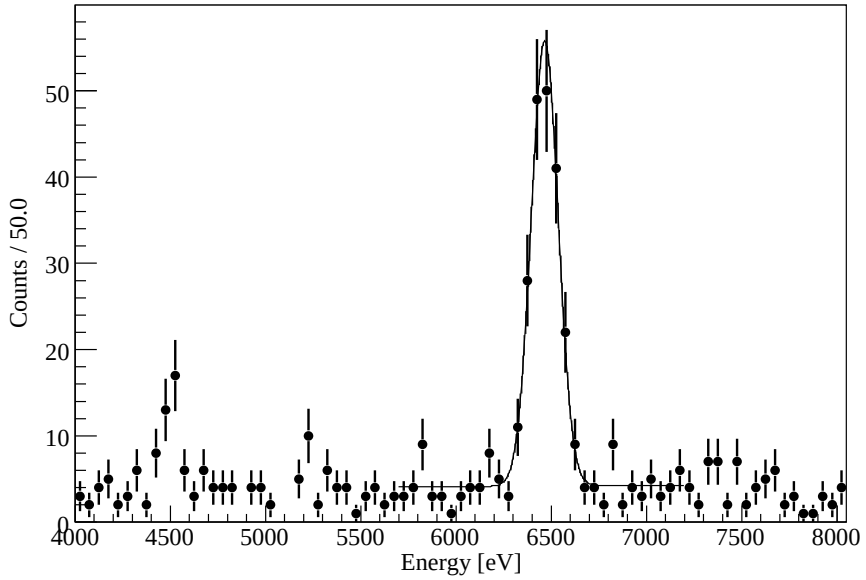

Figure D.8: Local-fit of the kaonic-helium L_α peak (SDD1-2nd).

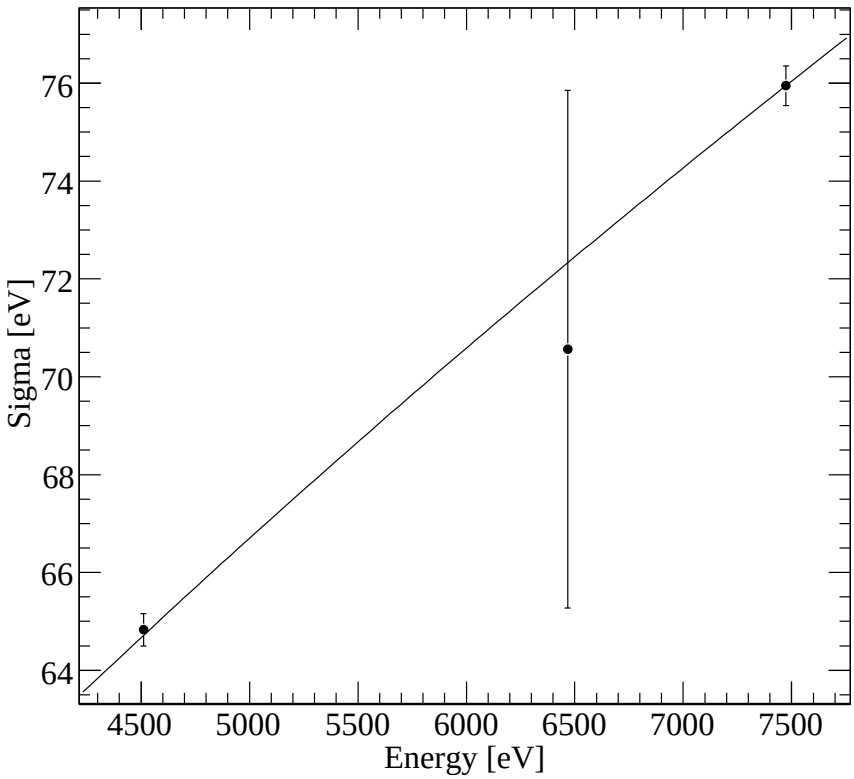

Figure D.9: Obtained sigma by the local-fits of the L_α X-ray and calibration lines (SDD1-2nd). Solid line represents the SDD-resolution function.

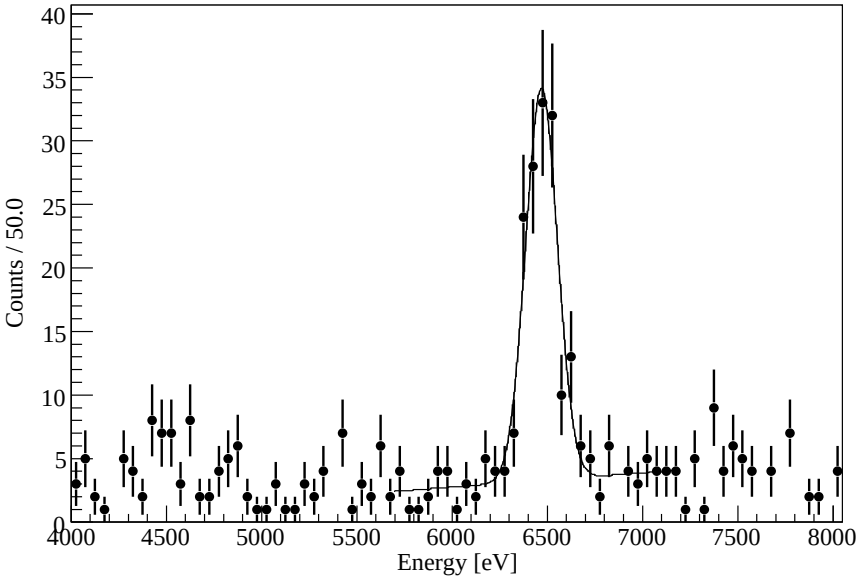

Figure D.10: Local-fit of the kaonic-helium L_α peak (SDD2-2nd).

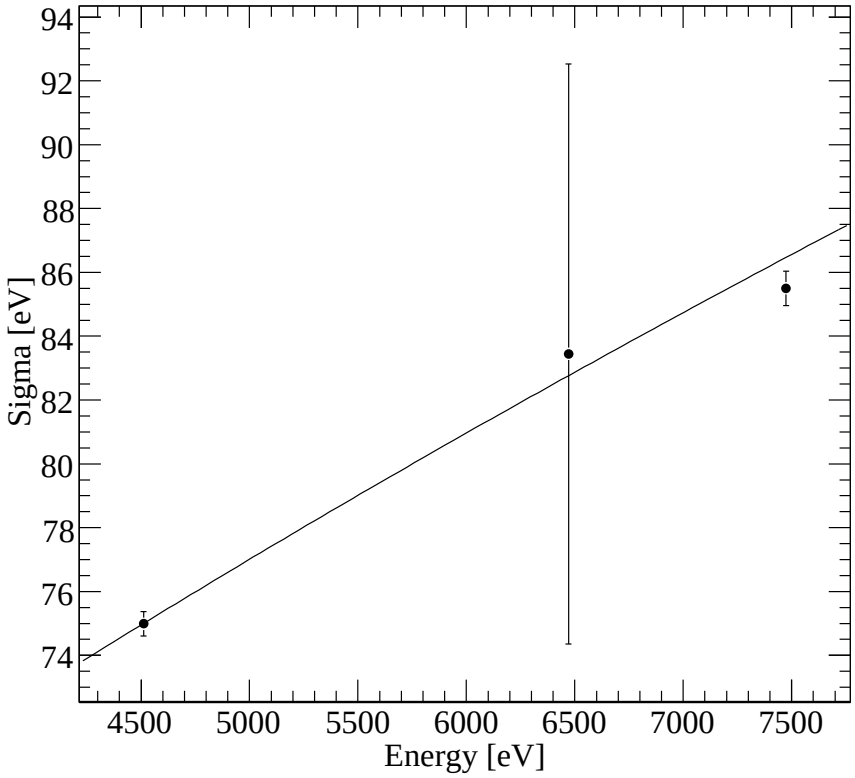

Figure D.11: Obtained sigma by the local-fits of the L_α X-ray and calibration lines (SDD2-2nd). Solid line represents the SDD-resolution function.

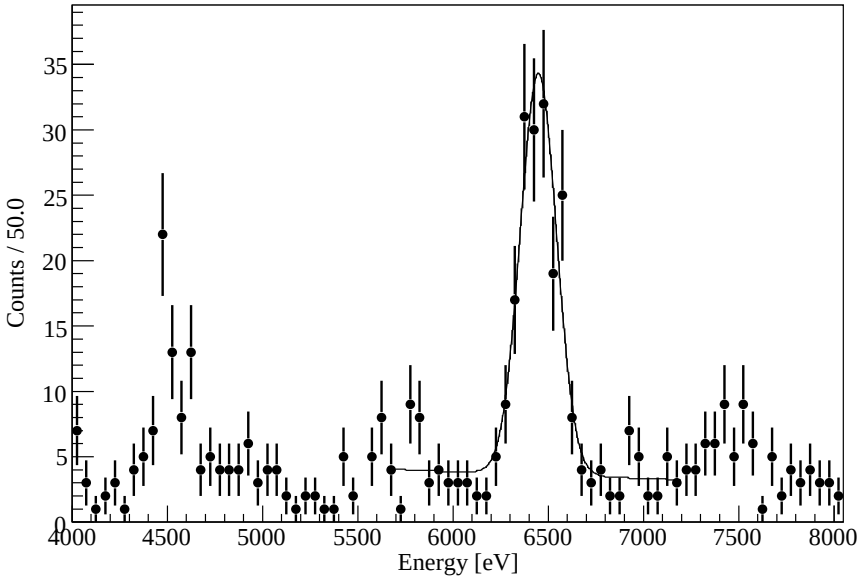

Figure D.12: Local-fit of the kaonic-helium L_α peak (SDD3-2nd).

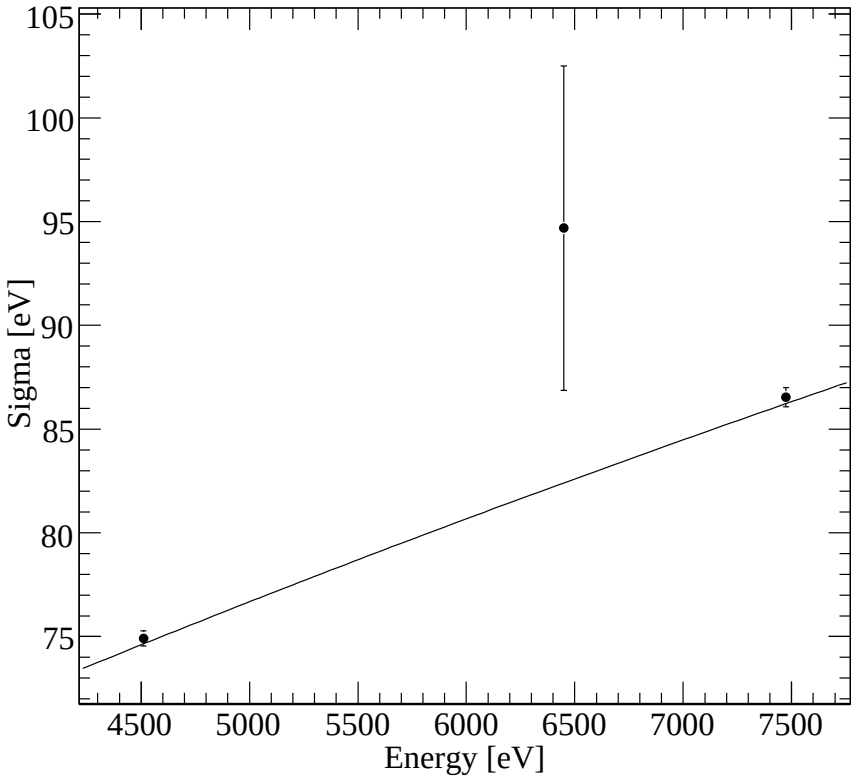

Figure D.13: Obtained sigma by the local-fits of the L_α X-ray and calibration lines (SDD3-2nd). Solid line represents the SDD-resolution function.

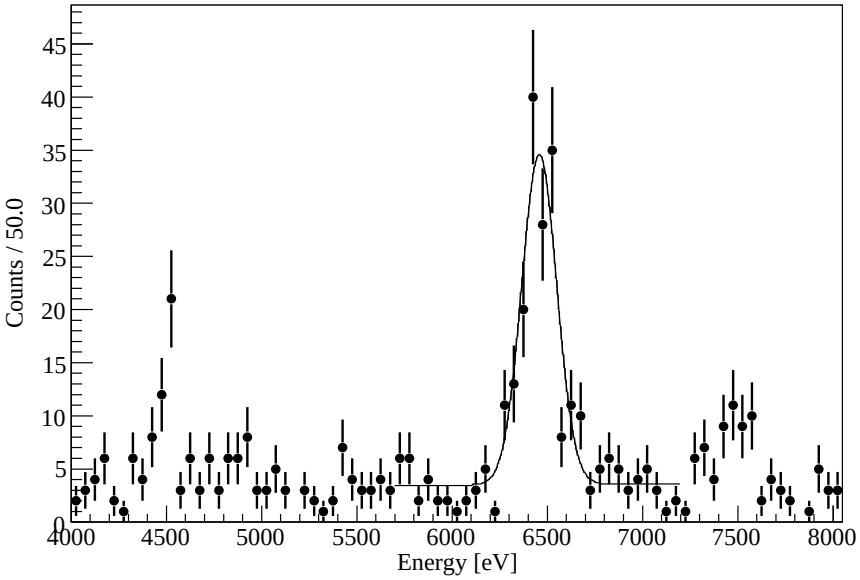

Figure D.14: Local-fit of the kaonic-helium L_α peak (SDD4-2nd).

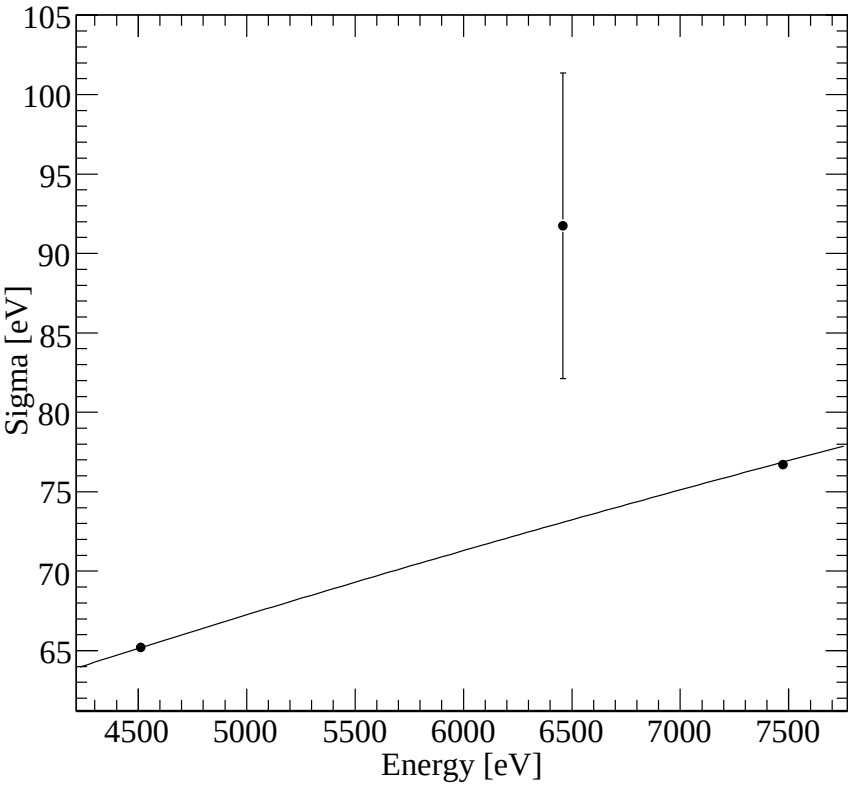

Figure D.15: Obtained sigma by the local-fits of the L_α X-ray and calibration lines (SDD4-2nd). Solid line represents the SDD-resolution function.

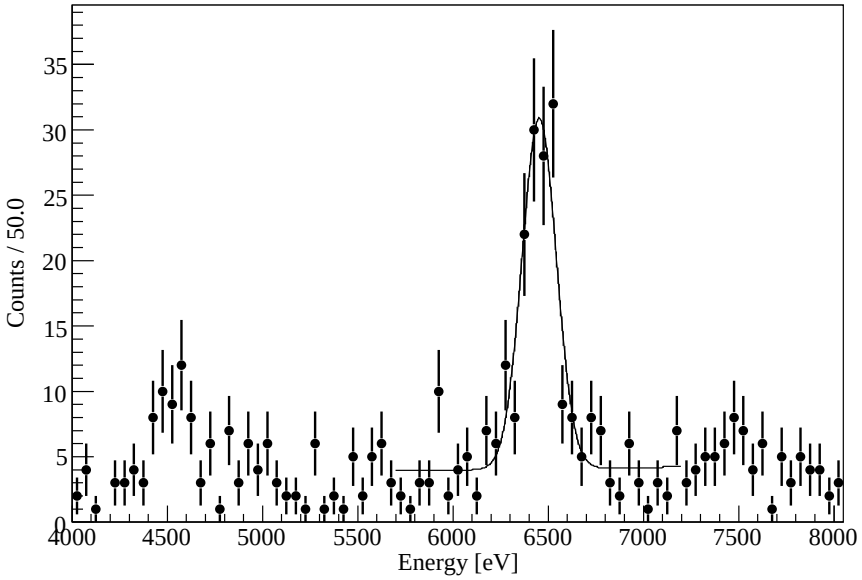

Figure D.16: Local-fit of the kaonic-helium L_α peak (SDD5-2nd).

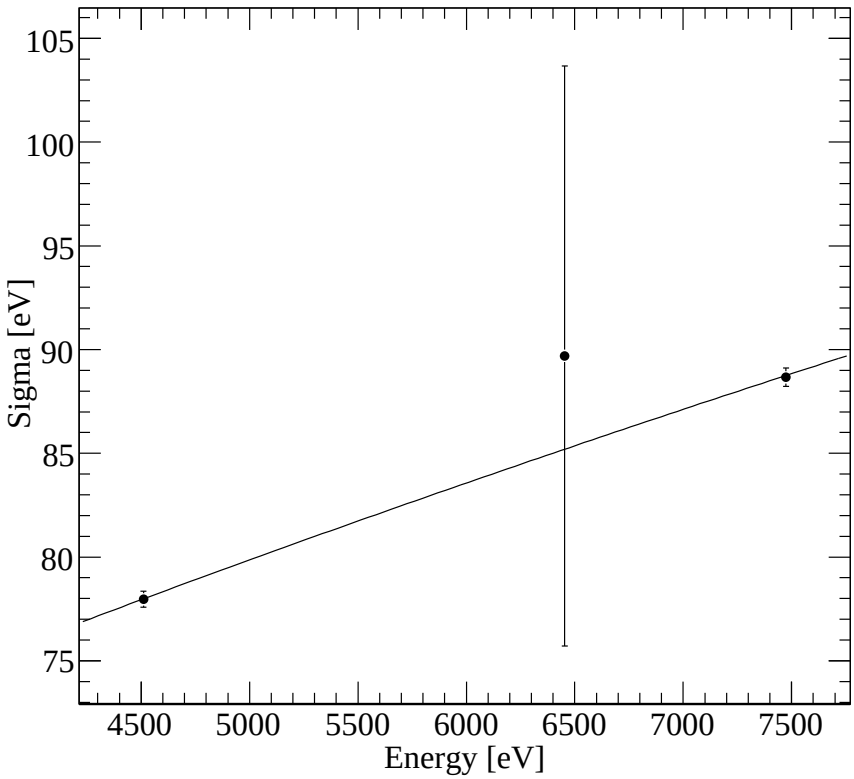

Figure D.17: Obtained sigma by the local-fits of the L_α X-ray and calibration lines (SDD5-2nd). Solid line represents the SDD-resolution function.

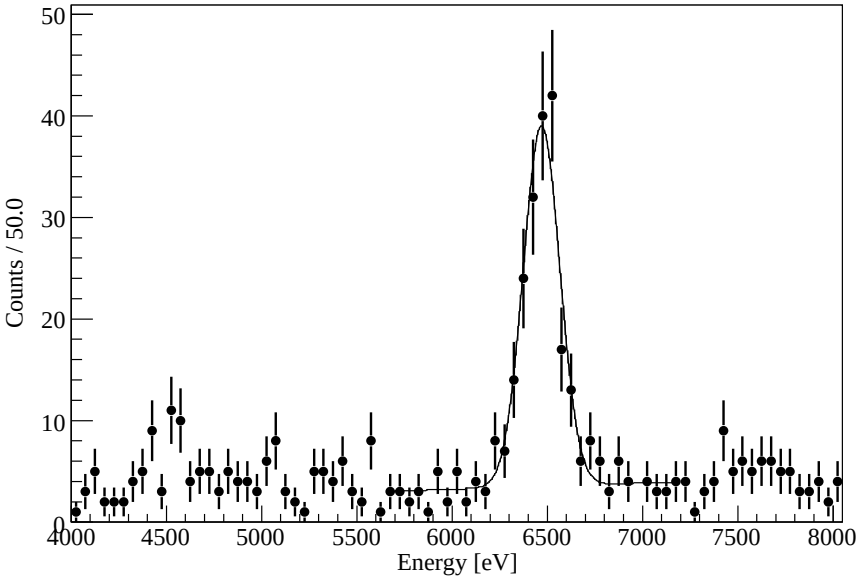

Figure D.18: Local-fit of the kaonic-helium L_α peak (SDD7-2nd).

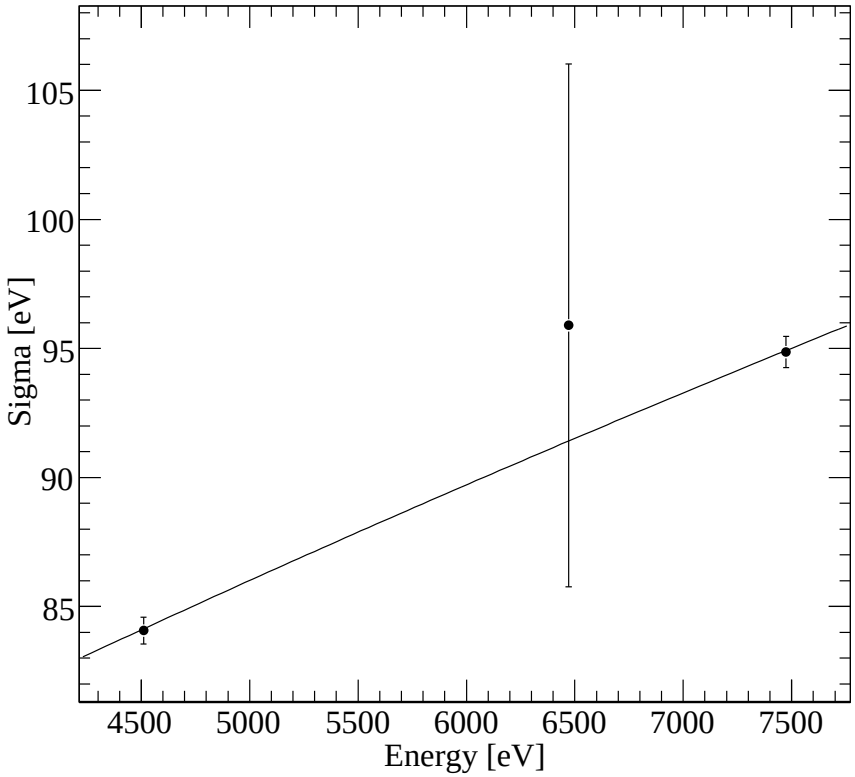

Figure D.19: Obtained sigma by the local-fits of the L_α X-ray and calibration lines (SDD7-2nd). Solid line represents the SDD-resolution function.

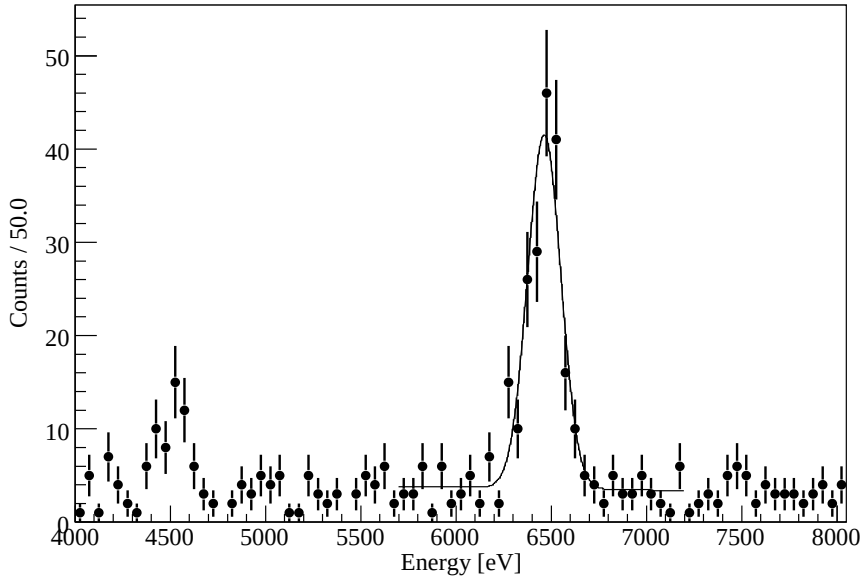

Figure D.20: Local-fit of the kaonic-helium L_α peak (SDD8-2nd).

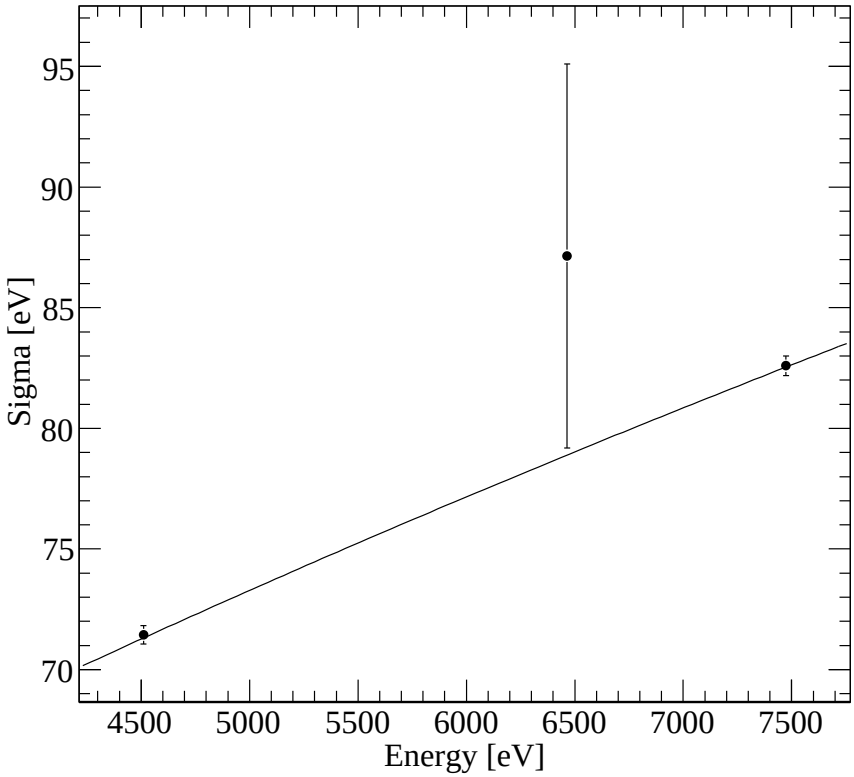

Figure D.21: Obtained sigma by the local-fits of the L_α X-ray and calibration lines (SDD8-2nd). Solid line represents the SDD-resolution function.

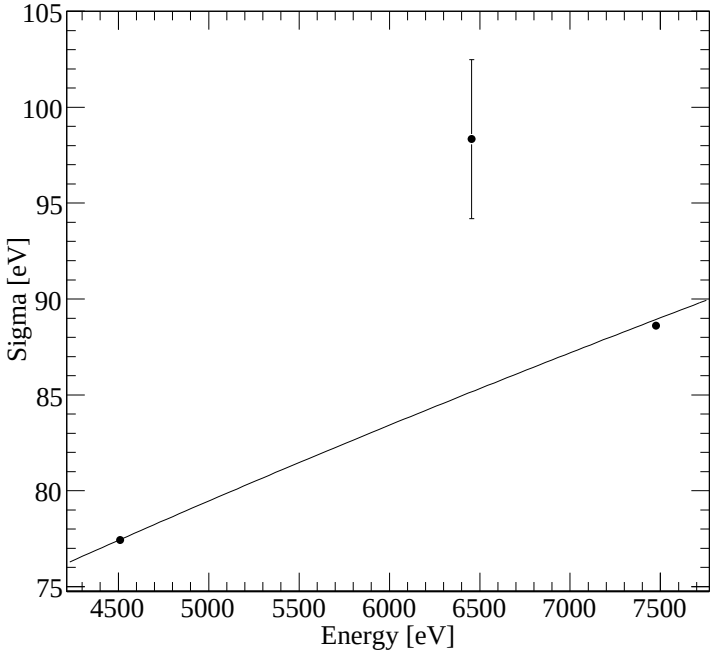

Figure D.22: Obtained sigma by the local-fits of the L_α X-ray and calibration lines (total-1st). Solid line represents the SDD-resolution function.

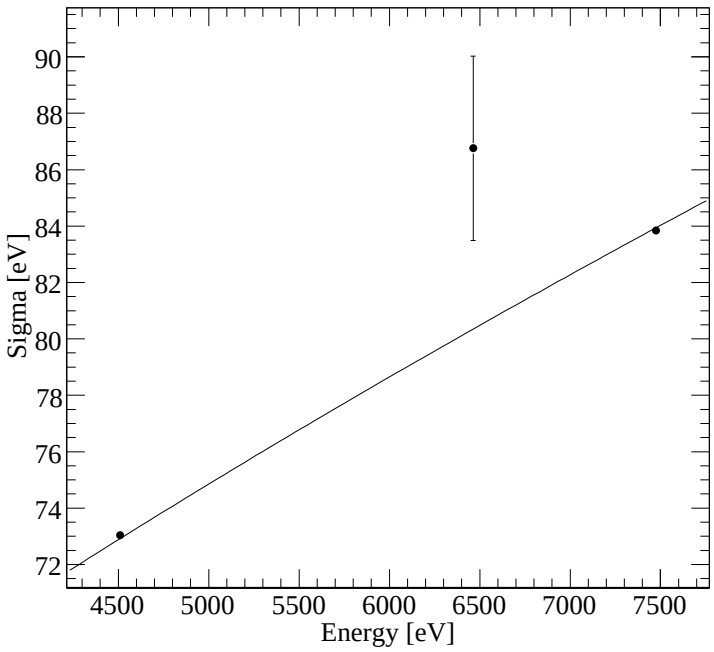

Figure D.23: Obtained sigma by the local-fits of the L_α X-ray and calibration lines (total-2nd). Solid line represents the SDD-resolution function.

Bibliography

[1] C.J. Batty, E. Friedman, A. Gal, Phys Rep **287** (1997) 385.

[2] Yoshinori Akaishi and Toshimitsu Yamazaki, Phys. Rev. C **65** (2002) 044005.

[3] Clyde E. Wiegand and Richard H. Pehl, Phys. Rev. Lett. **27** (1971) 1410.

[4] C.J. Batty, S.F. Biagi, S.D. Hoath, P. Sharman, J.D. Davies, G.J. Pyle, G.T.A. Squier, Nucl. Phys. **A326** (1979) 455.

[5] S. Baird, C.J. Batty, F.M. Russell, P. Sharman, P.M. Bird, A.S. Clough, K.R. Parker, G.J. Pyle, G.T.A. Squier, Nucl. Phys. **A392** (1983) 297.

[6] C.J. Batty, Nucl. Phys. **A508** (1990) 89c.

[7] Ryoichi Seki, Phys. Rev. **C5** (1972) 1196.

[8] Justus H. Koch, Morton M. Sternheim, James F. Walker, Phys. Rev. **C5** (1972) 381.

[9] E. Friedman, A. Gal, Phys Lett, B **459** (1999) 43.

[10] T. M. Ito, R. S. Hayano, S. N. Nakamura, T. P. Terada, M. Iwasaki, D. R. Gill, L. Lee, A. Olin, M. Salomon, S. Yen, K. Bartlett, G. A. Beer, G. Mason, G. Trayling, H. Outa, T. Taniguchi, Y. Yamashita, R. Seki, Phys. Rev. C **58** (1998) 2366.

[11] T. Suzuki, H. Bhang, G. Franklin, K. Gomikawa, R.S. Hayano, T. Hayashi, K. Ishikawa, S. Ishimoto, K. Itahashi, M. Iwasaki, T. Katayama, Y. Kondo, Y. Matsuda, T. Nakamura, S. Okada, H. Outa, B. Quinn, M. Sato, M. Shindo, H. So, P. Strasser, T. Sugimoto, K. Suzuki, S. Suzuki, D. Tomono, A.M. Vinodkumar, E. Widmann, T. Yamazaki, T. Yoneyama, Phys. Lett. B **597** (2004) 263.

[12] M. Iwasaki, T. Suzuki, H. Bhang, G. Franklin, K. Gomikawa, R.S. Hayano, T. Hayashi, K. Ishikawa, S. Ishimoto, K. Itahashi, T. Katayama, Y. Kondo, Y. Matsuda, T. Nakamura, S. Okada, H. Outa, B. Quinn, M. Sato, M. Shindo, H. So, P. Strasser, T. Sugimoto, K. Suzuki, S. Suzuki, D. Tomono, A.M. Vinodkumar, E. Widmann, T. Yamazaki, T. Yoneyama, arXive:nucl-ex/0310018 v2 16 Nov 2004.

[13] M. Agnello, G. Beer, L. Benussi, M. Bertani, S. Bianco, E. Botta, T. Bressani, L. Busso, D. Calvo, P. Camerini, P. Cerello, B. Dalena, F. De Mori, G. D'Erasmo, D. Di Santo, F. L. Fabbri, D. Faso, A. Feliciello, A. Filippi, V. Filippini, E. M. Fiore, H. Fujioka, P. Gianotti, N. Grion, V. Lucherini, S. Marcello, T. Maruta, N. Mirfakhrai, O. Morra, T. Nagae, A. Olin, H. Outa, E. Pace, M. Palomba, A. Pantaleo, A. Panzarasa, V. Paticchio, S. Piano, F. Pompili, R. Rui, G. Simonetti, H. So, S. Tomassini, A. Toyoda, R. Wheadon, A. Zenoni, Phys. Rev. Lett. **94** (2005) 212303.

[14] T. Kishimoto, T. Hayakawa, S. Ajimura, S. Minami, A. Sakaguchi, Y. Shimizu, R.E. Chrien, M. May, P. Pile, A. Rusek, R. Sutter, H. Noumi, H. Tamura, M. Ukai, Y. Miura, K. Tanida, Nucl. Phys. A **754** (2005) 383.

[15] Clyde E. Wiegand and Gary L. Godfrey, Phys. Rev. A **9** (1974) 2282.

[16] J. P. Santos, F. Parente, S. Boucard, P. Indelicato, J. P. Desclaux, Phys. Rev. A **71** (2005) 032501.

[17] Y. Akaishi, Proceedings of EXA05 International Conference on Exotic Atoms and Related Topics, February 21-25, 2005, Vienna, Austria.

[18] K.H. Tanaka, M. Ieiri, H. Noumi, M. Minakawa, Y. Yamanoi, Y. Kato, H. Ishii, Y. Suzuki, M. Takasaki, Nucl. Instr. and Meth. **A363** (1995) 114.

[19] Emilio Gatti and Pavel Rehak, Nucl. Instr. and Meth. **A225** (1984) 608.

[20] T. Eggert, P. Goldstrass, J. Kemmer, A. Pahlke, Nucl. Instr. and Meth. **A512** (2003) 257.

[21] Albert C. Thompson *et al.*, X-RAY DATA BOOKLET Center for X-ray Optics and Advanced Light Source, Lawrence Berkeley National Laboratory (2001).

[22] F. Perotti and C. Fiorini, Nucl. Instr. and Meth. **A423** (1999) 356.

[23] F. James and M. Rose, MINUIT manual, CERN report (1989).

[24] T. Koike, Y. Akaishi, Nucl. Phys. **A639** (1998) 521c.

[25] C.A. Baker, C.J. Batty, J. Moir, S. Sakamoto, J.D. Davies, J. Lowe, J.M. Nelson, G.J. Pyle, G.T.A. Squier,R.E. Welsh, R.G. Winter, E.W.A. Lingeman, Nucl. Phys. **A494** (1989) 507.

[26] R. Marc Kippen, New Astronomy Reviews **48** (2004) 221.

[27] L.Vainshtein, R.Sunyaev, E.Churazov, Astron. Lett. **24** (1998) 271

[28] T. Yamazaki, M. Aoki, M. Iwasaki, R.S. Hayano, T. Ishikawa, H. Outa, E. Takeda, H. Tamura, Phys. Rev. Lett. **63** (1989) 1590.

[29] H. Outa, Doctoral Dissertation, Univ. of Tokyo (2003).